Title
Topological Insulators and Ferrimagnets for Efficient and Fast Magnetization Manipulation

Author
Pan, Quanjun

Publication Date
2022

Peer reviewed|Thesis/dissertation

UNIVERSITY OF CALIFORNIA

Los Angeles

Topological Insulators and Ferrimagnets for Efficient and Fast Magnetization Manipulation

A dissertation submitted in partial satisfaction of the

requirements for the degree Doctor of Philosophy in

Electrical and Computer Engineering

by

Quanjun Pan

2022

ABSTRACT OF THE DISSERTATION

Topological Insulators and Ferrimagnets for Efficient and Fast Magnetization Manipulation

by

Quanjun Pan

Doctor of Philosophy in Electrical and Computer Engineering

University of California, Los Angeles, 2022

Professor Kang Lung Wang, Chair

Since the dawn of Big Data, the exponentially increasing demands for larger data volumes and higher information processing speeds have given the field of spintronics an astonishing momentum. In spintronics, the electron spins and their associated magnetic moments interplay with electronic charges, lattices, and even photons. These diverse interactions open endless possibilities for a new generation of fast, efficient, and non-volatile memory and logic devices to serve and fuel Big Data. Lying at the heart of innovating spintronic memory and logic devices is the search for advanced materials and mechanisms to control spin and magnetism.

Following this line of research, this dissertation focuses on exploring two emerging material classes, namely, topological insulators and ferrimagnets, which hold great promise for efficient and fast magnetization manipulation. More specifically, topological insulators exhibit an extraordinary charge-spin conversion efficiency owing to their exotic surface states and can be employed to manipulate magnetic moments with minimal energy. Ferrimagnets, by contrast, are

of technical interest for fast magnetization manipulation because their two non-equivalent and antiparallel aligned sublattices uniquely combine the antiferromagnet-like ultrafast dynamics with the ferromagnet-like readability/controllability for well-established techniques. However, these novel materials have been difficult to investigate using conventional magnetometers or magnetic resonance techniques. To address these challenges, an experimental platform integrating a magneto-optical Kerr effect magnetometer, a femtosecond optical pump-probe technique, and common magneto-transport measurements, was first established.

Using this experimental platform, the charge-spin conversion efficiency was investigated and accurately quantified for a topological insulator-based magnetic bilayer, and a critical role of the topological surface states with spin-momentum locking was unveiled. With innovative material engineering, topological insulators were integrated with widely used metallic ferromagnet in a topological insulator/Mo/CoFeB/MgO structure. This topological insulator/Mo/CoFeB/MgO structure demonstrates high thermal stability, robust magnetic properties, and efficient magnetization switching driven by spin-orbit torques. The systematically calibrated efficiency confirms that, for a room temperature magnetic memory, topological insulators are at least one order of magnitude more efficient than conventional heavy metals. Moreover, the annealing effects were carefully studied in this structure, and desirable thermal compatibility with modern CMOS technology has also been achieved, empowering the development of advanced spintronic applications.

To realize faster control of magnetic moments, the dynamical characteristics of a compensated ferrimagnetic GdFeCo film with a vertical compositional gradient were investigated through the laser-induced ultrafast spin dynamics. It is found that the vertical composition gradient significantly alters the ultrafast spin dynamics. Surprisingly, these distinct spin dynamics can be

handily controlled by tuning the power of laser excitation, indicating the existence of more efficient energy pathways to control magnetization with high speed. These observations motivate ferrimagnets with a composition gradient as an ideal candidate for efficient and fast magnetization manipulation.

Emboldened by the findings in this dissertation, topological insulators and ferrimagnets undoubtedly possess a vast potential to increase the efficiency and speed of magnetization manipulation for advancing spintronic memory and logic devices.

The dissertation of Quanjun Pan is approved.

Chee Wei Wong

Mona Jarrahi

Yaroslav Tserkovnyak

Kang Lung Wang, Committee Chair

University of California, Los Angeles

2022

This dissertation is dedicated to my parents

for their unconditional love and support

TABLE OF CONTENTS

LIST OF FIGURES

ACRONYMS

AFM	Antiferromagnet
AHE	Anomalous Hall Effect
AMC	Angular Momentum Compensation
ARPES	Angle-Resolved Photoemission Spectroscopy
CMOS	Complementary Metal-Oxide-Semiconductor
DL-SOF (DL-SOT)	Damping-Like Spin-Orbit Field (Damping-Like Spin-Orbit Torque)
DMI	Dzyaloshinskii-Moriya interaction
DW	Domain Wall
FFT	Fast Fourier Transform
FIM	Ferrimagnet
FL-SOF (FL-SOT)	Field-Like Spin-Orbit Field (Field-Like Spin-Orbit Torque)
FM	Ferromagnet
FMR	Ferromagnetic Resonance
GMR	Giant Magneto-Resistance
HM	Heavy Metal
HR-TEM	High-Resolution Transmission Electron Microscopy
IP	In-Plane
LLG	Landau–Lifshitz–Gilbert
MBE	Molecular Beam Epitaxy
MC	Magnetization Compensation
MOKE	Magneto-Optical Kerr Effect
MRAM	Magnetic-resistive Random Access Memory

MTJ	Magnetic Tunnel Junction
OP	Out-of-Plane
PEM	Photoelastic Modulator
PMA	Perpendicular Magnetic Anisotropy
PPMS	Physical Property Measurement System
RHEED	Reflection High-Energy Electron Diffraction
SOC	Spin-Orbit Coupling
SOF	Spin-Orbit Field
SOT	Spin-Orbit Torque
SQUID	Superconducting Quantum Interference Device
SNR	Signal-to-Noise Ratio
TEM	Transmission Electron Microscopy
TI	Topological Insulator
TMR	Tunneling Magneto-Resistance
TR-MOKE	Time-Resolved Magneto-Optical Kerr Effect
TSS	Topological Surface State
XRD	X-Ray Diffraction

ACKNOWLEDGMENTS

The end of each journey marks the sailing of the next one. And my Ph.D. journey at DRL has prepared me for every future journey to come. This journey has been incredible and full of challenges that I cannot complete without the numerous help and support received from people I cannot be more grateful for. First and foremost, I would love to sincerely thank my advisor, Prof. Kang L. Wang, for his continuous guidance, support, and encouragement throughout the past six and a half years. What I learned from Prof. Wang has gone far beyond technical skills and intellectual knowledge to more of a life education about conducting oneself and treating others, facing the seemingly impossible and working through them, staying positive and always aiming high, and overall, how to become a better person. It is to my conviction that I am ready for the next and every journey ahead, and I express my deep gratitude to Prof. Wang.

I am also deeply grateful to Prof. Chee-Wei Wong, Prof. Mona Jarrahi, and Prof. Yaroslav Tserkovnyak for serving as my doctoral committee members and providing their expertise and insightful advice, from which I have greatly benefited. Prof. Chee-Wei Wong and his group have taught me much about optics, especially in ultrafast optics; Prof. Jarrahi and her group have shared their extensive knowledge and enriched experience in optical pump-probe techniques. Our collaboration on picosecond switching of ferrimagnets using photoconductive switches is a delightful and rewarding experience; Finally, I would like to thank Prof. Tserkovnyak for his enlightening teaching on solid-state physics and topology as well as the in-depth discussions and theoretical support on various phenomena stemming from spin-orbit coupling during my Ph.D. study. I also owe a great deal to many other outstanding collaborators for their generous help and informative inputs along the way. Specifically, I would like to thank Prof. Robert N. Schwartz and Prof. Benjamin J. Schwartz from the Department of Chemistry & Biochemistry, UCLA, Dr. Deniz

Turan and Dr. Nezih Tolga Yardimci from the Department of Electrical and Computer Engineering, UCLA, and Prof. Dmitry A. Fishman from the Department of Chemistry, UCI for sharing their valuable hands-on experience in building femtosecond optical measurement platforms; Prof. Jing Xia from UCI for demonstrating low-temperature optical measurements on topological insulator-based magnetic heterostructures; Prof. Zongzhi Zhang and Dr. Guanjie Wu from Fudan University for providing constructive suggestions and know-hows on establishing the optical pump-probe technique; Dr. Yuting Liu from Hong Kong University of Science and Technology for providing the TEM images and enormous contributions to our joint publication;

It has always been a privilege for me to work with many talented minds at DRL. Meeting and discussing with these brilliant DRLers every day have always been enlightening and the most rewarding part of the doctoral study. Needless to say, it would be impossible for me to tackle the challenges of a Ph.D. without the help of all DRL members. First, I would like to offer my special thanks to Dr. Mohammad Montazeri, Dr. Qiming Shao, and Dr. Yabin Fan. Dr. Mohammad Montazeri mentored me when I first came to DRL. He has taught me every essential knowledge and skill needed to set sail on my Ph.D. journey successfully. Before I joined, Dr. Mohammad had contributed significantly to DRL's research in magneto-optics and the development of optical detection techniques/lab where most of my doctoral research was conducted. His achievements laid the foundation for my work presented in this dissertation. Dr. Yabin initiated the study on optical quantification of spin-orbit torques in topological insulators. During our collaboration, I learned much about being a reliable and rigorous researcher and gained valuable research skills. Dr. Qiming Shao introduced me to the field of spintronics. Through our work together, he inspired me with his enthusiasm, insights, and dedication to high-quality work. Special thanks should also go to Dr. Xiaoyu Che, Dr. Christopher Eckberg, Dr. Hao Wu, Dr. Peng Zhang, Dr. Guoqiang Yu,

and Dr. Yingying Wu for their contributions and fruitful discussions in many aspects throughout my Ph.D. study; Hanshen Huang, Dr. Tao Qu, Bingqian Dai, and Dr. Peng Deng for their many hours of assistance with the experiments; Lixuan Tai, Dr. Yang Cheng, Dr. Di Wu, Dr. Kin Wong, and Dr. Sukong Chong for providing high-quality materials and devices; Dr. Armin Razavi, Prof. Gen Yin, Malcolm Jackson, Dr. Yuxiang Liu, Haoran He, Dr. Qingyuan Shu, Qiu Gang, Dr. Sidong Lei, Dr. Xiang Li, and Dr. Murong Lang for their supports in theory, simulation, and data analysis; and at last, all other DRL members for their notable collaborations and supports. Additionally, I am also thankful to Katie Christensen, Eileen Panguito, Wendy Sanchez, Ryo Arreola, and Deeona Columbia for their great administrative support.

Lastly, my sincerest gratitude and deepest love will go to my dear family for their unconditional love, inspiration, and support. Their trust in me has kept me encouraged and my motivation high throughout this Ph.D. study.

VITA

Education

2018 – 2022 ***Ph.D. Candidate*** in Electrical and Computer Engineering
University of California, Los Angeles, USA

2015 – 2018 ***M.S.*** in Electrical and Computer Engineering
University of California, Los Angeles, USA

2011 – 2015 ***B.S.*** in Information Engineering
Zhejiang University, Hangzhou, China

Employment

2015 – 2022 Graduate Student Researcher
Device Research Laboratory, University of California, Los Angeles, USA

2020 Recording Media Research & Development Engineer Intern
Seagate Technology

Publications (*Equal contribution)

[1] **Quanjun Pan***, Yuting Liu*, Hao Wu, Peng Zhang, Hanshen Huang, Christopher Eckberg, Xiaoyu Che, Yingying Wu, Bingqian Dai, Qiming Shao, and Kang L Wang. "Efficient Spin-Orbit Torque Switching of Perpendicular Magnetization using Topological Insulators with High Thermal Tolerance." *Advanced Electronic Materials* (2022): 2200003.

[2] Xiaoyu Che*, **Quanjun Pan***, Božo Vareskic, Jingyi Zou, Lei Pan, Peng Zhang, Gen Yin, Hao Wu, Qiming Shao, Peng Deng, and Kang L Wang. "Strongly Surface State Carrier-Dependent Spin-Orbit Torque in Magnetic Topological Insulators." *Advanced Materials* 32, no. 16 (2020): 1907661.

[3] Qiming Shao*, Hao Wu*, **Quanjun Pan***, Peng Zhang, Lei Pan, Kin Wong, Xiaoyu Che, and Kang L. Wang. "Room temperature highly efficient topological insulator/Mo/CoFeB spin-orbit torque memory with perpendicular magnetic anisotropy." In *2018 IEEE International Electron Devices Meeting (IEDM)*, pp. 36-3. IEEE, 2018.

[4] Hao Wu, Jing Zhang, Baoshan Cui, Seyed Armin Razavi, Xiaoyu Che, **Quanjun Pan**, Di Wu, Guoqiang Yu, Xiufeng Han, and Kang L. Wang. "Field-free approaches for deterministic spin-orbit torque switching of the perpendicular magnet." *Materials Futures* (2022).

[5] Yu-Han Huang, Chao-Yao Yang, Chih-Wei Cheng, Albert Lee, Chih-Hsiang Tseng, Hao Wu, **Quanjun Pan**, Xiaoyu Che, Chih-Huang Lai, Kang-Lang Wang, Hong-Ji Lin, and

Yuan-Chieh Tseng. "A Spin-Orbit Torque Ratchet at Ferromagnet/Antiferromagnet Interface via Exchange Spring." *Advanced Functional Materials* (2022): 2111653.

[6] Hanshen Huang, Hao Wu, Tian Yu, **Quanjun Pan**, Bingqian Dai, Armin Razavi, Kin Wong, Baoshan Cui, Su Kong Chong, Di Wu, and Kang L Wang. "Electrical and optical characterizations of spin-orbit torque." *Applied Physics Letters* 118, no. 7 (2021): 072405.

[7] Yingying Wu, Gen Yin, Lei Pan, Alexander J. Grutter, **Quanjun Pan**, Albert Lee, Dustin A. Gilbert, Julie A Borchers, William Ratcliff, Ang Li, Xiao-dong Han, and Kang L Wang. "Large exchange splitting in monolayer graphene magnetized by an antiferromagnet." *Nature Electronics* 3, no. 10 (2020): 604-611.

[8] Kang L. Wang, Yingying Wu, Christopher Eckberg, Gen Yin, and **Quanjun Pan**. "Topological quantum materials." *MRS Bulletin* 45, no. 5 (2020): 373-379.

[9] Hao Wu, Deniz Turan, **Quanjun Pan**, Guanjie Wu, Seyed Armin Razavi, Nezih Tolga Yardimci, Zongzhi Zhang, Mona Jarrahi, and Kang L. Wang. "Picosecond spin-orbit torque switching of ferrimagnets." *arXiv preprint arXiv:1912.10129* (2019). (Under review)

[10] Hao Wu, Peng Zhang, Peng Deng, Qianqian Lan, **Quanjun Pan**, Seyed Armin Razavi, Xiaoyu Che, Li Huang, Bingqian Dai, Kin Wong, Xiufeng Han, and Kang L Wang. "Room-temperature spin-orbit torque from topological surface states." *Physical review letters* 123, no. 20 (2019): 207205.

[11] Hao Wu, Yong Xu, Peng Deng, **Quanjun Pan**, Seyed Armin Razavi, Kin Wong, Li Huang, Bingqian Dai, Qiming Shao, Guoqiang Yu, Xiufeng Han, Juan-Carlos Rojas-Sánchez, Stéphane Mangin, and Kang L Wang. "Spin-Orbit Torque Switching of a Nearly Compensated Ferrimagnet by Topological Surface States." *Advanced Materials* 31, no. 35 (2019): 1901681.

CHAPTER 1. Introduction

1.1 Magnetic Memory

Magnetic materials and their correlated phenomena, from the compass to modern spintronics, have been attractive to people since the dawn of humans.(*1*) A varieties of magnetic phenomena proceed on vastly different timescales, ranging from the magnetic patterns in a hard disk drive that stably store information against external perturbation without energy supply for tens of years down to the exchange interaction between electron spins that accelerates the switching of a magnet to a sub-picosecond regime.(*2*) These fascinating properties, together with the ever-growing demands for faster information processing speeds and larger data volumes to fuel Big Data, have been continuously pushing the frontier of modern magnetic applications, or spintronics devices as the central to this is the manipulation of the spin degree of freedom of electrons.

One critical milestone in the field of spintronics is the development of the modern magnetic-resistive random-access memory (MRAM), which will arguably revolutionize the contemporary architecture of memory systems. Historically, the MRAM is a new type of non-volatile memory developed based on the pioneering discovery of giant magneto-resistance (GMR)(*3*, *4*) and tunneling magneto-resistance (TMR)(*5*, *6*) and has shown tremendous potential in creating a universal memory and reforming the existing memory system based on the complementary metal-oxide-semiconductor (CMOS) technology.(*7*) The core component in MRAM is the magnetic tunnel junction (MTJ) which consists of two ferromagnetic layers separated by an insulating layer. An illustrative case of MTJ is shown in Figure 1-1.(*8–10*) Conceptually, when the magnetic moments of the two ferromagnetic films are aligned antiparallelly, the MTJ is in a high resistance state. In contrast, the MTJ is in a low resistance state when the magnetic moments are aligned parallelly. These binary resistance states can be utilized to magnetically encode the digital data ‘0’

and ‘1’, and handy readouts of the stored data can be achieved by passing a tunneling current vertically through the sandwich structure to probe the resistance states. This exploitation of both the magnetic and electronic properties in layered material structures can bring several groundbreaking functionalities to modern electronics in terms of read/write endurance, scalability, non-volatility, and power efficiency.(*11*) To date, MTJs have indeed opened up new perspectives not only for memory and data storage but also for high-performance magnetic sensors,(*12*) non-volatile programmable logic elements,(*13*, *14*) and brain-inspired applications.(*15*)

In practice, the magnetization of one layer (i.e., the fixed layer) always remains unchanged during operation, while the second layer (i.e., the free layer) can be switched between the two stable magnetic states. Therefore, data can be written into an MTJ by reversing the magnetization direction of the free layer, as illustrated in Figure 1-1. In order for the information stored in a miniaturized MTJ to remain highly non-volatile, a high energy barrier between the two magnetization states of the free layer is needed, which on the other hand, means a more considerable amount of energy is required to switch the magnetization during data writing. So far, in the quest to deliver high thermal stability for non-volatility, small feature size, and low power consumption concurrently, magnetic materials with easy-axis anisotropy, i.e., perpendicular magnetic anisotropy (PMA), have been strongly favored over those with easy-plane anisotropy for free layer.(*16*, *17*) Despite the rapid advances in MRAM in recent years, to compete with the current transistor-based memory devices and ultimately revolutionize the existing CMOS technology, the search for novel approaches and spintronic materials to manipulate magnetism with higher efficiency and speed is recognized as the central task in the development of MRAM and for the broader field of spintronics and modern magnetism.

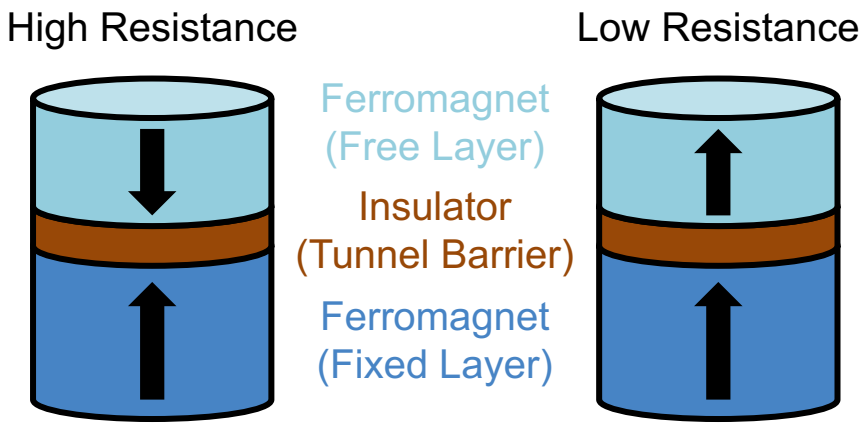

Figure 1-1. The illustrative basic structure of a magnetic tunnel junction (MTJ) with perpendicular magnetic anisotropy. The MTJ is a core component of modern spintronic devices. A typical MTJ consists of two ferromagnetic layers separated by an insulating layer. In an MTJ, a bit of data is stored by the relative alignment between the free layer and the fixed layer, or simply, the magnetization direction of the free layer. When the magnetizations of two ferromagnetic layers are aligned antiparallelly, the MTJ is in the high resistance state. When the magnetizations of two ferromagnetic layers are aligned parallelly, the MTJ is in the low resistance state. The resistance states can be read by passing a vertical tunneling current. For the development of high-performance MTJ, magnetic materials with perpendicular anisotropy are strongly preferred.

1.2 Spin-Orbit Torque Magneto-Resistive Random Access Memory

Spin-orbit torque is an exciting newly-discovered approach to electrically control magnetic moments, which has received extensive studies for developing next-generation MTJ in MRAM over the past decade.(*18–20*) The spin-orbit torque is generated by materials with strong spin-orbit coupling (SOC), which is described in the following Hamiltonian derived from the reduction of Dirac equation to non-relativistic limit:(*21*, *22*)

$$\widehat{H}_{\mathrm{SOC}} = \frac{\hbar}{2m_e c^2}(\boldsymbol{\nabla} V \times \widehat{\mathbf{p}}) \cdot \widehat{\boldsymbol{\sigma}} \tag{1-1}$$

where m_e is the electron mass, $\hbar$ is the reduced Planck's constant, and c is the speed of light. $\widehat{\boldsymbol{\sigma}}$ represents the vectorial Pauli-spin matrices, $\widehat{\mathbf{p}}$ is the momentum operator, and $\boldsymbol{\nabla} V$ is the local electric field experienced by the electron. As reflected in the above Hamiltonian of SOC, the electron momentum is directly coupled with the electron spin in SOC materials. Consequently, SOC gives rise to the spin-Hall effect in bulk materials(*23*, *24*), the Rashba-Edelstein effect at interfaces lacking structural inversion symmetry(*21*, *22*), and many other peculiar phenomena. Regardless of the underlying mechanism, when a charge current $\boldsymbol{J}_{\mathrm{C}}$ is injected through the SOC layer in a prototypical SOC material/magnetic material heterostructure, the moving electrons are deflected transversely depending on their spin direction, accumulating opposite spin on the opposite sides of the SOC material. Naturally, this can be seen as a spin current source, converting the charge current $\boldsymbol{J}_{\mathrm{C}}$ to a transverse spin current $\boldsymbol{J}_{\mathrm{S}}$ with an efficiency quantified using the effective spin-Hall angle (tangent) defined as(*18*)

$$\tan\theta_{\mathrm{SH}} = (2e/\hbar)\,|\boldsymbol{J}_{\mathrm{S}}|/|\boldsymbol{J}_{\mathrm{C}}| \tag{1-2}$$

Interfacing the SOC material with the magnetic material, this spin current transfers a considerable amount of spin angular momentum to the neighboring magnetic material, reorientating its magnetization direction. The influence of this spin current originating from the SOC on the magnetic layer can be treated as exerting so-called spin torques, or applying magnetic fields associated with the spin torques, onto the magnetic materials.(*25*) Given their origins in SOC, these spin torques and fields are called spin-orbit torque (SOT) and spin-orbit field (SOF), respectively. Throughout this dissertation, the terms SOF and SOT are often used interchangeably. There are two types of SOFs, namely, the damping-like SOF (DL-SOF) denoted as $\boldsymbol{H}_{\mathrm{DL}}$ and the field-like

SOF (FL-SOF) denoted as $\boldsymbol{H}_{\mathrm{FL}}$. The geometry of these SOFs is illustrated in Figure 1-2a and given by

$$\begin{aligned} \boldsymbol{H}_{\mathrm{DL}} &\approx \chi_{\mathrm{DL}}(\boldsymbol{J}_{\mathrm{C}} \times \boldsymbol{z}) \times \boldsymbol{m} \\ \boldsymbol{H}_{\mathrm{FL}} &\approx \chi_{\mathrm{FL}}(\boldsymbol{z} \times \boldsymbol{J}_{\mathrm{C}}) \end{aligned} \tag{1-3}$$

Here, $\boldsymbol{J}_{\mathrm{C}}$ is the charge current density passing through the SOC layer; $\boldsymbol{z}$ and $\boldsymbol{m}$ are unit vectors that denote the normal direction to the sample plane and the magnetization direction; χ_{DL} and χ_{FL} are the coefficients that normalize the strength of $\boldsymbol{H}_{\mathrm{DL}}$ and $\boldsymbol{H}_{\mathrm{FL}}$ to the charge current density, respectively.

The discovery of these current-induced SOFs has inspired an innovative write scheme for MTJ with PMA, leading to the development of a new category of MRAM, i.e., SOT-MRAM. In this SOT-based write scheme, the reversal of out-of-plane (OP) magnetic moments mainly relies on the current-induced $\boldsymbol{H}_{\mathrm{DL}}$ and requires an in-plane (IP) assisting field collinear with the injected current. The $\boldsymbol{H}_{\mathrm{DL}}$ and the IP assisting field jointly select one of the four equilibrium positions illustrated in Figure 1-2b. Accordingly, the magnetization can be switched between an ‘up’ state for data ‘1’ and a ‘down’ state for data ‘0’ by reversing the charge current direction given a fixed IP field direction. Noticeably, the polarity of such magnetization switching driven by the current-induced SOFs changes with the direction of the IP field. This dependence on an external magnetic, however, poses one of the most-recognized challenges to the development of SOF-based applications as the external fields inevitably interfere with many nano-electronic components and necessitates additional power consumption as well as auxiliary circuits. Motivated by this, several mechanisms, including the mirror symmetry breaking by structural asymmetry or magnetic exchange interactions, the combination of multiple spin torques, and the chiral symmetry breaking by tilted magnetic properties, have been proposed and offered numerous attractive research opportunities in addition to the search for novel spintronic materials.(*26*)

Nowadays, research into SOFs has become a thriving area of modern magnetism and spintronics because of its implications and prospects for higher operating speeds, lower energy consumption, and relaxed device designs.(*20*, *27*)

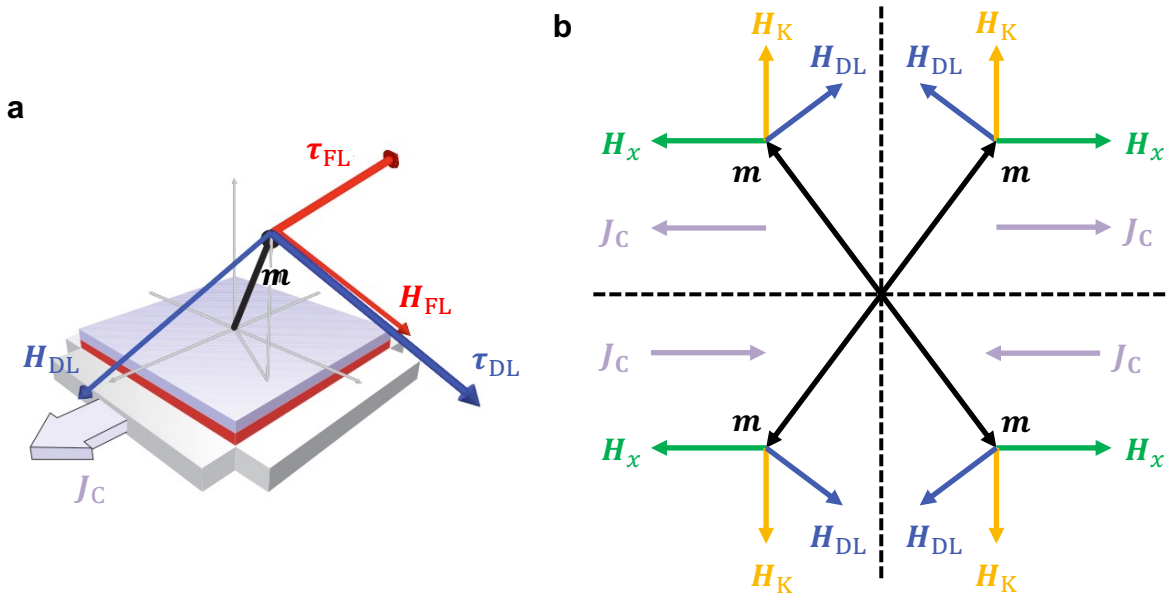

Figure 1-2. Spin-orbit field schematics and magnetization switching induced by spin-orbit fields with the assistance of an in-plane field. a. The geometry and orientation of the spin-orbit fields (i.e., $\boldsymbol{H}_{\mathrm{DL}}$ and $\boldsymbol{H}_{\mathrm{FL}}$) and the associate spin-orbit torques (i.e., $\boldsymbol{\tau}_{\mathrm{DL}} = \boldsymbol{m} \times \boldsymbol{H}_{\mathrm{DL}}$ and $\boldsymbol{\tau}_{\mathrm{FL}} = \boldsymbol{m} \times \boldsymbol{H}_{\mathrm{FL}}$) generated by an IP current injection with a density of $\boldsymbol{J}_{\mathrm{C}}$. The $\boldsymbol{m}$ is a unit vector that denotes the magnetization direction. **b.** Schematic of the stable magnetization state selected by the current-induced SOF alongside the IP assisting field H_x. The exact magnetization direction is given by the balancing among the external fields, i.e., $\boldsymbol{m} \parallel (\boldsymbol{H}_{\mathrm{DL}} + \boldsymbol{H}_x + \boldsymbol{H}_{\mathrm{K}})$. At a fixed H_x, reversing the direction of charge current leads to deterministic switching of the magnetization state. **a** is adapted from Ref. (*25*).

1.3 Emerging Spintronic Materials for Magnetic Memory

1.3.1 Topological insulator

Beyond the conventional SOC materials, such as heavy metal Ta,(*18*) Pt,(*28*) W(*29*), etc., an emerging material class with astonishingly strong SOC, topological insulators (TIs), has caught researchers' eyes in recent years.(*30*, *31*) While TI possesses a highly resistive bulk, it differs from ordinary insulators in many significant aspects. One of the most profound differences, due to the large SOC in TI, is that the energy gap of the insulating TI's bulk is inverted, which fundamentally changes the topological properties of the electronic band structure.(*32*, *33*) When a TI is in contact with a normal bandgap material or vacuum, the energy gap must close at the surfaces or interfaces as enforced by the continuity of wavefunctions, and unique topological surface states (TSSs) are thus formed. Rooted in the exotic band structure of TI (Figure 1-3a), these characteristic TSSs enjoy several fascinating properties:

1. While the bulk of TI is insulating, electrons are allowed to conduct on TI's "metallic" surface due to the bandgap closing in the TSSs. Moreover, the energy-momentum relationship of electrons (Figure 1-3a,b) in the TSS is linear as observed experimentally using angle-resolved photoemission spectrum (ARPES) measurements(*34*) and explained theoretically using an effective Dirac model.(*35*) Therefore, the surface electrons can be treated as massless Dirac fermions.
2. A more critical property derived from this effective Dirac model is the spin-momentum locking nature of the TSSs.(*35–37*) This means that for electrons in the TSSs, their spin directions always remain perpendicular to their momentum, as depicted in Figure 1-3a. Therefore, when these electrons flow directionally and generate currents, high spin polarization is guaranteed. As shown in Figure 1-3c, on the upper surface of TI, the forward-flowing current (red) contains

only the ‘up’ spin, whereas the backward-flowing current (blue) contains only the ‘down’ spin. And this polarity is reversed on the opposite surface.

3. Moreover, the TSSs are topologically protected by the time-reversal symmetry,(*38*) meaning the electron transport in the TSSs is immune to non-magnetic impurity scatterings or geometric perturbation. As shown on the right of Figure 1-3c, when the surface electrons encounter a non-magnetic impurity, there are only two paths for them to travel backward as the motion reversal is always accompanied by a reversal of the spin direction due to the spin-momentum locking. This spin rotation results in a quantum mechanical phase factor of –1 between the two back-scattering paths, and hence, causes destructive interference of the two paths.(*39*) Consequently, the electrons can only take a detour along the new surfaces/interfaces around the non-magnetic impurity without scattering and keep moving forward.(*39*)

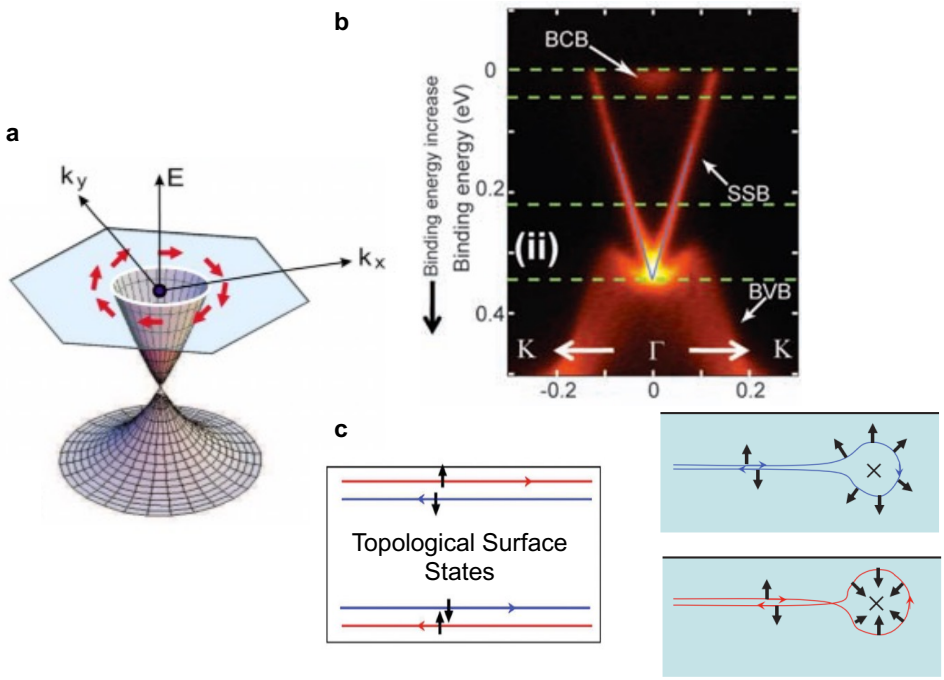

Figure 1-3. Topological insulator and its surface states. a. Schematic of the spin-polarized topological surface electronic band, where the red arrows denote spin direction; **b.** Experimental confirmation of the spin-momentum locking topological surface states by ARPES measurements;

c. Spin-momentum locking itinerate electrons in the topological surface states and prohibition of scattering by non-magnetic impurities due to the destructive interference between the two backward scattering paths as illustrated on the right of **c**. **a**, **b**, and **c** are adapted from Ref. (*33*); Ref. (*34*); Ref. (*39*), respectively.

Owing to the three features discussed above, when injecting a charge current into TI, a highly spin-polarized, low-dissipation current mainly conducted at the interfaces/surfaces is expected, making TI a promising candidate capable of delivering spin current with ultrahigh charge-spin conversion efficiency and significantly improving the energy performance of SOT-based spintronic memory and logic devices.

1.3.2 Ferrimagnet

Conventional spintronic devices have been predominately developed based on the control of ferromagnetism. In recent years, antiferromagnets (AFMs) have gradually emerged as a preeminent magnetic system for spintronics. AFMs own a variety of superior functionalities, including stability against external magnetic perturbations, virtually zero stray fields that prevent crosstalk between magnetic components, and most importantly, the ultrafast spin dynamics driven by the antiferromagnetic exchange interaction. Moreover, compared to ferromagnets (FMs), AFM orders are expected to be found in more material classes, given that they are permitted in every magnetic symmetry group, and there are more diversified arrangements of the magnetic sublattices to achieve a zero net magnetization.(*40*) While AFMs indeed represent a superior, diverse, and largely unexplored category of spintronic materials, the lack of net magnetic moments in AFMs, alongside the higher spin precession/resonance frequencies, makes it extremely challenging to

investigate AFMs using common magneto-transport or magnetic resonance techniques.(*41*) Therefore, at the frontier of developing ultrafast spintronic applications, ferrimagnets (FIM) which consist of inequivalent magnetic sublattices with an AFM-like arrangement have recently attracted considerable attention as FIM represents a class of intermediate materials between AFMs and FMs as shown in Figure 1-4a. As a result, FIMs uniquely combine the advantages of both FM and AFM,(*42*, *43*) which stem intrinsically from the two or more inequivalent and antiferromagnetically-aligned sublattices in FIMs. More specifically, the antiferromagnetic exchange interaction between the sublattices accelerates spin resonance frequencies and magnetization dynamics into the ultrafast terahertz range when the sublattices in FIMs are magnetically compensated like an AFM. Concurrently, unlike AFMs, the inequivalence between the sublattices gives rise to finite magneto-transport/-optical effects and element-specific signals even when the FIM is fully magnetically compensated, allowing for easy control and detection of the magnetic states in FIMs with well-established methods like those applied to FMs.

In addition to this unique combination of the AFM-like ultrafast spin dynamics and the FM-like easy accessibility to the internal magnetic states, the inequivalent sublattices also provide extra degrees of freedom for materials engineering and integrating of novel functionalities. It is well known that the properties of FIMs can be continuously tuned by varying their composition, i.e., the ratio between the constituent spin sublattices. The most exciting features of FIMs are the two types of compensating behaviors (Figure 1-4b): (1) Magnetization compensation (MC) point where $\sum_i x_i \boldsymbol{M}_i = 0$ (x_i and $\boldsymbol{M}_i$ denote the composition ratio and magnetization of the i-th sublattice in the FIM) is achieved. At this compensation condition, the net magnetization is nearly zero, resulting in a large coercivity field and high magnetic anisotropy energy; (2) Angular momentum compensation (AMC) point where $\sum_i x_i \boldsymbol{M}_i/\gamma_i = 0$ (γ_i denotes the gyromagnetic ratio

of the i-th sublattice in the FIM) is achieved, suggesting the total angular momentum of FIM vanishes while a finite net magnetic moment remains. Therefore, on approaching this angular momentum compensation point, the spin dynamics accelerate dramatically, as shown in Figure 1-4c, and the nonzero magnetic moment can still acutely couple to external fields.(*44*, *45*) Apparently, these compensation points can be reached by choosing proper compositions. In addition to tunning the composition, the two compensation conditions can also be met by varying the temperature, namely, reaching either the magnetization compensation temperature T_{MC} or the angular momentum compensation temperature T_{AMC} (Figure 1-4b). However, it should be noted that since the inequivalent sublattices have different gyromagnetic ratios, these two compensation conditions are generally not satisfied concurrently. Nevertheless, the unique combination of FM-like easy control/detection with the AFM-like ultrafast spin dynamics and the greater flexibility in material engineering highlights the potential of FIM as a near-term material platform for efficient and fast spintronic applications.

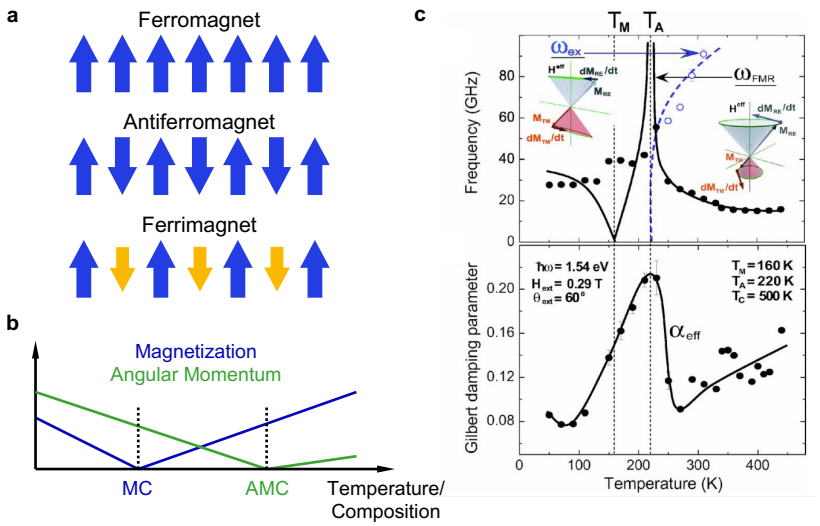

Figure 1-4. Ferrimagnets and their compensation points. a. Schematic of the alignment of magnetic moments in a ferromagnet (FM), an antiferromagnet (AFM), and a ferrimagnet (FIM); Compared to FMs and AFMs, FIMs uniquely consist of inequivalent magnetic sublattices and can

be viewed as a class of intermediate materials between AFMs and FMs; **b.** The two types of compensating behaviors in FIMs. The parameter can be either temperature or composition; **c.** Temperature dependence of the spin precession frequencies of a prototypical FIM GdFeCo. Spin dynamics are significantly accelerated near the angular momentum compensation point. **a** and **b** are adapted from Ref. (*43*) with modifications, and **c** is adapted from Ref. (*46*)

1.4 Magneto-Optical Characterization for Spintronic Materials

Light interacts with all kinds of magnetic materials or regular matters that are subjected to magnetic fields through a great number of magnetic-optical effects(*47*), offering ideal detection techniques for the field of magnetism. Among which, the magneto-optical Kerr effect (MOKE)(*48*) is one of the most extensively studied and is of great importance from both the fundamental science and application points of view. The MOKE describes the changes in the polarization of an electromagnetic wave upon reflected from a magnetic surface, as shown in Figure 1-5.(*48*)

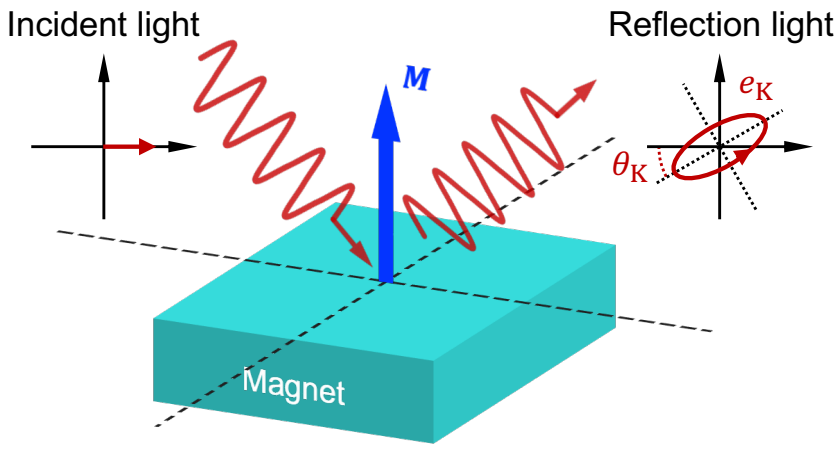

Figure 1-5. Illustration of the magneto-optical Kerr effect. The magneto-optical Kerr effect (MOKE) describes the changes to light reflected from materials with magnetic ordering or subject to an external magnetic field. Conceptually, upon interacting with and being reflected from a magnetized surface, the linearly polarized incident light is changed into an elliptically polarized

beam. The changes in the polarization of light, denoted by a Kerr rotation (θ_K) and a Kerr ellipticity (e_K), quantitatively contain the information of the magnetic sample. Generally, the MOKE signal is proportional to the $\boldsymbol{k} \cdot \boldsymbol{M}$, where $\boldsymbol{k}$ is the wavevector of the incident light, and $\boldsymbol{M}$ denotes the magnetization.

By measuring the changes in reflected light, the magnetic states of a material can be quantitively reconstructed. For decades, the applications of MOKE in studying magnetic media have been known for their high sensitivity, local probing/non-contact nature, and technological simplicity. Moreover, the magnetization and its associated dynamics can be optically probed with high spatial and temporal resolutions by incorporating various imaging/focusing optics and optical pump-probe techniques.(*2*, *49*, *50*) Particularly in the cases of exploring TIs as well as FIMs covered in this dissertation and addressing the unique challenges that come along, MOKE becomes even more appealing for the detailed reasons listed below

1. The exotic topological surface states, together with their strong dependence on the carrier concentration, the fermi level, and the bulk bands in TIs, convolute the electronic signals obtained using conventional electrical transport and ferromagnetic resonance (FMR) techniques. In this case, MOKE can serve as alternative access to the underlying electronic and magnetic states, providing additional insights into these materials.
2. The high frequencies inherent to ferrimagnetic spin dynamics, ranging from tens of gigahertzes to a few terahertzes, prohibit them from comprehensively characterized using conventional FMR techniques. Femtosecond laser pulses, on the other hand, are one of the shortest man-made events and enjoy the capability of probing magnetic dynamics on a timescale that corresponds to the shortest characteristics time of magnetic interactions. Indeed, the time-

resolved MOKE technique that incorporates the strength of ultrashort laser pulses with the sensitivity of MOKE offers a temporal resolution limited only by the pulse duration and the speed of light, allowing magnetic signals of up to several terahertzes to be measured at ease. Furthermore, unlike FMR, the time-resolved MOKE is a time domain technique capable of directly revealing the temporal trace of a magnetic process, especially for the magnetic response to an impulse.

3. To make the above issue worse for standard FMR techniques, the highest frequencies in FIMs is usually reached when the net magnetic moment is minimized, and the magnetic volumes of modern spintronic devices are typically on the scale of a few nanometers, posing additional challenges to standard FMR techniques. In contrast, the wavelength dependence and the superior surface sensitivity of MOKE can mitigate these issues.
4. Lastly, for many emerging spintronics materials, including topological insulators and low-dimension materials, how the device fabrication and the associated size effects can modify the material properties have received relatively limited investigation. While most FMR techniques and magneto-transport measurements require extra fabrication steps that might inevitably alter the material properties, MOKE measurements can be performed on pristine thin films. Additionally, by employing different imaging and focusing optics, the MOKE measurements can locally probe the materials and nanostructures (e.g., magnetic domains, magnetic skyrmions, etc.) with a high spatial resolution.

Given the important usage of MOKE-based detection techniques in this thesis, details regarding the formulation and experimental implementation of MOKE are discussed in Chapter 2.

1.5 Dissertation Outline

This dissertation consists of three parts centered around exploring the applicability of TIs and FIMs for efficient and fast magnetization manipulation and providing informative guidance and material information on developing next-generation SOT-based logic and memory spintronic devices. First, in Chapter 2, two custom-built MOKE-based detection techniques are introduced. One is designed to quantify the charge-spin conversion efficiency, while the other is for tracking the ultrafast dynamics. These techniques are essential for investigating the desired properties of TIs and FIMs and have been deployed to acquire the main experimental results presented in this dissertation. Chapter 3 covers two projects focusing on topological insulators. To begin with, systematic measurements of the charge-spin conversion efficiency of TI are presented, and the observed consistency among results obtained by fundamentally different detection techniques resolves the long-standing discrepancies regarding the efficiency of TI. Empowered by a better and more accurate understanding of TI, a TI/Mo/CoFeB/MgO structure with room temperature perpendicular magnetic anisotropy, efficient magnetization switching, and high thermal tolerance is developed, highlighting the vast potential of TI in improving the efficiency of applicable spintronics devices. Next, in Chapter 4, the basic dynamical properties of a novel ferrimagnetic structure, namely, GdFeCo with a vertical composition gradient, are characterized using the time-resolved MOKE technique. By conducting comprehensive fluence-dependent and field-dependent measurements, a previously unseen spin precession mode is found in the ferrimagnet with a vertical composition gradient. The main findings in Chapter 4 suggest a tremendous potential of ferrimagnets with a vertical composition gradient in realizing high-speed and efficient spintronic components. Finally, Chapter 5 concludes this dissertation and provides an outlook for future research.

CHAPTER 2. Magneto-Optical Kerr Effect Detection Techniques

2.1 Overview

To harness the merits of MOKE summarized in Section 1.4, two detection strategies based on MOKE and their experimental implementation are introduced in this chapter: (1) A SOF magnetometer based on MOKE (*51–53*) for probing the static magnetic properties and optically quantifying the charge-spin conversion efficiency of a material; (2) An all-optical pump-probe approach to access the dynamical magnetic information and transient magnetic states by measuring the time-resolved MOKE signals. In order to put both techniques into practice, a single experimental platform that integrates both measurement schemes has been established. This integrated experimental setup was primarily built based on the all-optical pump-probe scheme and has been used to acquire most of the experimental results presented in this thesis.

Chapter 2 starts with the basics and formulation of MOKE, followed by the introduction of two detection techniques mentioned above. Next, each technique's essential characteristics, theoretical considerations, experimental implementation, and instrumental setup are presented in detail. Note that this chapter focuses only on the most general and basic descriptions for these MOKE-based techniques, and the detection techniques are reviewed with additional details/modifications along with the specific research projects in the following chapters.

2.2 Magneto-Optical Kerr Effect

The magneto-optical Kerr effect (MOKE), which is the essence of the experimental techniques described in this chapter, manifests as the changes in the polarization of an electromagnetic wave upon reflected from a magnetic surface. The origin of MOKE can be phenomenologically explained in the context of dielectric tensor. Conceptually, any polarized light can be decomposed

into a left circularly polarized light and a right circularly polarized light. Upon interacting with a magnetic medium, in which the dielectric tensor contains non-zero antisymmetric, off-diagonal elements, the two circularly polarized components respectively undergo reflection with different phase shifts and absorption. As a result, the polarization of the reflected light is changed with respect to the incident light. Based on this interpretation, the MOKE produces several observables in the reflected light as shown in Figure 1-4: (1) the rotation of the polarization plane (of a linearly polarized light) or the principal axis (of a circularly polarized light); (2) the change in ellipticity; and (3) the modification of intensity. Here, the most common case, where the light source is linearly polarized, is adopted, and the rotation of the polarization plane, i.e., the Kerr rotation θ_{K}, is chosen as the target observable to implement the magneto-optical detection techniques. The Kerr rotation θ_{K} is approximately proportional to the projection of the magnetization $\boldsymbol{M}$ onto the wave vector $\boldsymbol{k}$ of the incident light, i.e., $\theta_{\mathrm{K}} \propto \boldsymbol{M} \cdot \boldsymbol{k}$. Therefore, a polar MOKE geometry with normal incidence (as shown in Figure 2-1) on a sample is employed for the experimental setup. This configuration is technically and experimentally preferred because of: (1) the technological interests and advances in magnetic materials with PMA; (2) the experimental simplicity, as will be discussed in detail in the next section.(*51*, *52*) With this experimental configuration, the θ_{K} adapts a simple form(*49*):

$$\theta_{\mathrm{K}} = f_{\perp} m_z + f_{\parallel} m_t m_l \tag{2-1}$$

where $f_{\perp}$ and $f_{\parallel}$ are the first- and second-order dimensionless magneto-optical coefficients that parameterize the coupling between the light and the magnetic moments; $\boldsymbol{m} = (m_x, m_y, m_z)$ is a normalized unit vector that denotes the magnetization direction (i.e., $\boldsymbol{m} = \boldsymbol{M}/|\boldsymbol{M}|$) and m_z is the OP component of $\boldsymbol{m}$, while m_l and m_t are the longitudinal and transverse IP components of $\boldsymbol{m}$ with respect to the polarization plane of laser(*49*), i.e.

$$\begin{cases} m_l = m_x \cos\varphi + m_y \sin\varphi \\ m_t = -m_x \sin\varphi + m_y \cos\varphi \end{cases} \tag{2-2}$$

and φ is the angle between the polarization plane of the laser and the x-axis; In principle, the first term $f_\perp m_z$ in Equation (2-1) is the linear contribution that stems from the polar MOKE and generally predominates the θ_K, while the second term $f_\parallel m_t m_l$ originated from the non-linear quadratic MOKE usually makes a minor contribution; Apparently, the quadratic MOKE contribution depends on the laser polarization while the polar MOKE does not, and hence, these two contributions can be separated by carrying out polarization-dependent experiments.

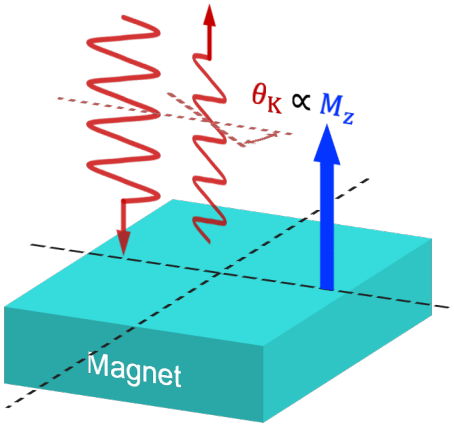

Figure 2-1. Polar magneto-optical Kerr effect configuration. The polar MOKE is the most frequently studied geometry for MOKE experiments. In the context of polar MOKE, the magnetic component of interest is parallel to the plane of incidence and normal to the sample/reflection surface. Near-normal angles of incidence and reflection are usually adapted as the polar MOKE signals dominate in this case, maximizing the signal given $\theta_K \propto \boldsymbol{M} \cdot \boldsymbol{k}$ (where $\boldsymbol{k}$ denotes the wave vector of the incident beam) while simplifying the experimental setup and data analysis. The blue arrow indicates the orientation of magnetization, and the red arrows indicate the propagation of sensing light.

Based on the above formulation and the preferred geometry, a critical task for deploying MOKE-based detection techniques is to precisely and quantitatively measure the rotation of the polarization plane of the reflected beam with respect to the incident beam. To this end, a detection module schematically shown in Figure 2-2 is built.(*49*)

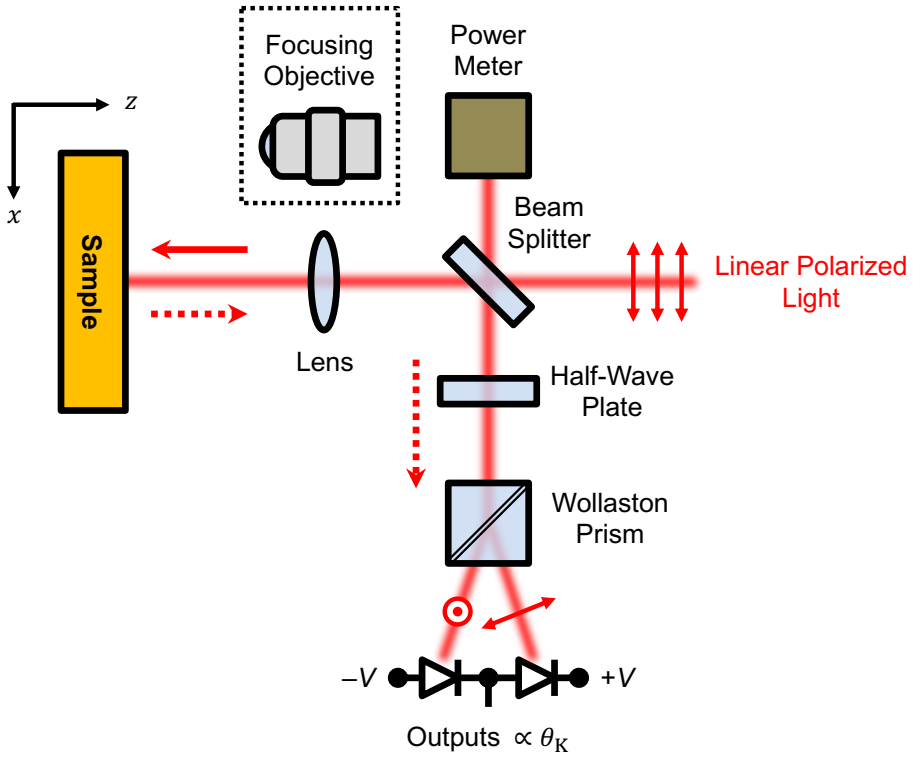

Figure 2-2. Schematic of the experimental implementation for measuring MOKE signals. This detection module and the optical layout are designed on the basis of polar MOKE, where the rotation of the principal axis of a linearly polarized light upon normally reflected from a magnetized sample surface is measured to quantitatively restructure the magnetic state of the sample. The module takes a linearly polarized beam as input, and a portion of the incident beam is reflected by a beam splitter into a power meter to monitor the intensity fluctuations. The remainder is used for probing and is focused normally onto the sample surface by a lens or a long working distance microscope objective. These focusing optics enable measurements to be performed on micro-devices (e.g., a 20 μm × 130 μm Hall bar structure). After that, the magnetic

states at the focused laser spot are locally probed via polar MOKE and are encoded in the reflected light. The reflected light is then collected by the same lens/microscope objective and directed by the beam splitter to where the polar MOKE signal is extracted and analyzed using a half-wave plate, a Wollaston prism, and a balanced photodetector. Here, the Wollaston prism is used to decompose the beam into two orthogonally polarized components, and the balanced photodetector outputs the difference between the two components, in which the polarization state of a linearly polarized light can be reconstructed. The half-wave plate is used for zeroing the signals.

Starting with a linearly polarized beam, the module is equipped with a lens mounted on a 3-axis optical translational stage to focus the beam normally into a spot size of ~100 μm in diameter on the sample surface. For measurements on micro devices (e.g., a 20 μm × 130 μm Hall bar structure) that require a finer spatial resolution, the lens can be replaced with a microscope objective which gives a spot size of ~5 μm. The magnetic states at the focused laser spot are locally probed via MOKE, and the beam carrying the magnetic information is reflected normally. Then, the reflected beam is collected by the same lens/microscope objective. Thereafter, a beam splitter directs the beam to where its Kerr rotation θ_{K} is extracted and analyzed using a half-wave plate, a Wollaston prism, and a balanced photodetector. Here, the Wollaston prism is used to decompose the beam into two orthogonally polarized components, and the balanced photodetector outputs the difference between the two components. In the small angle approximation, this output is linearly proportional to the Kerr rotation, and the half-wave plate is used for zeroing the signals. Meanwhile, the sample is mounted on a 3-axis translational stage with electrical connections and is placed in an electromagnet. The maximum field strength that can be applied along the z-direction is 0.5 T, and for fields applied within the sample plane, the field strength can reach 1.4 T. Note that the mounted

sample can also rotate freely around the z-axis. For low-temperature measurements, the sample is placed in a Janis® ST-100 optical cryostat with a temperature range of ~2 to ~500 K. Careful optical alignment was taken to assure normal incidence onto the sample plane in this detection module. To enhance the signal-to-noise ratio, the incident laser undergoes intensity/polarization modulation, and thus the output from the balanced photodetector can be denoised with lock-in amplifiers. With appropriate modulation, the Kerr rotation can be measured with an accuracy of ~1 μrad in most experiments. The details regarding the modulation and the associated lock-in techniques will be presented in the following sections for different MOKE detection techniques. In addition, a portion of the incident light is directed by the beam splitter to an optical power meter to monitor fluctuations in its intensity throughout the measurements.

2.3 Time-Resolved Magneto-Optical Kerr Effect Measurements

The detection module described above was then integrated with a femtosecond laser system and other necessary optics and optomechanical components into an ultrafast all-optical pump-probe setup. Conceptually, an intensive laser pulse is used as a pump to stimulate the sample bringing it into a highly non-equilibrium transient state and initiating a certain ultrafast dynamical process, while a weaker pulse is used to probe the sample state at the given time delay after the pump excitation. By recording the probe signals as a function of the time delay, the ultrafast dynamics and the highly non-equilibrium transient states can be reconstructed with an ultrashort temporal resolution, providing one of the most powerful tools to investigate the high-frequency behaviors of matters. Although this experimental platform was primarily built based on a pump-probe scheme, its flexible design and instrumental setup allow for other measurement schemes to be integrated as well.

As schematically shown in Figure 2-3a, this experimental platform is sourced by an amplified ultrafast Ti:Sapphire laser system. This laser system manufactured by *Spectra-Physics* can emit femtosecond pulses with extremely high pulse energy and consists of two core pieces: (1) a *Mai Tai SP* Ti:Sapphire oscillator that provides high-quality, transform-limited femtosecond pulses, and (2) a *Spitfire Ace* Ti:Sapphire regenerative amplifier that boosts the pulse energy by 5–6 orders. The *Mai Tai SP* laser delivers 35-fs laser pulses with a center wavelength of 800 nm at a repetition rate of 42 MHz. This train of femtosecond laser pulses is used to seed the *Spitfire Ace* amplifier, which outputs 35-fs laser pulses with a center wavelength of 800 nm and amplified pulse energy of 1 mJ at a repetition rate of 1 kHz. Immediately at the output, the laser pulses from *Spitfire Ace* are resized and attenuated and then split into two arms unequally using a 90:10 thin film beam splitter (BS1). The weaker beam serves as the probe and travels subsequentially through an optical delay stage, a pair of linear polarizers that keep the light linearly polarized and enable handy adjustment of the probe intensity, and finally, enters the detection module described in Section 2.2 to monitor the magnetic states of samples via polar MOKE. In comparison with Figure 2-2, the additional half-wave plates HWP1 and HWP2 in Figure 2-3a are used to compensate for the nonnegligible polarization responses from the beam splitter as well as the focusing optics and control the polarization direction of the linearly polarized probe pulses, respectively.(*52*) The more intensive beam from BS1 is used as the pump to excite the sample, and therefore, it travels through a simpler optical path in order to minimize additional attenuation and potential damage to the optics. The two polarizers and the half-wave plate (i.e., LP3, LP4, and HWP4 in Figure 2-3a) on this pump arm function similarly to those on the probe arm. Given the high pulse energy provided by *Spitfire Ace*, two ultrafast thin plano-convex lenses with focal lengths of 200 mm and 250 mm are selected to respectively focus down the probe and pump beams to ~100 μm spots on the sample.

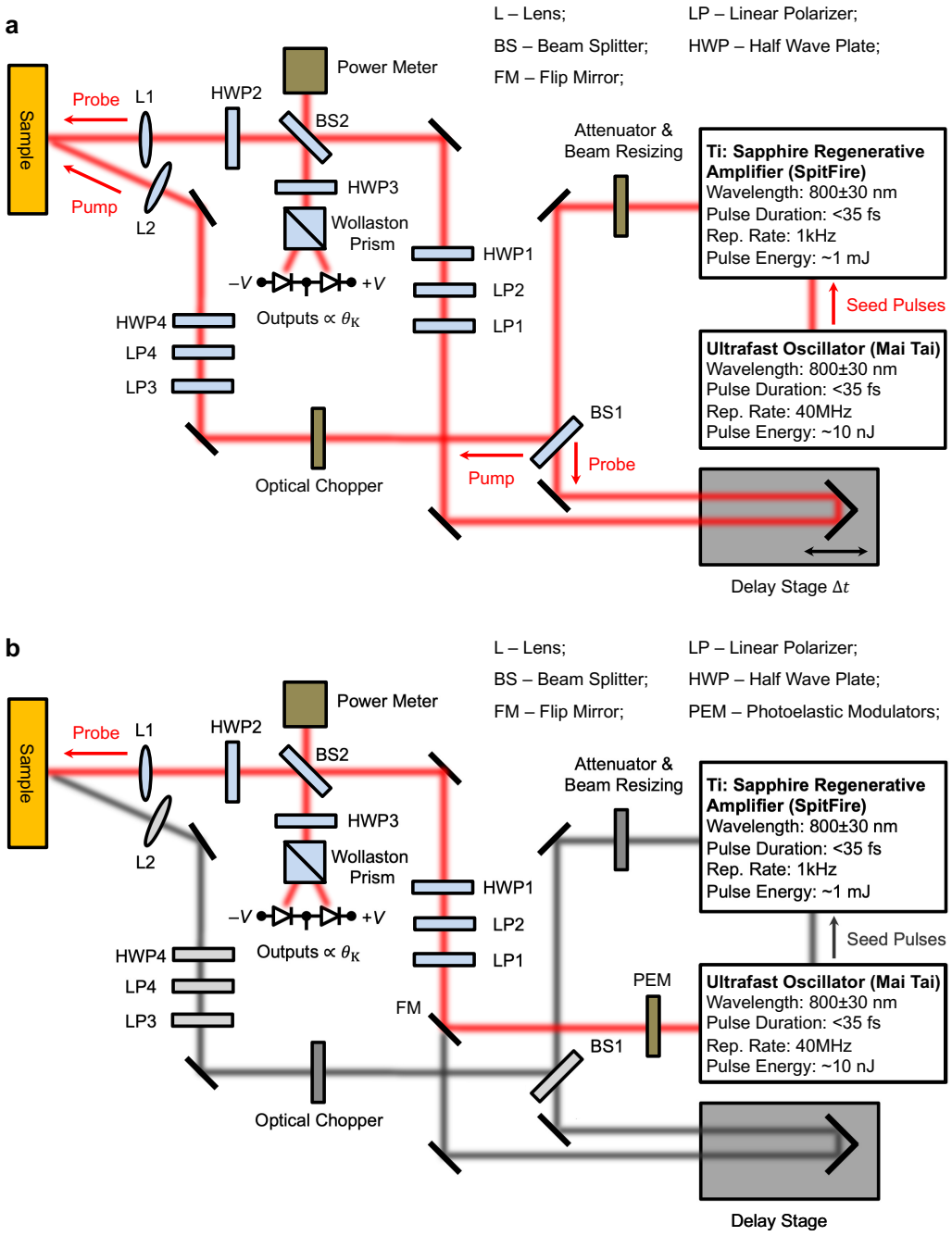

Figure 2-3. Schematic of the femtosecond laser-based magneto-optical platform. a. Experimental setup and optical layout for the all-optical time-resolved pump-probe technique described in Section 2.3; **b.** Experimental setup for the statice MOKE measurements and optical quantification of spin-orbit field (MOKE spin-orbit field magnetometer) described in Section 2.4. Note that the optical layout in **b** is built by reusing much of **a**, and the unused parts are grayed out.

Therefore, the two measurement schemes are compactly integrated into a single optical platform where the conversion from **a** to **b** is completed by deploying a flip mirror that externally switches the system light source from *SpitFire Ace* to *Mai Tai* and adding a photo-elastic modulator. This design requires minimal realignment of optics and adds experimental flexibility to allow for rapid and comprehensive characterization of materials' spintronic properties by combining various optical measurements.

The difference in focal lengths results in a smaller probe spot than the pump spot, ensuring uniform excitation in the measurement area once careful optical alignment is taken so that the pump and the probe overlap. As depicted in Figure 2-3a, while the probe is at normal incidence, the pump makes a slight angle with respect to the film normal, i.e., z-axis. This incident angle can be varied from nearly 0 degrees to 16 degrees from the z-axis by adjusting the focusing lens or the last mirror on the pump arm. An optomechanical delay stage with a retro-reflector is placed in the probe arm and change the optical path length of the probe arm to introduce and control the time delay between the pump and the probe. This delay stage has a maximum translation distance of ~150 mm, corresponding to a time delay of ~1 ns. To isolate the pump-induced signals, an optical chopper is deployed to modulate the pump arm, and hence, feeding the outputs of the photodetector into a lock-in amplifier (*SR830* by Stanford Research Systems Inc.) that is locked to the frequency of the optical chopper yields only the pump-induced signals with low noise.

2.4 Static MOKE Magnetometer and Optical Quantification of Spin-Orbit Field

While this experimental platform is implemented based on an all-optical pump-probe scheme, it can be conveniently modified to adapt to other measurement schemes. Another useful

experimental setup incorporated into this platform is the MOKE spin-orbit field magnetometer first developed in Ref. (*51*). This optical magnetometer is a valuable tool for characterizing static magnetic properties and quantifying the spin-orbit fields.

Unlike the pump-probe scheme, only one beam is needed in this case. A flip mirror (denoted by FM in Figure 2-3b) is used to guide the direct outputs from *Mai Tai* to source the setup, as shown in Figure 2-3b. The direct outputs from *Mai Tai* are more suitable for measuring the static magnetic properties and the spin-orbit fields because:

1. The repetition rate of *Mai Tai* is 42 MHz which is considerably higher than that of *SpitFire Ace*, and therefore, enables high-frequency modulation that can significantly enhance the sign-to-noise ratio; Note that the repetition rate of *Mai Tai* (42 MHz) exceeds the limit of the *SR830* lock-in amplifier (100 kHz), and therefore, an external modulator (i.e., the photo-elastic modulator, or PEM, in Figure 2-3b) is needed.
2. As the high energy pulses (~1 mJ) from *SpinFire Ace* can damage the optics more easily when focusing, the lower pulse energy (~1 nJ) of *Mai Tai* allows for tighter focusing with microscope objective such that the experiments can be performed on patterned micro-size devices, which is generally required for generating spin-orbit fields by charge current injection, or on low-dimensional materials with small sample sizes. With a typical 20× long working distance microscope objective, a spot size <5 μm in diameter can be achieved on the sample.
3. Most of the emerging quantum materials and low-dimensional materials are vulnerable to laser excitation and only manifest their exotic properties at cryogenic temperatures. Thus, the lower pulse energy of *Mai Tai* can better prevent unwanted damage and minimize the influence of local heating on the materials.

In principle, the MOKE spin-orbit field magnetometer operates based on the current-driven macroscopic magnetization oscillation via SOF,(*51*) which is also the essence of the widely-used 2nd-harmonic measurements for quantifying spin-orbit fields.(*54*) In the presence of an a.c. current, the SOFs produced by SOC materials (e.g., heavy metals, topological insulators) oscillate the magnetic moments around their equilibrium position, as illustrated in Figure 2-4a. This magnetization oscillation gives rise to current-induced changes in the Kerr angle ($\Delta\theta_{\mathrm{K}} = J_{\mathrm{C}}\frac{\partial\theta_{\mathrm{K}}}{\partial J_{\mathrm{C}}}$ where J_{C} is the amplitude of the a.c. charge current), and hence, the information about SOFs is optically encoded into $\Delta\theta_{\mathrm{K}}$ for subsequent quantification. The detailed relation between SOFs and $\Delta\theta_{\mathrm{K}}$ can be derived from the quasi-equilibrium condition given by $\boldsymbol{m}\times\boldsymbol{H}_{\mathrm{eff}} = \left(\boldsymbol{m}_0 + J_{\mathrm{C}}\frac{\partial\boldsymbol{m}}{\partial J_{\mathrm{C}}}\right)\times \left(\boldsymbol{H}_0 + J_{\mathrm{C}}\frac{\partial\boldsymbol{H}_{\mathrm{eff}}}{\partial J_{\mathrm{C}}}\right) = \boldsymbol{0}$ where $\boldsymbol{m}_0$ and $\boldsymbol{H}_0$, respectively, denote the equilibrium values of $\boldsymbol{m}$ and $\boldsymbol{H}_{\mathrm{eff}}$ in the absence of in-plane a.c. current injection (i.e., in the absence of SOFs-driven magnetization oscillation). Apparently, it has $\boldsymbol{m}_0\times\boldsymbol{H}_0 = 0$ and the equilibrium condition can thus be reduced to

$$\left(\boldsymbol{m}_0\times\frac{\partial\boldsymbol{H}_{\mathrm{eff}}}{\partial J_{\mathrm{C}}} + \frac{\partial\boldsymbol{m}}{\partial J_{\mathrm{C}}}\times\boldsymbol{H}_0\right) = 0 \qquad (2\text{-}3)$$

In a commonly adapted experimental configuration where both the a.c. current and the external magnetic field point along the x-axis, the total effective field exerted on the sample magnetization:

$$\boldsymbol{H}_{\mathrm{eff}} = \boldsymbol{H}_0 + \boldsymbol{H}_{Oe} + \boldsymbol{H}_K + \boldsymbol{H}_{\mathrm{FL}} + \boldsymbol{H}_{\mathrm{DL}} = H_x\cdot\boldsymbol{x} + H_{\mathrm{Oe}}\cdot\boldsymbol{y} + H_{\mathrm{K}}m_z\cdot\boldsymbol{z} + \boldsymbol{H}_{\mathrm{FL}} + \boldsymbol{H}_{\mathrm{DL}} \qquad (2\text{-}4)$$

where $\boldsymbol{H}_0 = H_x\cdot\boldsymbol{x}$ is the applied magnetic field; $\boldsymbol{H}_{\mathrm{Oe}} = H_{\mathrm{Oe}}\cdot\boldsymbol{y} = \chi_{\mathrm{Oe}}\cdot J_{\mathrm{C}}\cdot\boldsymbol{y}$ is the Oersted field generated at the device center by the current pulses; $\boldsymbol{H}_K = H_{\mathrm{K}}m_{\mathrm{z}}\cdot\boldsymbol{z}$ represents the effective anisotropy field; $\boldsymbol{H}_{\mathrm{FL}}$ and $\boldsymbol{H}_{\mathrm{DL}}$ are the damping-like spin-orbit field and field-like spin-orbit field, respectively. When $H_x \gg H_{\mathrm{K}}$, $\boldsymbol{m}_0$ is aligned along the x–axis and can be approximated as $(1,\ 0,\ 0)$. In this case, $\boldsymbol{H}_{\mathrm{FL}}$ points along the y-axis and can be expressed as $\chi_{\mathrm{FL}}\cdot J_{\mathrm{C}}\cdot\boldsymbol{y}$ while $\boldsymbol{H}_{\mathrm{DL}}$ points along the z-axis and can be expressed as $\chi_{\mathrm{DL}}\cdot J_{\mathrm{C}}\cdot\boldsymbol{z}$ based on Equation (1-3).

Substituting these expressions of $\boldsymbol{H}_{\mathrm{FL}}$ and $\boldsymbol{H}_{\mathrm{DL}}$ into Equation (2-4) and the term $\frac{\partial \boldsymbol{H}_{\mathrm{eff}}}{\partial J_{\mathrm{C}}}$ in Equation (2-3) acquires the form below:

$$\frac{\partial \boldsymbol{H}_{\mathrm{eff}}}{\partial J_{\mathrm{C}}} = \left(0, \quad \chi_{Oe} + \chi_{\mathrm{FL}}, \quad H_{\mathrm{K}} \frac{\partial m_z}{\partial J_{\mathrm{C}}} + \chi_{\mathrm{AL}}\right) \tag{2-5}$$

Thereby replacing the associated terms in Equation (2-3) with the result of Equation (2-5), $\boldsymbol{m}_0 = (1, \quad 0, \quad 0)$, and $\boldsymbol{H}_0 = (H_x, \quad 0, \quad 0)$ to solve for $\frac{\partial \boldsymbol{m}}{\partial J_{\mathrm{C}}}$ yields:

$$\begin{cases} \dfrac{\partial m_y}{\partial J_{\mathrm{C}}} = \dfrac{\chi_{\mathrm{Oe}} + \chi_{\mathrm{FL}}}{H_x} \\ \dfrac{\partial m_z}{\partial J_{\mathrm{C}}} = \dfrac{\chi_{\mathrm{DL}}}{|H_x - H_{\mathrm{K}}|} \end{cases} \tag{2-6}$$

By substituting these results into $\Delta\theta_{\mathrm{K}} = J_{\mathrm{C}} \frac{\partial \theta_{\mathrm{K}}}{\partial J_{\mathrm{C}}} = J_{\mathrm{C}} \frac{\partial}{\partial J_{\mathrm{C}}} (f_{\perp} m_z + f_{\parallel} m_t m_l)$ where m_t and m_l are given by Equation (2-2) will reach:

$$\Delta\theta_{\mathrm{K}} = \frac{f_{\perp} H_{\mathrm{DL}}}{|H_x - H_{\mathrm{K}}|} + \frac{f_{\parallel}(H_{\mathrm{Oe}} + H_{\mathrm{FL}})}{H_x} \cos 2\varphi \approx \frac{\theta_{\mathrm{S}} H_{\mathrm{DL}}}{|H_x - H_{\mathrm{K}}|} \tag{2-7}$$

where φ is the polarization angle of incident laser defined as the angle between the polarization plane of incident laser and x-axis. Note that the second term (from the quadratic MOKE) in Equation (2-7) can be reasonably neglected when $H_{\mathrm{K}} > 0$ and $f_{\perp} \gg f_{\parallel}$ for magnetic materials with strong PMA. According to Equation (2-1), $f_{\perp}$ can be approximated as the saturation Kerr rotation (θ_{S}) extracted from the OP optical hysteresis loop as shown in Figure 2-4c. Based on the formulation in Equation (2-7), a MOKE-based SOF magnetometer with the normal incidence geometry was implemented. As schematically illustrated in Figure 2-4b, a laser beam from *Mai Tai* is linearly polarized and incidents perpendicularly onto the sample. A 20× microscopic objective is deployed to focus the laser into a 5 μm × 5 μm spot, where the magnetization and spin dynamics are probed. The same detection module described in Section 2.2 is used to extract the

total Kerr rotation with the a.c. current modulation. In this case, the output voltage signals from the photodetector are $\propto \cos(\omega_1)\,[\theta_{\mathrm{K}} + \cos(\omega_2)\,\Delta\theta_{\mathrm{K}}]$ where ω_1~100 kHz is the frequency of the PEM that modulates the laser intensity and ω_2~673 Hz is the frequency of the a.c. current with no d.c. offset. With this modulation, it is handy to extract θ_{K} and $\Delta\theta_{\mathrm{K}}$ with two consecutive lock-in amplifiers. In particular, the first lock-in amplifier locks to the reference frequency at ω_1 to yield the magnitude of θ_{K} and the second lock-in amplifier was locked to another reference frequency at ω_2 and outputs the magnitude of $\Delta\theta_{\mathrm{K}}$. To demonstrate the equivalence between this optical approach and the well-established 2nd-harmonic transport approach for quantifying SOFs, as these two approaches are developed on the same basis of the SOF-driven magnetization oscillation, both measurements were also conducted simultaneously on a prototypical ferromagnetic sample with robust PMA, and the results obtained with J_0~1.2×10^5 A cm^{-2} under IP field scan are presented in Figure 2-4c&d. Given that both the optical and transport signals originate from the SOF-driven magnetization oscillation, these results unsurprisingly show an excellent agreement as the following relation(*51*, *54*)

$$\frac{\Delta\theta_{\mathrm{K}}}{\theta_{\mathrm{S}}} \approx \frac{H_{\mathrm{DL}}}{|H_x - H_{\mathrm{K}}|} \approx -2\,\frac{R_{\mathrm{AHE}}^{2\omega}}{R_{\mathrm{S}}} \tag{2-8}$$

This clear consistency between the transport and optical results firmly validates the formulation, usage, and relevance of the MOKE-based SOF magnetometer for investigating SOF-related phenomena. Furthermore, compared to the magneto-transport techniques, this optical technique employs two different modulation frequencies (ω_1~100 kHz and ω_2~673 Hz) so that the optical signals ($\Delta\theta_{\mathrm{K}}$) are purely linear in current density and minimize the contributions from other effects (e.g., Joule heating, asymmetric magnon scattering) that are in higher orders of the current density.

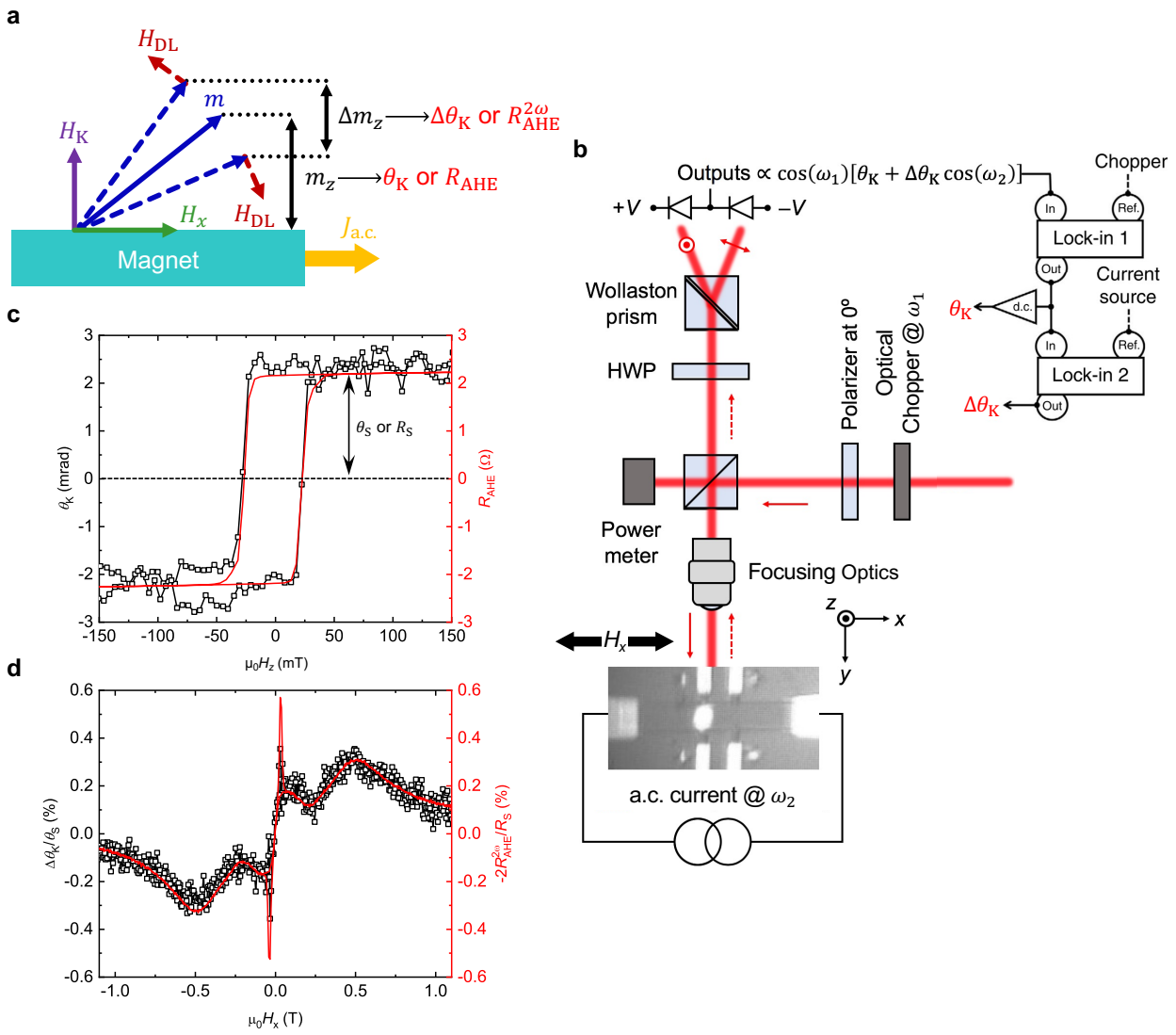

Figure 2-4. Optical quantification of spin-orbit torques. a. The schematics show the geometry of the magnetic fields involved in the measurement. An a.c. current injection oscillates the magnetic moments (denoted by Δm_z) by generating spin-orbit fields. The perpendicular magnetic components (m_z) are linearly reflected by θ_K (optical signals) or R_{AHE} (transport signals), while the SOF-driven magnetization oscillations along the OP direction are linearly reflected as $\Delta\theta_K$ or $R_{AHE}^{2\omega}$. **b.** Schematic drawing of the experimental setup for the MOKE SOF magnetometer; **c.** Comparison between OP hysteresis loops measured by the optical and transport. The saturation Kerr rotation θ_S and saturation anomalous Hall resistance R_S can be extracted from these OP

hysteresis loops. **d.** Direct comparison between the current-driven dynamical magnetic signals (i.e., $\Delta\theta_{\mathrm{K}}$ and $R_{\mathrm{AHE}}^{2\omega}$), which encode the information about SOTs, from the magneto-optical Kerr measurements and magneto-transport Hall measurements. The optical and transport signals both originated from macroscopic magnetization oscillation and agreed well with each other. Figure 2-4 is adapted from Ref. (*55*) (Q. Pan's publication).

CHAPTER 3. Topological Insulator-Based Magnetic Structures for Efficient Magnetization Switching through Spin-Orbit Field

3.1 Overview

Since its discovery, TI has been extensively studied for both generic condensed matter physics and applied spintronics.(*56*) It has been demonstrated that the strong spin-orbit coupling in TI leads to full spin-momentum locking in its topological surface states and suppresses electron scattering from non-magnetic impurities.(*33*) These properties make TIs an ideal spin current source for generating SOFs with an energy efficiency unmatched by conventional heavy metals. The TI-based magnetic heterostructures have thus been envisioned as a promising building block for next-generation high-performance spintronic memory and logic devices. Whereas the amplitudes of SOFs, as well as the charge-spin conversion efficiencies in TIs measured by a variety of conventional electrical means, show apparent inconsistencies, and the interpretation of these results was also controversial. This disagreement unavoidably makes it more difficult to comprehend the fundamentals of SOC-related phenomena in TIs and the subsequent development of TI-based spintronic devices.

With aims to tackle these problems, Chapter 3 begins with exploiting the capability of the MOKE detection technique described in Chapter 2 to quantify TI's charge-spin conversion efficiency directly. More specifically, the θ_{SH} as defined by Equation (1-2), which is the figure of merit for charge-spin conversion of a SOC material, is investigated using the MOKE SOF magnetometer (see Section 2.4) for a prototypical magnetically-doped TI/TI bilayer sample. Unlike the previous transport signals, the experimental results by MOKE measurements evidently originated from SOFs. These optical results are further compared with those independently obtained by measuring the current-induced shifts in the hysteresis loop, and quantitative consistency is achieved, revealing

that both measurement schemes can provide reliable and quantitative results for unraveling the SOC-related physics in TI-based structures. Empowered by the established technique for quantifying the strength of SOC, subsequent studies on how temperature and carrier concentration affect the charge-spin conversion efficiency of TI considerably resolve the wide discrepancies among the earlier reports. Moreover, the unprecedentedly large θ_{SH} in TI is solidly confirmed, and a critical role of the TSSs in generating giant SOFs is also elucidated.(*57*)

With these insights into the TSSs and SOFs in TI, however, a key question that remains is whether TI is truly applicable to and can greatly innovate the spintronics devices that are required to operate at room temperature, given that most of the previous research related to TI is limited to cryogenic temperature. Although this concern has been partly mitigated by the recent advances in the development of TI-FM heterostructures at room temperature, promising an innovative avenue in spin-orbit torque non-volatile magnetic memory and low dissipation electronics. However, direct integration of TIs with perpendicularly magnetized ferromagnet while retaining an extraordinary charge-spin conversion efficiency (θ_{SH} >100%), remains a major challenge. In addition, the indispensable thermal compatibility with modern CMOS technologies has not yet been demonstrated in TI-based structures. In the second part of Chapter 3, the high-quality integration of a perpendicularly magnetized CoFeB/MgO system with TI was achieved by adding a Mo insertion layer, and efficient current-induced magnetization switching at ambient temperature was demonstrated. The calibrated energy efficiency of TIs is at least one order of magnitude larger than those found in heavy metals. Moreover, it was demonstrated that the perpendicular anisotropy of the integrated CoFeB/MgO system and the current-induced magnetization switching behavior are well-preserved after annealing at >350 °C, offering a wide temperature window for thermal treatments. This thermal compatibility with the modern CMOS back-end-of-line process, high-

quality integration with the technically preferred magnetic system, and low energy consumption switching at room temperature in these TI-based structures pave the way toward TI-based low-dissipation spintronic applications.

3.2 Magneto-Optical Determination of Spin-Orbit Torque in a Magnetically Doped Topological Insulator Heterostructure

With a particular focus on the intrinsic properties of TI and physics related to SOFs, bilayer TI/Cr-doped TI heterostructure consists of two quintuple layers of $Bi_xSb_{2-x}Te_3$ on top and five quintuple layers of Cr-doped $Bi_xSb_{2-x}Te_3$ at the bottom was selected for the study in this section. The sample was grown by molecular beam epitaxy (MBE) on insulating GaAs(111) substrates. The introduction of uniform Cr dopant into the lower TI layers establishes a robust ferromagnetic order, which is developed through the bulk van Vleck mechanism and/or surface carrier-mediated magnetism(*58*). Using the detection technique covered in Section 2.2, the MOKE responses of the sample to OP and IP magnetic fields at 12 K are shown in Figure 3-1a, manifesting the more pronounced ferromagnetism and more robust perpendicular anisotropy compared to other magnetically-doped topological insulators. When the applied external field is along the OP direction, the magnetization saturates when $\mu_0 H_z$ > 100 mT, and the coercivity field H_C is estimated to be ~4 mT. The OP hysteresis loops were also characterized at different temperatures using both the MOKE magnetometer and a superconducting quantum interference device (SQUID). The temperature dependence of the saturation Kerr rotation θ_S and the saturation magnetization M_S are summarized in Figure 3-1b, from which the Curie temperature is estimated to be ~27 K. Note that the saturation magnetization was obtained from SQUID measurements conducted on a thicker sample (~50 nm) with identical growth conditions. The temperature dependence of θ_S

extracted from the $\theta_K - H_z$ curves is in excellent agreement with that of saturation magnetization M_S, and the relationship between θ_S and M_S strongly suggests that the MOKE signals are most sensitive to and remain linearly proportional to the OP component of magnetization. Therefore, the θ_K serves as a direct probe to the OP magnetization in the following sections.

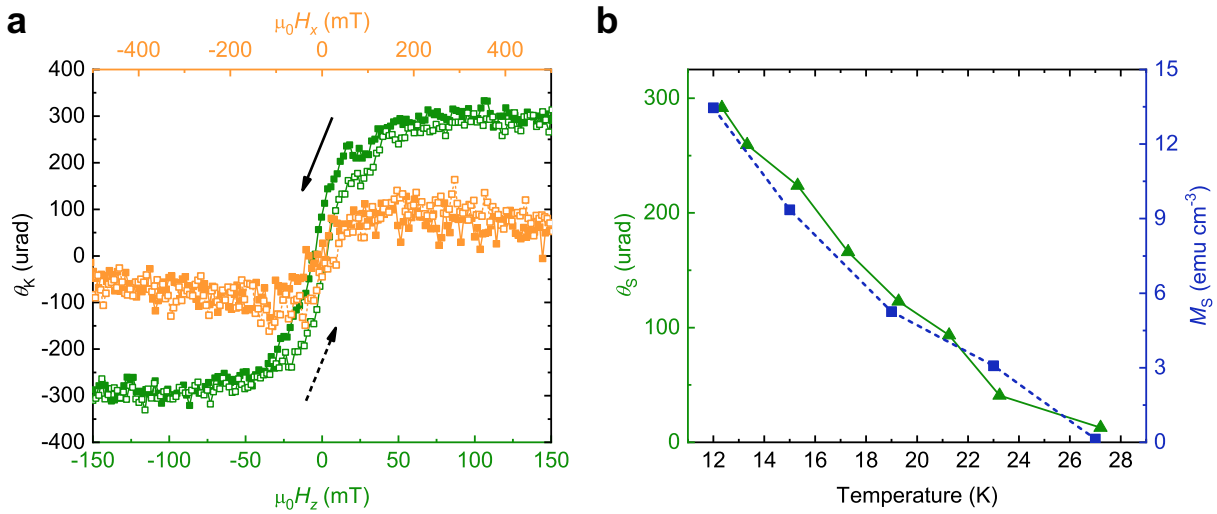

Figure 3-1. Magnetic properties of the TI/Cr-doped TI bilayer structure. a. The Kerr rotation θ_K as functions of OP and IP external fields with respect to the sample plane at 12 K. The TI/Cr-doped TI bilayer structure exhibits ferromagnetism with perpendicular magnetic anisotropy. **b.** The temperature dependence of saturation Kerr rotation (θ_S) and saturation magnetization (M_S) extracted from the OP hysteresis loops. The θ_S is obtained using the static MOKE setup described in Section 2.2 and the M_S is extracted from SQUID measurements conducted on a thicker sample (~50 nm) with identical growth conditions.

To evaluate the efficiency of current-induced SOFs in TIs, the films were then patterned into 50 μm × 800 μm Hall bar devices by standard photolithographic and dry etching techniques. Owing to the TSSs in TI, an IP charge current injected into the heterostructure conducts on the top and bottom surfaces of the bilayer structure and becomes highly spin-polarized. As a result of the Cr

dopant-introduced structural asymmetry, the top and bottom spin-momentum locking TSSs produce non-equal SOFs; hence, a non-zero net SOF tilts the magnetic moments of the Cr-doped TI off their equilibrium position. As depicted in Figure 3-2, if an a.c. IP current is applied, the alternating SOF will oscillate the magnetic moments (i.e., Δm_z), and hence, will be reflected as current-induced modulations to the Kerr rotation θ_{K}. Accordingly, the strength of SOF and the charge-spin conversion efficiency in TIs can be evaluated from these current-driven modulations to θ_{K} based on the technique introduced in Section 2.4 and Ref. (*51*).

In brief, as introduced in Section 1.2 and defined in Equation (1-3), there are two types of SOFs, the DL-SOF $\boldsymbol{H}_{\mathrm{DL}} \approx \chi_{\mathrm{DL}}(\boldsymbol{J}_{\mathrm{C}} \times \boldsymbol{z}) \times \boldsymbol{m}$ and the FL-SOF $\boldsymbol{H}_{\mathrm{FL}} \approx \chi_{\mathrm{FL}}(\boldsymbol{z} \times \boldsymbol{J}_{\mathrm{C}})$. Based on this expression of $\boldsymbol{H}_{\mathrm{DL}}$, the DL-SOF always remains perpendicular to the magnetic moments so that it is capable of efficiently rotating the magnetic moment in the plane defined by the direction of injection current and the direction of sample norm, and it is of primary interest for applicative SOT-switching devices. The following sections will mainly focus on the $\boldsymbol{H}_{\mathrm{DL}}$. By adapting the experimental configuration described in Section 2.4 (i.e., both the a.c. current and the external field are applied along the x-axis) to optically measure $\boldsymbol{H}_{\mathrm{DL}}$, a quantitative relationship between the optical signals and the SOFs as derived in Equation (2-7) is established. This experimental configuration is summarily presented in Figure 3-2. Noticeably, the precession frequency of Cr-doped TI is on the order of a few GHz which is much higher compared to the frequency of a.c. current (~673 Hz) that drives the magnetization dynamics during the measurements. For this reason, it is safe to assume the magnetization in Cr-doped TI adiabatically follows the overall effective field that includes an applied magnetic field H_x, effective perpendicular anisotropy field $\boldsymbol{H}_{\mathrm{K}}$, and current-induced DL-SOF $\boldsymbol{H}_{\mathrm{DL}}$. The Oersted field is estimated to be <0.1 Oe at the maximum current density applied in the measurements, and thus, its influence is omitted here. Due

to the low Curie temperature of Cr-doped TI, the devices were placed inside a cryostat, where the major measurements were conducted and cooled down to 12K using liquid helium flow. This temperature has taken into account the influence of the local heating effect from the laser and thermal radiation through the optical window, which is achieved by careful calibration based on the comparison between the shapes of optical hysteresis loops and magnetic hysteresis loops.

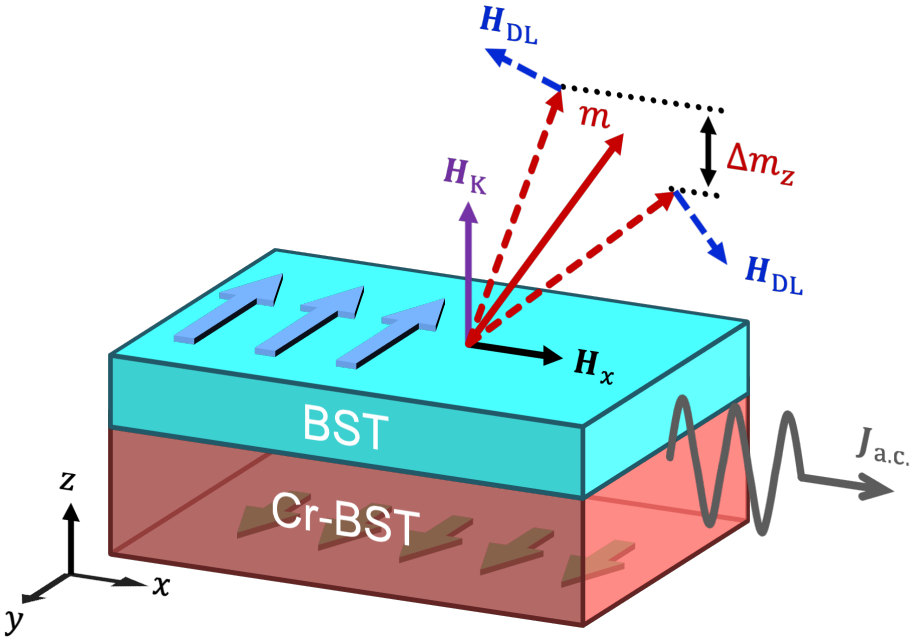

Figure 3-2. Schematic of the current-induced magnetization dynamics for optical probe of SOFs. When an IP current passes through the TI/Cr-doped TI bilayer structure, it produces a giant SOF owing to the spin-momentum locking in TI's surfaces and the different conditions on the top and bottom surfaces. This SOF can reorientate magnetic moments and drive magnetization dynamics. If the injected current is an a.c. current and a collinear IP field H_x is present, the DL-SOF will excite an OP magnetization oscillation (Δm_z), which contains quantitative information about the SOF and can be probed optically. The frequency of the a.c. current is ~673 Hz, which is much lower than the typical ferromagnetic resonance/precession frequency. The black arrow denotes the IP magnetic field H_x; The violet arrow denotes the effective field of the perpendicular

anisotropy (H_K); The solid (dashed) red arrows denote the magnetization orientation without (with) the IP current injection/the current-induced DL-SOF.

Figure 3-3a depicts the optically measured $\Delta\theta_K$ as a function of H_x at 12K for $J_{a.c.}$ = 4.3×10^4 A cm^{-2} by assuming a uniform current density throughout the bilayer. The dependence of $\Delta\theta_K$ on H_x is qualitatively consistent with the picture of SOF-induced macroscopic magnetization oscillations as evidenced by the following H_x-dependent features observed in Figure 3-3a: (1) $\Delta\theta_K$ = 0 at H_x = 0. As in the absence of an external magnetic field, the magnetic moments spontaneously orientate along the z-axis due to the perpendicular anisotropy and make the SOF-induced magnetization oscillation contain no OP component, i.e., $\boldsymbol{H}_{DL} \parallel (\boldsymbol{J}_C \times \boldsymbol{z}) \times \boldsymbol{m} \parallel x$-axis and Δm_z = 0; (2) Next, $\Delta\theta_K$ increases as H_x increases because the tilted magnetic moments now result in a finite z-component in the DL-SOF ($\boldsymbol{H}_{DL} \parallel (\boldsymbol{J}_C \times \boldsymbol{z}) \times \boldsymbol{m}$) as well as the SOF-induced magnetization oscillation. (3) Then, this non-zero z-component reaches its maximum at $H_x \approx H_K$ where the magnetization of the Cr-doped TI layer is fully aligned along the x-axis such that the SOF-driven magnetization oscillation is completely along the z-axis, i.e., $\boldsymbol{H}_{DL} \parallel (\boldsymbol{J}_C \times \boldsymbol{z}) \times \boldsymbol{m} \parallel z$-axis. Therefore, the effective perpendicular anisotropy field H_K can be approximately inferred from the peak position of $\Delta\theta_K$, as marked by the dashed lines in Figure 3-3a. As a result, it is estimated $H_K \approx \pm$100 mT for the TI/Cr-TI bilayer structure from Figure 3-3a; (4) When H_x further increases beyond H_K, the external field acts against the SOF-induced magnetization oscillation, and $\Delta\theta_K$ starts to decrease with a simple $1/|H_x - H_K|$ scaling as derived in Section 2.4 and Equation (2-7). In Equation (2-7), the parameter $f_\perp$ is indeed the saturation Kerr angle (i.e., $f_\perp = \theta_S$) extracted from the OP hysteresis loop (Figure 3-1a) and the H_K can be treated as a free parameter or takes the value inferred from the peak position of $\Delta\theta_K - H_x$ curve. Figure 3-3b presents the $\Delta\theta_K$ signals

collected from a reversed structure, i.e., five quintuple layers of Cr-doped $Bi_xSb_{2-x}Te_3$ on top and two quintuple layers of $Bi_xSb_{2-x}Te_3$ at the bottom, using the same measurements. Compared with Figure 3-3a, the results in Figure 3-3b manifest similar features but with opposite polarity. This polarity reversal of signals is consistent with the definition of SOF as the helicity of surface conduction is opposite for the top and bottom TSSs,(*59*) demonstrating again a good agreement with the picture of SOF-induced magnetization oscillation.

The optical signals at the high field regime (i.e., $H_x > H_K$) are of particular importance for quantifying the SOFs. In this regime, while the OP magnetization oscillation is mainly driven by the H_{DL} and is expected to dominate the $\Delta\theta_K$ signal via polar MOKE effect, an IP oscillation induced by $\boldsymbol{H}_{FL} \parallel \boldsymbol{z} \times \boldsymbol{J}_C \parallel y$-axis can potentially make a minor contribution to $\Delta\theta_K$ through quadratic MOKE. Based on Equation (2-7), this contribution from $\boldsymbol{H}_{FL}$ should depend on the polarization plane of the laser, and hence, it can be distinguished from the H_{DL}-induced contributions by analyzing the polarization dependence of $\Delta\theta_K$. To this end, polarization-dependent measurements were conducted with a fixed current density $J_{a.c.} = 4.3\times10^4$ A cm^{-2}. The polarization of the laser is designated by the angle φ between the polarization plane and the x-axis. The results at different polarization angle φ ranging from 0º to 90º are shown in Figure 3-3c. The experimental data were offset and normalized to the θ_S for clarity. As verified by these experimental results, $\Delta\theta_K$ demonstrates no significant dependence on the laser polarization, indicating the contribution from H_{FL} is negligible, and hence, $\Delta\theta_K$ is predominated by the H_{DL}-induced OP oscillation in this experimental configuration. This absence of the H_{FL}-induced term is expected as the IP reorientation contributes to the $\Delta\theta_K$ through a second order non-linear effect, which is usually much smaller compared to the linear effect.

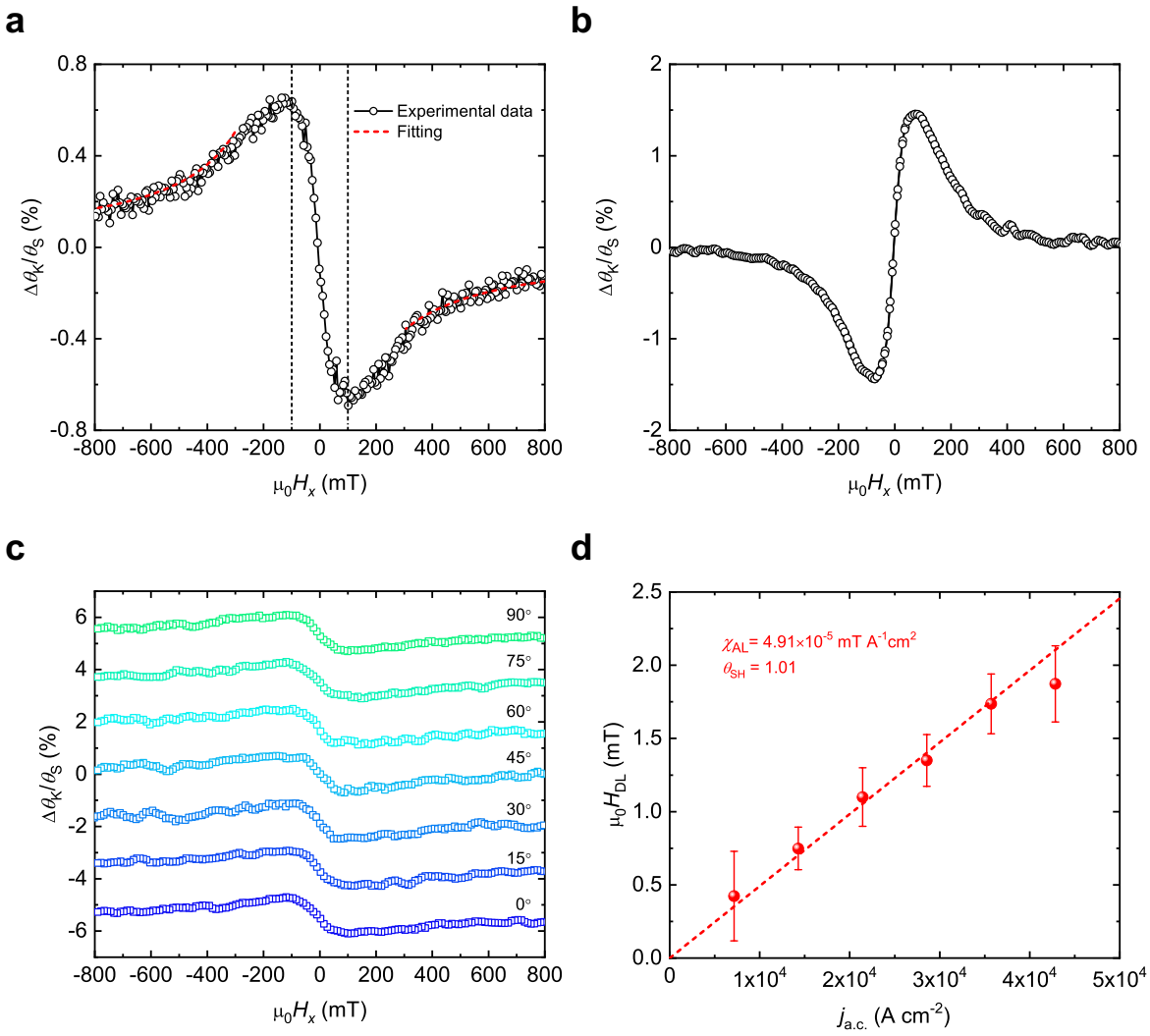

Figure 3-3. Measurements of current-induced magnetization dynamics and SOFs in TI/Cr-doped TI bilayer heterostructure. a. the current-induced changes in Kerr rotation ($\Delta\theta_K$) as a function applied field along x-axis for $J_{a.c.}$ = 4.3×10^4 A cm^{-2} at 12 K. The magnitude of SOF can be obtained by fitting the experimental data with Equation (2-7) and the effective anisotropy field can be estimated from the peak position of $\Delta\theta_K$ as indicated by the black dashed line. **b.** $\Delta\theta_K$ probe with an identical experimental setup to those in **a** in a reversed magnetically-doped TI bilayer that consists of five quintuple layers of Cr-doped $Bi_xSb_{2-x}Te_3$ on the top and two quintuple layers of $Bi_xSb_{2-x}Te_3$ at the bottom. **c.** The normalized $\Delta\theta_K$ as a function of H_x at different polarization

angles ranging from 0º to 90º. The signals reveal no significant polarization dependence, indicating the H_{DL}-induced OP magnetization oscillation predominates the $\Delta\theta_{\mathrm{K}}$ signals via the polar MOKE effect. **d.** The optical quantification of DL-SOF as a function of the a.c. current. A linear fitting to the H_{DL} yields $\chi_{\mathrm{DL}} = \mu_0 H_{\mathrm{DL}}/J_{\mathrm{a.c.}}$ of 4.91 × 10^{-5} mT A^{-1} cm^2, which will be used to evaluate the charge-spin conversion efficiency in the following section.

Based on the findings above, fitting the $\Delta\theta_{\mathrm{K}}$ signals at the high field to the first term in Equation (2-7) yields H_{DL} ~ 1.90 ± 0.02 mT for $J_{\mathrm{a.c.}}$ = 4.3×10^4 A cm^{-2}. The direction of H_{DL} points along either $+z$ or $-z$ depending on the sign of H_x. The perfect fitting of experimental data to the Equation (2-7) firmly proves that $\Delta\theta_{\mathrm{K}}$ is governed by SOF-induced macroscopic magnetization oscillation. The current dependence of H_{DL} is summarized in Figure 3-3d for current density ranging from 7.1×10^3 A cm^{-2} to 4.3×10^4 A cm^{-2}, and H_{DL} scales linearly with the a.c. current indicating the Ohmic heating is insignificant. The linear fitting to the results in Figure 3-3d yields a SOF efficiency $\chi_{\mathrm{DL}} = \mu_0 H_{\mathrm{DL}}/J_{\mathrm{a.c.}}$ of 4.91 × 10^{-5} mT A^{-1} cm^2, which is two orders larger compared to those reported in conventional heavy metals.

To further confirm the accuracy and reliability of these MOKE results, the current-induced hysteresis shift method is employed, as schematically illustrated in Figure 3-4a.(*60*) It has been widely reported that the hysteresis shift method, which is developed on the basis of the Néel-type domain walls (DWs) formed during the magnetization reversal process, is a viable technique in determining the SOFs in a variety of magnetic devices.(*60–62*) Fundamentally, the presence of either bulk or interfacial Dzyaloshinskii-Moriya interaction (DMI) in most magnetic heterostructures stabilizes Néel-type DWs within the transitional area between ‘up’ and ‘down’ magnetic domains or during the magnetization switching process.(*63*, *64*) More importantly, the

DMI lifts the chiral degeneracy and determines the spin textures inside the DWs as shown in the left of Figure 3-4a.(*60*, *65*) When the DL-SOFs generated by an IP d.c. current act on these Néel-type DWs in the absence of an IP magnetic field, the DWs on opposite sides of a magnetic domain are driven to move in the same direction, producing zero net influence on the expansion or shrinkage of domains. However, when an IP field collinear with the current injection is applied to counteract the DMI and aligns the spin textures of DWs, the current-induced DL-SOFs can now produce a net effect on the domain expansion, as shown in the right of Figure 3-4b. In other words, the IP current-induced DL-SOFs preferentially facilitate the expansion of one magnetic state while suppressing the other in this case. Accordingly, in the presence of an IP current injection and a colinear IP magnetic field, the OP hysteresis loop will shift toward either the $+H_z$ or the $-H_z$ direction, depending on the sign of DMI. By integrating the z-component of SOF exerted onto the non-uniform spin texture inside the Néel-type DWs, the H_{DL} can be quantitatively estimated as $(H_+ + H_-)/\pi$ where H_+ and H_- represents the experimentally observed shift in the OP hysteresis loop for a positive or a negative IP current injection, respectively. Since the Cr-doped TI/TI bilayer also possesses an appreciable DMI,(*66*) this hysteresis shift method can be used to determine the SOF in TIs as an alternative to the MOKE techniques. Obviously, this hysteresis shift method is entirely independent of the MOKE technique because the primary mechanism of this method outlined above is fundamentally different from the magnetization oscillations underlying the MOKE SOF magnetometer.

To experimentally determine H_{DL} based on this scenario, a large d.c. current is applied to the device for generating the SOFs, and a small a.c. current is superposed on top of it simultaneously to read out the magnetization via anomalous Hall effect. Typical experimental results are presented in Figure 3-4b. Apparently, the hysteresis loop shifts toward opposite directions for opposite d.c.

currents, which agrees with the picture mentioned above. To provide a direct comparison with the optical results, this measurement was also carried out at 12 K with the presence of an in-plane field H_x. Nevertheless, if H_x is insufficient to fully overcome the DMI like that on the right of Figure 3-4a, meaning the spin directions inside the DWs are not completely polarized to the same direction, then the measured value of $|H_{\mathrm{DL}}|$ may deviate from the actual value. Indeed, the measured $|H_{\mathrm{DL}}|$ by the hysteresis shift method will gradually approach to its intrinsic value as H_x increases and saturates once the DMI is entirely overcome. To further quantify the exact value of H_{DL}, hysteresis shift measurements were performed under different H_x. Figure 3-4c shows the H_x-dependence of $\chi_{\mathrm{DL}} = \mu_0 H_{\mathrm{DL}}/J_{\mathrm{d.c.}}$, from which it is evident that χ_{DL} gradually increases at small fields and saturates at $\mu_0 H_x > 200$ mT with a value of 4.27×10^{-5} mT A cm^2. This result is in excellent quantitative agreement with that obtained from the previous MOKE measurements, confirming the accuracy of the optical results.

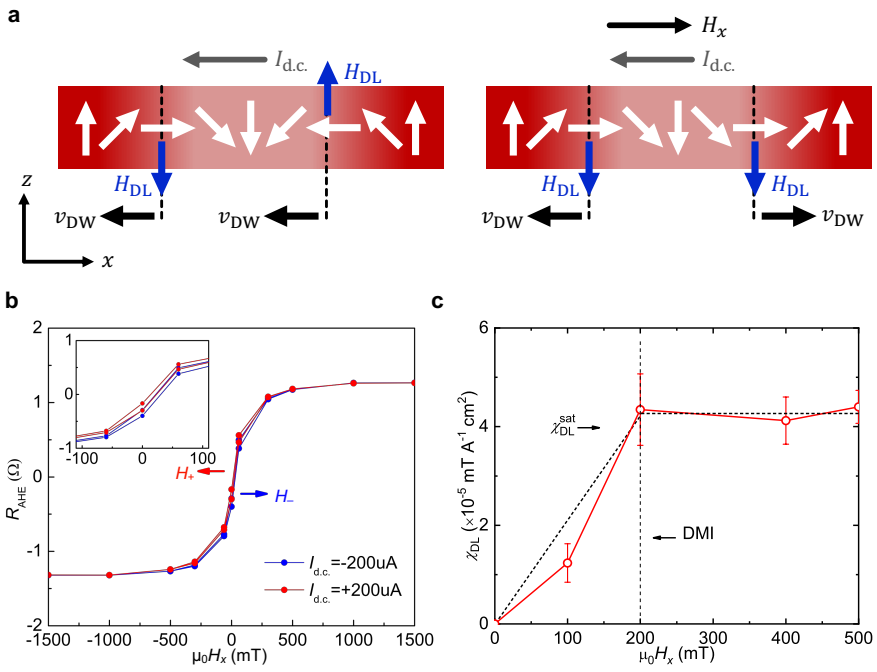

Figure 3-4. Current-induced hysteresis shift method for quantifying SOF. a. Schematic of the current-induced SOFs acting on Néel type domain walls of a magnetic system with perpendicular

magnetic anisotropy and Dzyaloshinskii-Moriya interaction. Only with the presence of an IP magnetic field, the domain walls will be pushed to move in opposite directions, leading to a net effect on magnetic domain expansion for magnetization switching. **b.** The typical current-induced shift of hysteresis loops with $I_{\mathrm{d.c.}} = \pm 200$ μA. **c.** The measured $\chi_{\mathrm{DL}} = \mu_0 H_{\mathrm{DL}}/J_{\mathrm{d.c.}}$ as a function of applied in-plane field along the x-axis. **a** is adapted from Ref.(*60*) with modifications.

In order to explicitly compare TI's performance with other conventional HMs and to better assess TI's potential for efficient spin current sources, the figure of merit for intrinsic charge-spin conversion efficiency, the (tangent of) θ_{SH}, is calculated from the experimental data using:(*18*)

$$\theta_{\mathrm{SH}} = (2e/\hbar)\,|\boldsymbol{J}_{\mathrm{S}}|/|\boldsymbol{J}_{\mathrm{C}}| = \frac{2eM_{\mathrm{S}}\mu_0 H_{\mathrm{DL}} t_{\mathrm{m}}}{\hbar|\boldsymbol{J}_{\mathrm{C}}|} \tag{3-1}$$

where e is the electron charge; $\hbar$ is the reduced Planck's constant; t_{m} is the thickness of the magnetic layer, which is the Cr-doped TI layer thickness in this case, and M_{S} is the saturation magnetization measured to be 13.5 emu cm^{-3} at 12 K from Figure 3-1b. The calculated $\tan(\theta_{\mathrm{SH}})$ is ~1.01 and its sign is the same as that of Pt, which are both consistent with previous reports on TIs(*31*, *36*, *54*, *62*, *67–76*). Additionally, the $\Delta\theta_{\mathrm{K}}$ signals presented in Figure 3-3b for the sample with a reversed stacking order yield comparable values of χ_{DL} and θ_{SH} with trivial differences, which do not affect the main conclusions and can be attributed to the minor variations in sample quality.

Another unresolved issue regarding the SOFs generated by TI is the huge disagreement among the previously reported temperature dependence of SOF strength in TIs.(*31*, *36*, *67*, *68*, *75*, *76*). Furthermore, a precise investigation into the temperature dependence of charge-spin conversion efficiency is critical to answering whether TI is feasible for practical spintronic devices at room temperature. To this end, temperature-dependent measurements on SOF in TI were carried out

with the same experimental setup, wherein both the external magnetic field and the laser polarization were parallel to the current injection at all temperatures. The current density was fixed at 4.3×10^4 A cm^{-2}. As shown in Figure 3-5a,b, the detected $\Delta\theta_K$ reduces rapidly as temperature increases while maintaining a characteristic $1/(|H_x| - H_K)$ dependence on H_x throughout the entire temperature range. Both θ_K and $\Delta\theta_K$ are below the detection threshold when the temperature is higher than 21 K. These experimental results, together with the extracted H_{DL} and θ_{SH} for temperatures ranging from 12 to 21 K, are illustrated in Figure 3-5c,d.

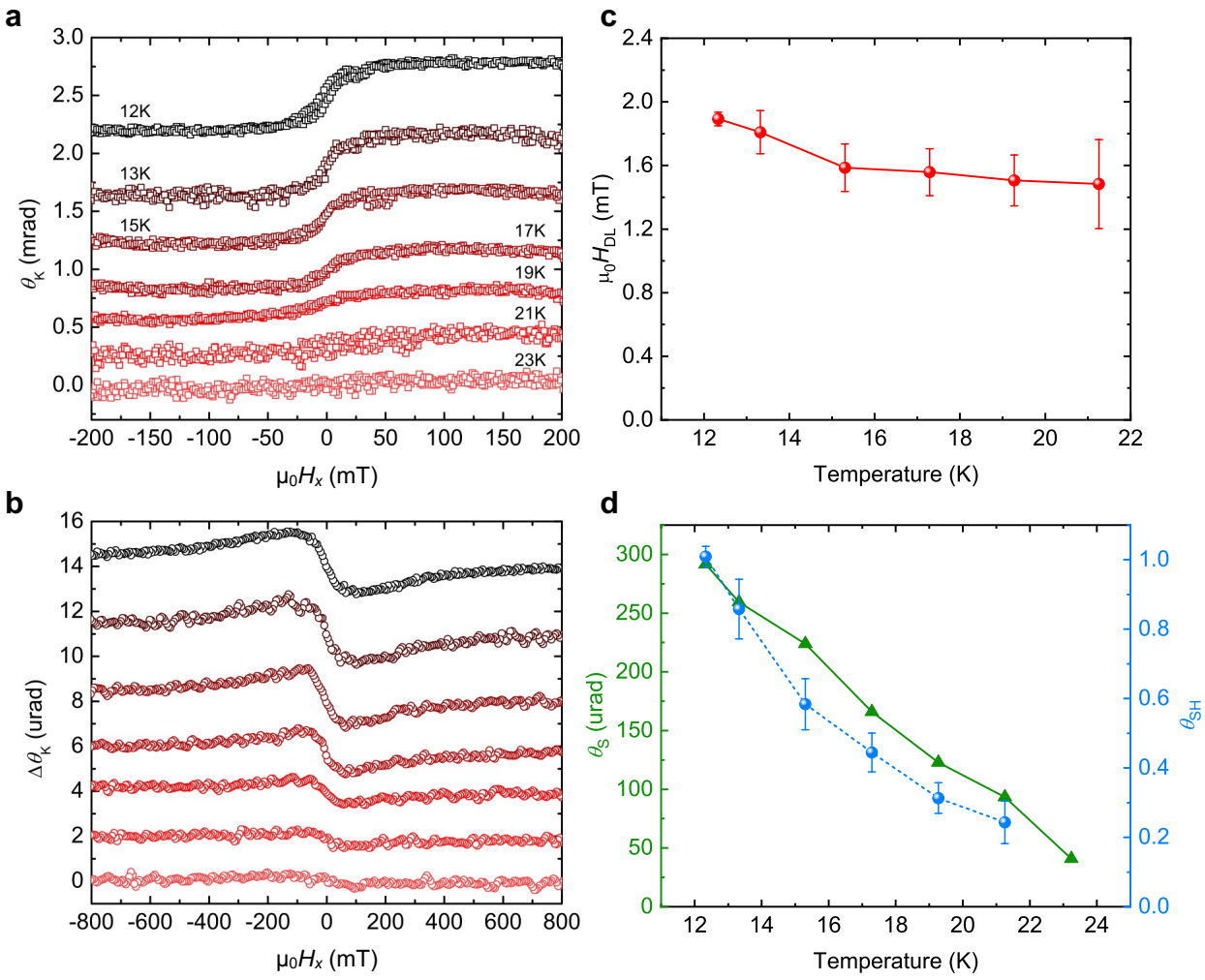

Figure 3-5. Temperature dependence of MOKE measurements of TI/Cr-doped TI bilayer heterostructure. **a**,**b** θ_K and $\Delta\theta_K$ as a function of the external field H_x at $J_{a.c.} = 4.3\times10^4$ A cm^{-2}

at different temperatures ranging from 12 K to near Curie temperature (~27 K). Note that the detected signals are significantly overwhelmed by noise at temperatures higher than 21 K. Throughout the entire temperature range of the MOKE measurements, the experimental data possess the features discussed in earlier sections and can be well-fitted to Equation (2-7), indicating the SOF origin of $\Delta\theta_{\mathrm{K}}$. **c.** Temperature dependence of the extracted H_{DL}. The amplitude of H_{DL} slightly decreases as temperature increases and remains sizeable up to 21 K when the ferromagnetism almost vanishes. **d**. Comparison between the temperature dependence of θ_{S} and the calculated θ_{SH}. The spin Hall angle θ_{SH} shows a similar temperature dependence as θ_{S}. Here, the θ_{S} can be treated as a proper representation of the M_{S} as concluded from Figure 3-1b.

Overall, both H_{DL} and θ_{SH} reduce as temperature increases, and this observation indicates the loss of spin polarization at a higher temperature,(*57*) which could be attributed to: (1) the thermally-activated bulk conduction, which leads to a relative reduction of contribution from spin-polarized surface conduction(*77*); (2) the enhancement of inelastic scatterings such as phonon scatterings which deteriorates the spin polarization of TSS when the temperature rises. Remarkably, when temperature increases, θ_{SH} appears to decay more sharply in comparison with H_{DL} and it drops to nearly zero when the temperature exceeds the Curie temperature of Cr-doped TI while the value of H_{DL} remains appreciable. As suggested by the similar temperature dependence of θ_{S} (or M_{S} as concluded from Figure 3-1b) and θ_{SH} shown in Figure 3-5d, the rapid disappearance of ferromagnetism in Cr-doped TI, which results in a reduction of spin coherent length and loss of channel for transfer angular momentum, could be the major reasons for the diminishing θ_{SH}. These findings suggest TIs can serve as an efficient spin source for spintronic applications at room

temperature if alternative magnetic materials with high Curie temperature and strong coupling to TI's TSSs can be found.

Indeed, recent work has demonstrated spin-orbit torque switching in a TI-ferromagnet heterostructure with perpendicular magnetic anisotropy at room temperature.(*62*) This recent success in using topological insulators with ferromagnets at room temperature has opened an innovative avenue in the field of SOT-based non-volatile magnetic memory and low dissipation electronics. Along this line, the next section will focus on developing feasible TI-based SOT devices that operate at room temperature.

3.3 Highly-Efficient Switching of Perpendicular Magnetization in Topological Insulator/Mo/CoFeB/MgO with High Thermal Tolerance at Room Temperature

As introduced in previous sections, the spin-orbit torque originating from materials with strong spin-orbit coupling has been progressively studied for its capability to efficiently manipulate the spin degree of freedom for potential low-dispassion high-speed memory devices. In the conventional heavy metal/FM heterostructure, the successful demonstration of SOT-based magnetization switching with an in-plane charge current injection(*18*, *19*, *78*) and subsequent development of applicable magnetic tunneling junctions(*17*) undoubtedly confirmed the predicted technological value of SOT-based memory devices. To further exploit the strength of SOFs beyond these conventional heavy metal/FM structures, recently discovered TIs,(*32*, *33*) wherein SOC is strong enough to change the band topology, have been experimentally demonstrated to generate giant SOTs for manipulating adjacent magnetic moments with unprecedented energy efficiency in several TI-based magnetic heterostructures.(*31*, *54*, *62*, *71*, *73*, *79*)

Regardless of the debatable origins of such giant SOTs, the development of prototypical TI/FM structures for either fundamental research or applicable devices remains a key technological challenge, namely, the integration of functional perpendicularly magnetized FM with TI for modern CMOS technology. Additionally, the widely used back-end-of-line processes in advanced CMOS technologies require heat treatments above 350 °C.(*30*, *80*) However, the desirable thermal tolerance for these processes has proved to be challenging and has not yet been demonstrated in TI/FM structures.

Based on the conclusions of Section 3.2 and inspired by the recent efforts of incorporating a layer of molybdenum (Mo) into heavy metal/FM structures to enhance the interfacial quality and thermal tolerance,(*81–84*) here, high-quality and technologically-preferred CoFeB/MgO layers were successfully grown on epitaxial TI by inserting a thin layer of Mo. The structures studied in this paper are TI(6)/Mo(2)/CoFeB(1)/MgO(2) stacks (as shown in Figure 3-6a) grown on a sapphire substrate (numbers in parenthesis are the layer thickness in nanometer). In this structure, six quintuple layers of $(Bi_{0.2}Sb_{0.8})_2Te_3$ TI thin film were first grown on the sapphire substrate using MBE. Immediately after the MBE growth, the TI films were transferred to the sputtering chamber through the air, and a stack of Mo/CoFeB/MgO with Ta capping was deposited consecutively using magnetron sputtering. To evaluate the thermal tolerance, five TI/Mo/CoFeB/MgO samples were then respectively annealed at different temperatures ranging from 200 °C to 400 °C for 30 minutes in a vacuum.

During the MBE growth of TI, reflection high-energy electron diffraction (RHEED) was performed to monitor the crystal quality, thickness, and surface flatness. As shown in Figure 3-6b, the high-quality growth of TI films with atomically flat surfaces is manifested by the sharp RHEED pattern, and the periodic RHEED oscillation explicitly indicates the layer-by-layer growth process.

A total thickness of 6 quintuple layers is determined by the number of peaks in the RHEED oscillations. X-ray diffraction (XRD) measurements were also conducted on the as-grown $(Bi_{0.2}Sb_{0.8})_2Te_3$ to identify its crystalline structure. As shown in Figure 3-6c, the growth direction along the *c*-axis is clearly indicated by multiple peaks collinear with the (001) direction, and good single crystal growth can be confirmed from the characteristic peaks.(*85*) With a well-tuned Bi/Sb ratio of 2:8 during the growth, the Fermi level of TI thin film is precisely controlled to lie within the bulk bandgap(*86*) as revealed by the electronic properties, namely, the carrier density, mobility, and the semiconductor-like temperature dependence of resistivity.

Figure 3-6d presents the sheet resistivity measured with a unitary length-width ratio as a function of temperature. The as-grown $(Bi_{0.2}Sb_{0.8})_2Te_3$ thin films are semiconducting, as revealed by the monotonically increasing sheet resistivity as the temperature drops from 300 K to 100 K. The carrier density and mobility were also evaluated by measuring the ordinary Hall resistance as a function of an OP field (as shown in Figure 3-6e). The (2-dimensional) carrier density ($n_{2D} = \mu_0 H_z / e R_H$) is 4.98×10^{12} cm^{-2}. Meanwhile, the mobility $\mu = 1/\rho_{sheet} n_{2D} e$ is calculated to be 186 cm^2 V^{-2} s^{-1}, where ρ_{sheet} = 6.74 kΩ is extracted from Figure 3-6d. The characteristic semiconducting behavior, carrier density, and carrier mobility together imply that the high-quality growth of TI is achieved, and the Fermi level of the as-grown TI thin film lies inside the bulk band gap. It was suggested that such conditions are beneficial for enhancing the charge-spin conversion efficiency in TIs.(*86*)

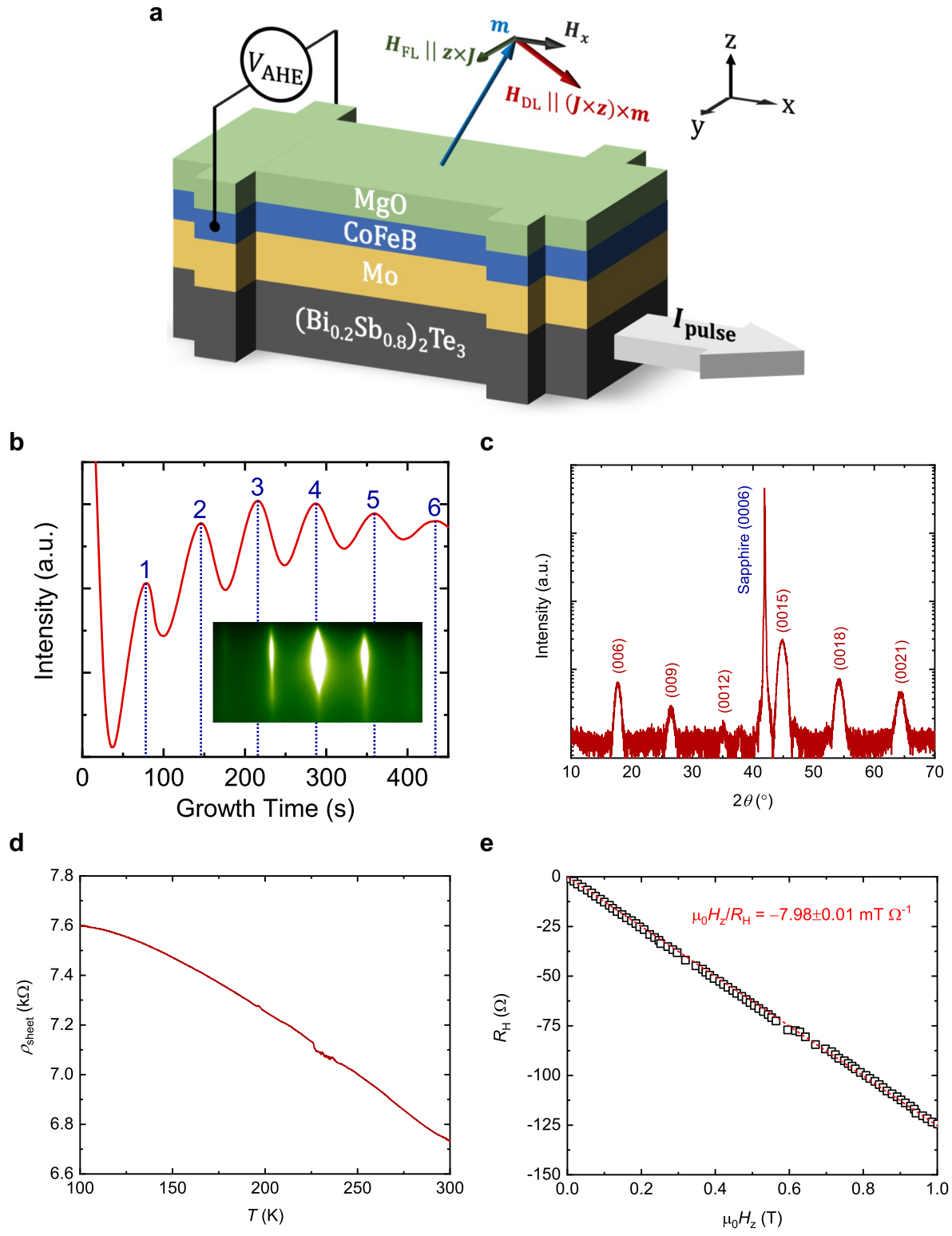

Figure 3-6. Experimental setup for transport measurements and material characterization of the $(Bi_{0.2}Sb_{0.8})_2Te_3$/Mo/CoFeB/MgO structures. a. Schematic of the sample and experimental

setup for measuring anomalous Hall resistance (R_{AHE}) to monitor the magnetization in samples and schematic of the current-induced magnetization switching by spin-orbit fields (SOFs) from TI, where H_{DL}, H_{FL}, H_x, and $\boldsymbol{m}$ represent the DL-SOF, FL-SOF, external magnetic field, and magnetization direction, respectively. The DL-SOF tilts and eventually switches the magnetic moment. **b.** The RHEED oscillation indicates the high-quality layer-by-layer growth of $(Bi_{0.2}Sb_{0.8})_2Te_3$, and the number of layers is indicated by the numbers in blue. **c.** XRD measurements of the as-grown $(Bi_{0.2}Sb_{0.8})_2Te_3$ film on a sapphire substrate. The growth direction along the *c*-axis is indicated by multiple peaks collinear with the (001) direction, and good single crystal growth can be confirmed from the characteristic peaks. **d.** Temperature dependence of sheet resistivity for a sample with a unitary length-width ratio. The temperature dependence is semiconductor-like, and the sheet resistance is 6.74 kΩ at room temperature. **e.** The ordinary Hall measurement for estimating carrier density and mobility. The semiconducting characteristics shown in Figure 3-6 indicate that the Fermi level lies inside the bulk band gap in the as-grown TI thin film, which is an optimal condition for enhancing the charge-spin conversion efficiency in TIs. Figure 3-6 is reproduced from Ref. (*55*) (Q. Pan's publication).

Regarding magnetic properties of TI/Mo/CoFeB/MgO film stacks, the interfaces (i.e., Mo/CoFeB and CoFeB/MgO) play an essential role in achieving robust perpendicular magnetic anisotropy.(*17*, *87–89*) The key ingredient here is the Mo insertion layer, of which the primary functionality is threefold:

1. Mo serves as a seed layer to grow the perpendicularly magnetized CoFeB/MgO on top of TI. It is known that the magnetic anisotropy of CoFeB largely depends on the interfacial conditions(*89*), and the atomic terraces on the surface of TI thin films preferably lead to an

easy-plane magnetic anisotropy in CoFeB/MgO if grown directly on TI without this Mo insertion layer.(*90*)

2. The Mo insertion can suppress the atom diffusion/intermixing across the TI/CoFeB interface at high temperatures, and hence, it tremendously enhances the thermal tolerance of the structures(*91*). Moreover, when the samples are annealed at a higher temperature, the crystallization of MgO and the quality of interfaces are thereby improved, resulting in a stronger PMA.
3. Mo has weak SOC(*92*) as well as a sufficiently long spin diffusion length and thus does not block the spin current generated by the TI. In terms of designing devices, such as magnetic tunnel junctions, the addition of the Mo layer offers an extra degree of freedom to lower the write energy by choosing a proper Mo thickness.(*90*)

To characterize the magnetic properties, SQUID measurements were performed on the annealed film stacks, and micron-size Hall bars for magneto-transport measurements were then fabricated by standard photolithography and dry etching techniques. Every magneto-transport result was verified by performing multiple device measurements, and high reproducibility was achieved. Figure 3-7a and 3-7b present the magnetization M and the anomalous Hall resistance R_{AHE} as functions of an external OP magnetic field for all annealed samples. While the as-deposited sample does not show desirable magnetic properties, the samples annealed at different temperatures all have an open, nearly rectangular OP hysteresis loop with a sizeable coercivity field $H_{\mathrm{C}} > 2$ mT. On the other hand, sharp magnetization reversal is not observed in the corresponding IP $M - H$ curves (Figure 3-7c). The IP $R_{\mathrm{AHE}} - H$ measurements were also carried out, and the results are presented in Figure 3-7d. Unlike the OP curves, the IP $M - H$ curves differ a lot from the corresponding $R_{\mathrm{AHE}} - H$ curves, which is due to the fact that the SQUID signals mainly reflect

the IP component of magnetization (i.e., M_x) while the R_{AHE} reflects the OP component of magnetization (i.e., M_z) in the experimental configuration. It should be noted that in the $R_{\mathrm{AHE}} - H$ curves, the sharp switching is likely caused by the applied field not being perfectly aligned within the film plane. Additionally, the R_{AHE} values at zero field are comparable to the saturation anomalous Hall resistance R_{S}, which means the spontaneous magnetization is fully aligned along the OP direction. These IP $M - H$ curves are useful for characterizing the key magnetic properties of the sample, as the effective perpendicular anisotropy fields H_{K} can be conveniently estimated as the IP saturation field, as shown in Figure 3-7c. Here, the IP saturation field (indicated by black arrows) is determined from the intersection of the extension lines of the saturation regions and a straight line with a slope fitted to the low-field region. The OP and IP hysteresis loops together undoubtedly confirm the presence of pronounced ferromagnetism with a clear OP easy axis at room temperature in all TI/Mo/CoFeB/MgO film stacks after annealing. To evaluate the thermal tolerance of the magnetic properties, the saturation magnetization M_{S} and the effective anisotropy field H_{K} as functions of the annealing temperature T_{A} are plotted in Figure 3-7e. The M_{S} is ~525 emu cm^{-3} (~660 mT) and exhibits no apparent dependence on T_{A}. These M_{S} values are lower compared to those (>1000 emu cm^{-3}) for CoFeB/MgO systems deposited on typical underlayers, indicating the potential existence of a magnetic dead layer in the structures.(*91*) At the same time, the smaller M_{S} results in weaker demagnetization energy, and hence, helps the PMA originated from the CoFeB/MgO interface dominate. Likewise, the saturation anomalous Hall resistance R_{S} obtained from Figure 3-7b is 2.4 Ω, 3.1 Ω, 2.6 Ω, 2.9 Ω, 3.0 Ω for T_{A} = 200 °C, 250 °C, 300 °C, 350 °C, 400 °C, respectively. The R_{S} demonstrates a good correlation with M_{S}, and we consider the magneto-transport results as proper reference to the magnetization state of the samples in the following sections.

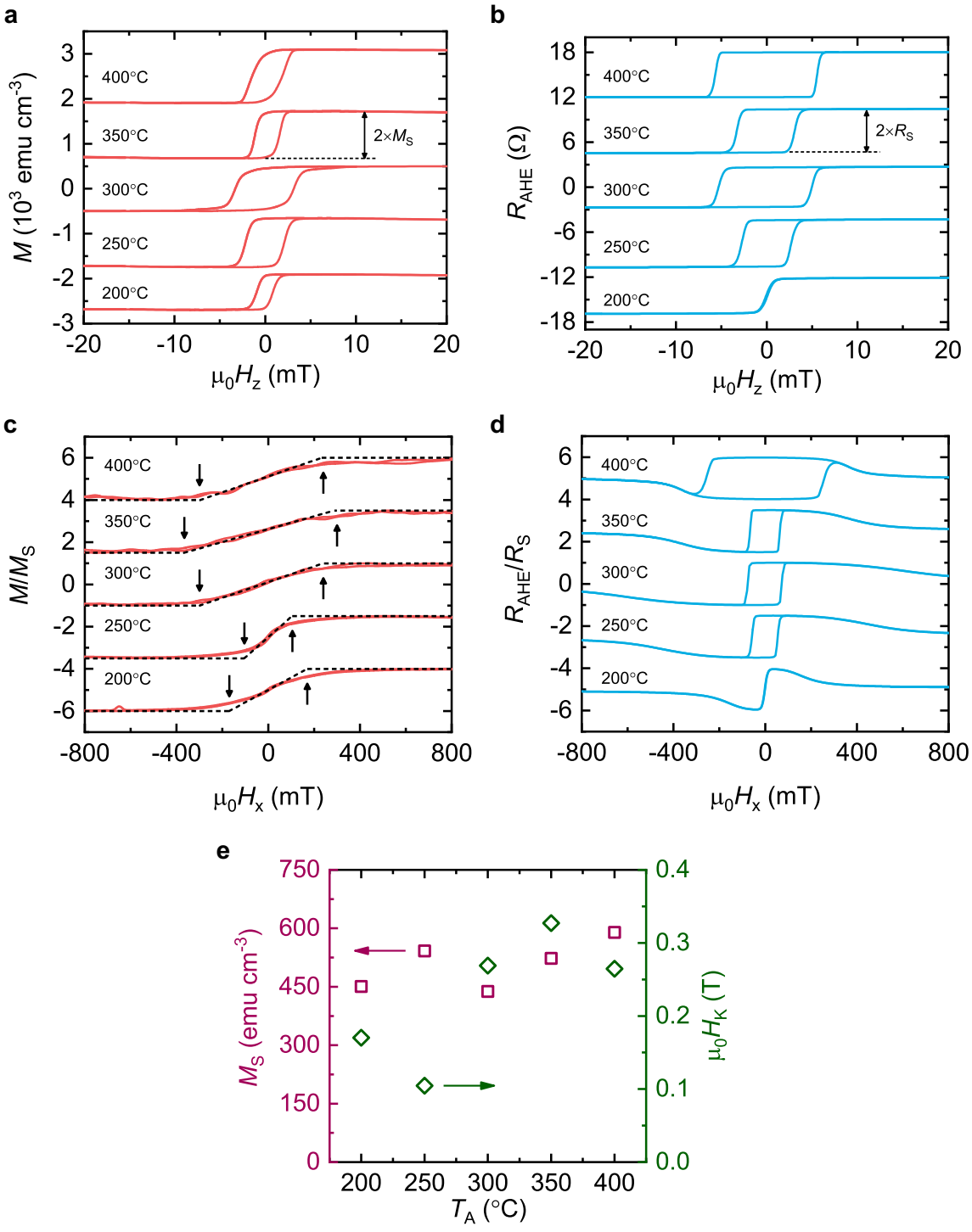

Figure 3-7. Magnetic properties of the $(Bi_{0.2}Sb_{0.8})_2Te_3$/Mo/CoFeB/MgO structures. a, b. The room temperature magnetization M and anomalous hall resistance R_{AHE} as functions of an external magnetic field along the z-axis (the OP direction) for the TI/Mo/CoFeB/MgO samples

annealed at different temperatures. The presence of pronounced ferromagnetism with a clear OP easy axis can be observed definitely. **c.** The room temperature magnetization (normalized to the saturation magnetization M_S extracted from **a**) as a function of an IP external magnetic field (H_x). The dashed black lines are the extension lines of the saturation regions and the straight lines with a slope fitted to the low-field region for estimating the IP saturation fields. The black arrows indicate the estimated effective anisotropy field H_K, which is 170 mT, 100 mT, 270 mT, 330 mT, 260 mT for T_A = 200 °C, 250 °C, 300 °C, 350 °C, 400 °C, respectively. **d.** The room temperature R_{AHE} (normalized to the saturation anomalous Hall resistance R_S extracted from **b**) as a function of H_x for the TI/Mo/CoFeB/MgO samples with different annealing temperatures. The $R_{AHE} - H$ curves differ from the corresponding $M - H$ curves because the SQUID signals mainly reflect the IP component of magnetization (i.e., M_x) while the R_{AHE} reflects the OP component of magnetization (i.e., M_z). **e.** the dependences of saturation magnetization M_S and effective anisotropy field H_K on the annealing temperature. No obvious deterioration of magnetic properties is observed at an increased annealing temperature up to 400 °C. Figure 3-7 is reproduced from Ref. (*55*) (Q. Pan's publication).

In contrast to M_S, an apparent improvement in H_K is observed at elevated annealing temperatures. As shown in Figure 3-7e, the H_K is smaller than 180 mT for T_A < 300 °C and increases rapidly to >270 mT for T_A ≥ 300 °C. Based on the measured M_S and H_K, the PMA can be quantified using the anisotropy energy density $K = M_S H_K/2$, which ranges from 2.8×10^4 J m^{-3} to 8.6×10^4 J m^{-3} with a trend of increasing with T_A (Figure 3-8a). It is worth noting that for samples annealed at between 300 °C to 400 °C , the PMA energy is sufficiently high to provide a thermal stability $\Delta = KV/k_B T > 45$ (where V is the volume of the 1 nm CoFeB layer, k_B is the Boltzmann constant, and

T = 298 K for room temperature) at a scaled device size of 60 nm in diameter, satisfying the typical requirements for applicable memory devices.(*93*) This enhancement of PMA at higher annealing temperatures has most likely resulted from the improved CoFeB/MgO interface quality. Here, the interfacial contribution to the PMA is quantified using the interfacial anisotropy K_{i}, which can be calculated from the relation:

$$K = \left(K_b - 2\pi {M_{\mathrm{S}}}^2\right) + \frac{K_{\mathrm{i}}}{t_{\mathrm{m}}} \tag{3-2}$$

where K_b is the bulk anisotropy which is negligible for the CoFeB/MgO system,(*17*, *94*) $-2\pi {M_{\mathrm{S}}}^2$ is the demagnetization energy, and t_{m} is the magnetic layer thickness, which is 1 nm in this case. Figure 3-8b presents the obtained K_{i} as a function of T_{A}. As T_{A} rises from 200 °C to 400 °C, the K_{i} gradually increases by 78% from 1.66×10^{-4} J m^{-2} to 2.96×10^{-4} J m^{-2} indicating the improvement of CoFeB/MgO interface quality.

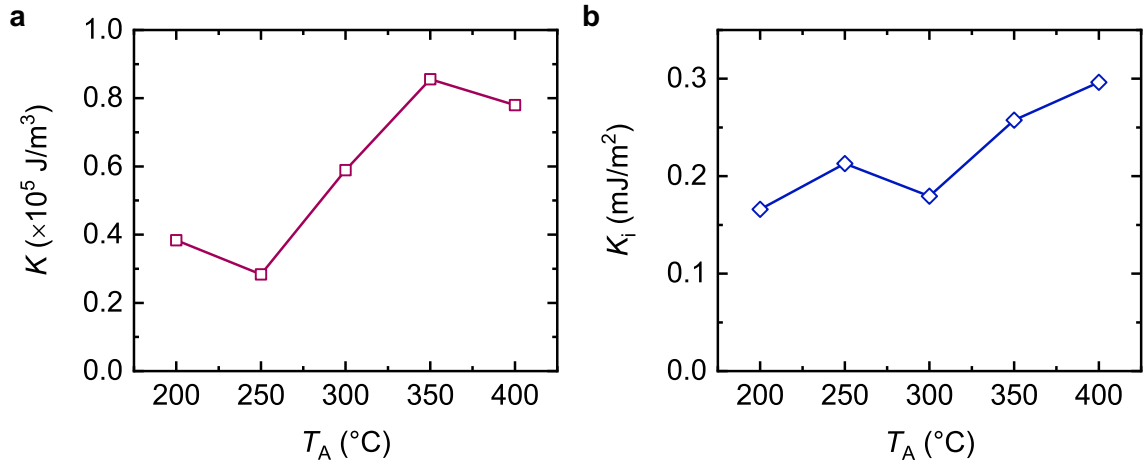

Figure 3-8. Anisotropy energy density and interfacial anisotropy in TI/Mo/CoFeB/MgO. The dependence of **a.** PMA energy density K and **b.** the interfacial anisotropy K_{i} on the annealing temperature T_{A}. The K_{i} is calculated from Equation (3-2) by assuming K_b = 0 for the CoFeB/MgO system.(*17*, *94*). Both the PMA energy density K and the interfacial anisotropy K_{i} gradually

increase with the annealing temperature, indicating an enhancement in the interfacial quality due to the annealing treatment. Figure 3-8 is reproduced from Ref. (*55*) (Q. Pan's publication).

To gain further insights into the high thermal tolerance and the annealing-enhanced PMA in the TI-based device with the Mo insertion, high-resolution transmission electron microscope (HR-TEM) measurements were carried out for the samples annealed at 200 °C and 400 °C. Figure 3-9a shows the TEM image for the 200 °C–annealed sample with the view axis along the $[10\bar{1}0]$ axis of the TI layer. While the lattice fringe of TI can be clearly identified, the Mo layer and CoFeB layer are not well distinguishable owing to a bad contrast between these two materials and their amorphous nature.(*91*) The MgO layer is not well crystallized, and the CoFeB/MgO interface is blurry. Figure 3-9b presents the TEM image for the 400 °C–annealed sample, and the view axis is changed to $[\bar{2}110]$ of the TI layer for better image contrast. Given the changes in the view axes, the lattice fringes of TI in Figure 3-9a and 3-9b are different. Two critical features, which do not depend on the view axis, can be clearly observed in Figure 3-9b. First, the crystal structure of the TI layer is well-preserved, and the interface between TI with the Mo layer is intact. As demonstrated in other studies, this is likely because the Mo insertion layer remains stable at 400 °C, which gives effective prevention of undesirable interdiffusion of neighboring elements and results in a high thermal tolerance.(*91*) Moreover, the thereby allowed annealing treatment up to 400 °C promotes crystallization in the samples and brings out the second observable feature in Figure 3-9b, that is, a better-crystallized MgO layer and a neat CoFeB/MgO interface at T_A = 400 °C. It has been theoretically(*95*) and experimentally(*94*, *96*, *97*) reported that the PMA of the CoFeB/MgO system originates entirely from the interfacial anisotropy. Accordingly, the PMA is more robust with a high-quality CoFeB/MgO interface. Consistent with these TEM observations,

the interfacial anisotropy of the TI/Mo/CoFeB/MgO film stack also exhibits a gradual increase with T_A as given in Figure 3-8b. Hence, the enhancement of PMA can be mainly attributed to the improved interfaces at a higher T_A within the range of this study.

Taken together, these results demonstrate that pronounced room temperature ferromagnetism with PMA is successfully integrated onto TI with the insertion of Mo. More remarkably, the key magnetic properties in the TI/Mo/CoFeB/MgO film stacks are well maintained within a wide annealing temperature window, offering high thermal tolerance for modern CMOS processes and device optimization, such as optimizing the T_A to realize high magnetoresistance in magnetic tunnel junctions.

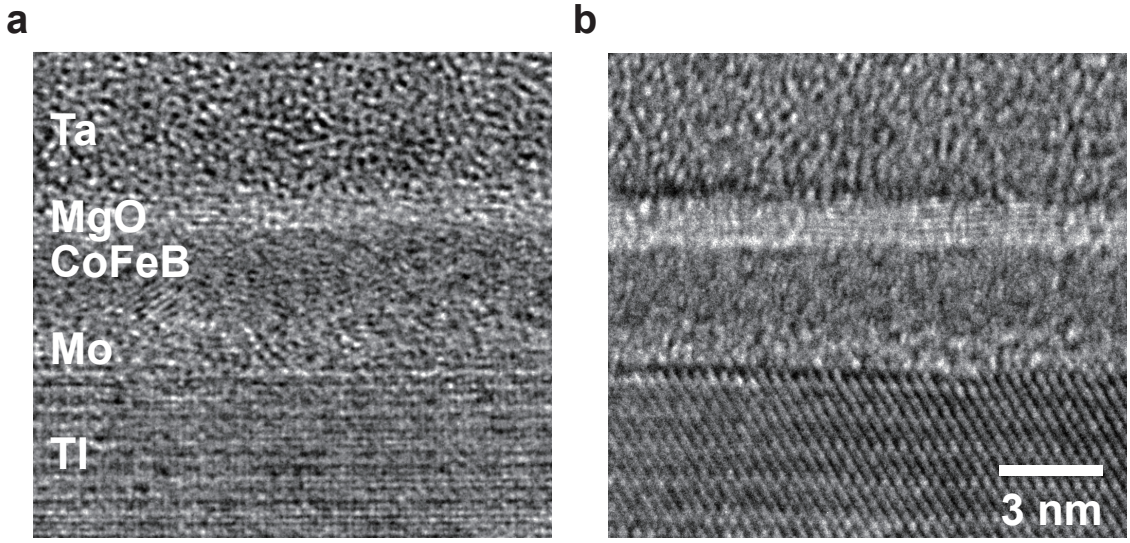

Figure 3-9. The cross-section HR-TEM image of TI/Mo/CoFeB/MgO stack. a. The TEM image for the 200 °C annealed sample with the view axis along $[10\bar{1}0]$ of the TI layer. **b.** The TEM image for the 400 °C annealed sample with the view axis along $[\bar{2}110]$ of the TI layer. Figure 3-9 is reproduced from Ref. (*55*) (Q. Pan's publication).

With the successful incorporation of the perpendicularly magnetized CoFeB/MgO system onto TI, the current control on magnetization in this TI-based structure can be examined. To demonstrate the current-induced magnetization switching, a sequence of magnitude-varying IP current pulses and a collinear external magnetic field H_x, are applied along the longitudinal direction of the Hall bar device (i.e., the x-axis). This configuration is employed based on such current-induced magnetization switching is caused by the DL-SOF generated by TI,(*25*) which is schematically depicted in Figure 3-6a and will be discussed in detail in the next section. The injected charge current pulses have a duration of 1 ms and can change the magnetization orientation, resembling the writing process in a SOT-based memory unit cell. Following each write current pulse, another pulse with a much smaller magnitude (~0.5 mA) was sent through the device to read the modified magnetization via the anomalous Hall effect. The sequence of write and read pulses is depicted in Figure 3-10a (bottom). Given the much smaller magnitude of the read pulse compared to the write pulse, it is reasonable to assume the read pulse does not significantly alter the magnetization. While no recognizable magnetization switching is observed for samples annealed at 200 °C, switching between two magnetic states by IP current pulses is realized for samples with T_A = 250 °C ~ 400 °C. A typical current-induced switching loop observed in these samples with a collinear external magnetic field of ±30 mT is shown in Figure 3-10a. One of the signatures of SOT-driven magnetization switching, the reversal of switching curve polarity when the IP field direction is changed, is observed and excludes the possibility of current-induced Oersted field or Joule heating being the main switching mechanism. In all these switchable samples, the difference between the initial and final anomalous Hall resistance (ΔR_{AHE}) in current-induced switching is comparable to the $2R_S$ extracted from OP hysteresis loops. Namely, the switching ratio defined as $\Delta R_{AHE}/2R_S$ is ~100% and hints a complete magnetization reversal by current injection is achieved in all samples

with T_A = 250 °C ~ 400 °C. Two reasons can account for the small discrepancy between the total R_{AHE} changes in current-driven and field-driven magnetization switching: 1) The current does not spread to the voltage pins of the Hall bar, and hence, the SOT-assisted expansion of reversed domains ceases and leads to some small unswitched area at the voltage pins; 2) The H_x applied in these measurements tilts the magnetic orders slightly off the OP direction, which reduces the R_{AHE}. To fully demonstrate the switching behaviors of samples, the current-induced switching experiments at different H_x were carried out and the critical switching current I_{SW} (defined as the magnitude of the current pulse at which R_{AHE} crosses zero during the switching) as a function of H_x is summarized in the phase diagram in Figure 3-10b. Under the conditions when both H_x and IP current pulse are large, i.e., at the four corner panels in Figure 3-10b, the magnetization state is deterministic; When H_x is small but non-zero, the deterministic switching behaviors between two distinct magnetization states are still preserved but with a smaller switching ratio. Whereas, if IP current injection is smaller than the I_{SW}, the up and down magnetization states are both possible as the hysteresis windows shown in Figure 3-10a. It is known that during SOT-induced magnetization switching, the H_x acts against the DMI and boosts the switching efficiency. Consequently, the I_{SW} drops as H_x increases and then saturates when the DMI is completely overcome by H_x.(*60*) The nearly constant I_{SW} at different H_x, as observed in Figure 3-10b, indicates the DMI in TI/Mo/CoFeB/MgO stack is relatively small and is overcome by a H_x ~ 2.5 mT. For samples with different T_A, the I_{SW} ranges from 3.7 mA to 5.8 mA, of which only ~7.5% passes through the TI layer estimated with a parallel resistance model. The converted critical current density (J_{SW}) inside the TI layer ranges from 2.5×10^5 A cm^{-2} to 3.6×10^5 A cm^{-2} (Figure 3-10c), which is significantly lower than those in heavy metals (on the order of 10^6 A cm^{-2} to 10^7 A cm^{-2}) and even some TIs in other reports,(*62*) highlighting the efficient electrical manipulation of

magnetization in the TI/Mo/CoFeB/MgO structures. Note that a recent study also demonstrated reversible current-induced magnetization switching in Mo-based magnetic heterostructures.(*92*) To rule out the possibility of Mo being the predominant cause of the current-driven magnetization switching, a control sample Mo(2)/CoFeB(1)/MgO(2)/Ta(2) was prepared with identical growth conditions except for the absence of the TI layer. This control sample acquires pronounced ferromagnetism with PMA, as shown in Figure 3-11a. The IP current injection experiments were carried out in the same manner as described above, and the magnetization states at different current magnitudes and external magnetic fields are summarized in Figure 3-11b and Figure 3-11c for positive and negative IP fields, respectively. No current-induced switching between the opposite magnetization states is observed with I_{pulse} up to 30 mA (the TI/Mo/CoFeB/MgO samples show current-induced magnetization reversal with $I_{\mathrm{pulse}} < 15$ mA) and further increasing the I_{pulse} beyond 30 mA damages the sample. It can be concluded from these results that the Mo layer cannot induce switching in this study. Therefore, the efficient current-induced switching in these samples is predominately attributed and correlated to the TI layer.

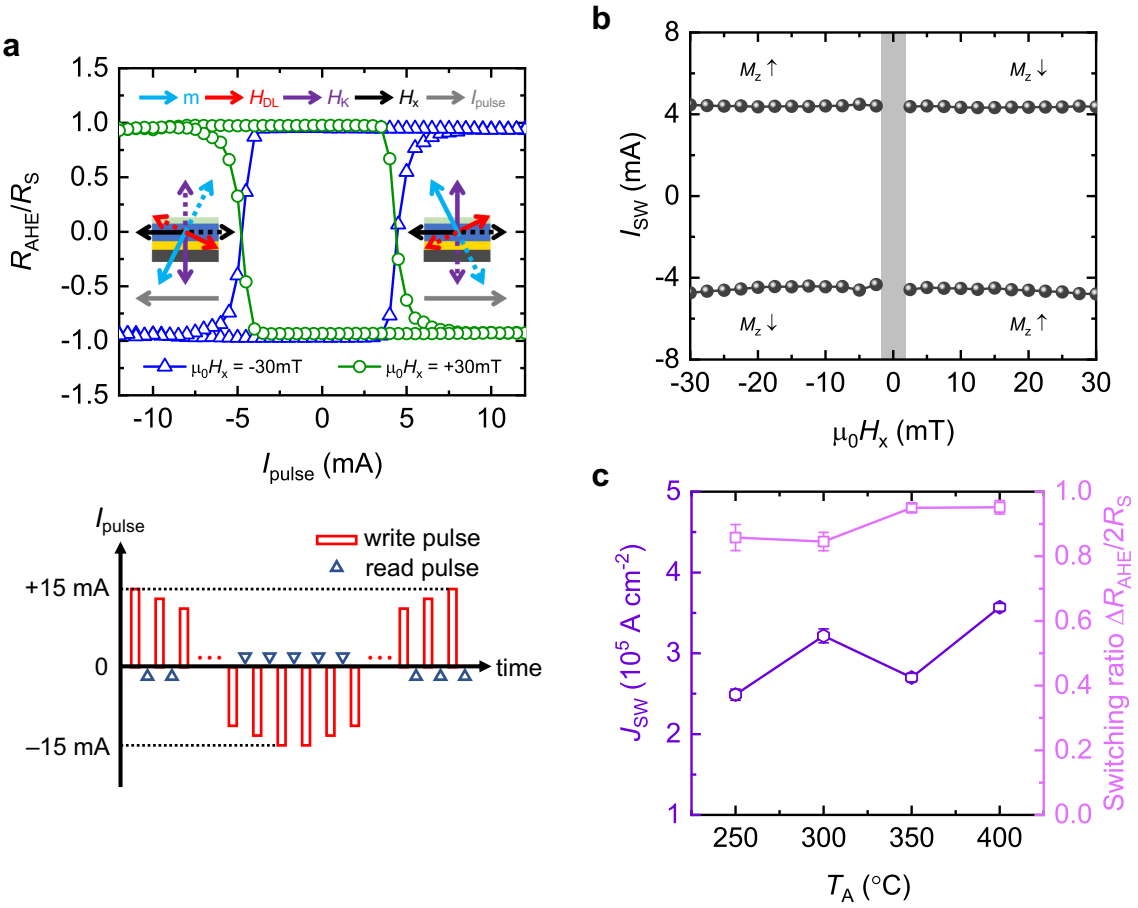

Figure 3-10. Current-induced magnetization switching via SOTs produced by TI. a. The current-induced switching assisted by an external magnetic field $\mu_0 H_x$ = ±30 mT at room temperature for samples with annealing temperatures of 350 °C. The insets depict how the final states are determined by the combined action of current-induced SOFs and H_x for the switching process. The solid (dashed) arrows denote the scenario for $\mu_0 H_x$ = –30 mT ($\mu_0 H_x$ = +30 mT). The R_{AHE} is normalized to the saturation anomalous Hall resistance (R_S) for a better demonstration of the complete magnetization switching from $+R_S$ to $-R_S$. The bottom inset shows the sequence of current pulses applied for demonstrating current-induced magnetization switching in TI/Mo/CoFeB/MgO. The maximal pulse applied in the experiments is ~15 mA. **b.** A typical phase diagram of the magnetization states depicting the critical switching currents as a function of H_x.

The critical switching current I_{SW} is defined as the magnitude of the current pulse at which R_{AHE} crosses the boundaries (R_{AHE} = 0) between the different magnetization states. $M_z\uparrow$ ($\downarrow$) indicates the magnetization orientation of the stable state is "up" ("down"), i.e., $R_{AHE} > 0$ ($R_{AHE} < 0$), after switching. The gray region indicates no current-induced switching is observed for $|\mu_0 H_x| < 2.5$ mT. **c.** J_{SW} and the switching ratio $\Delta R_{AHE}/2R_S$ as functions of T_A. Based on these results, complete magnetization switching can be achieved with a current density of ~10^5 A cm^{-2} for all presented samples. Figure 3-10 is reproduced from Ref. (*55*) (Q. Pan's publication).

A comparison in both the J_{SW} and the switching ratio $\Delta R_{AHE}/2R_S$ for samples with different T_A (Figure 3-10c) reveals that the magnetization switching behaviors are almost independent on T_A. Overall, the results in this section suggest that highly efficient electrical controllability of magnetization is realized in the TI/Mo/CoFeB/MgO structures and can be well sustained at T_A between 250 °C to 400 °C. The outstanding energy efficiency, along with the enhanced thermal tolerance, makes the TI/Mo/CoFeB/MgO structure a promising building block for modern spintronics devices.

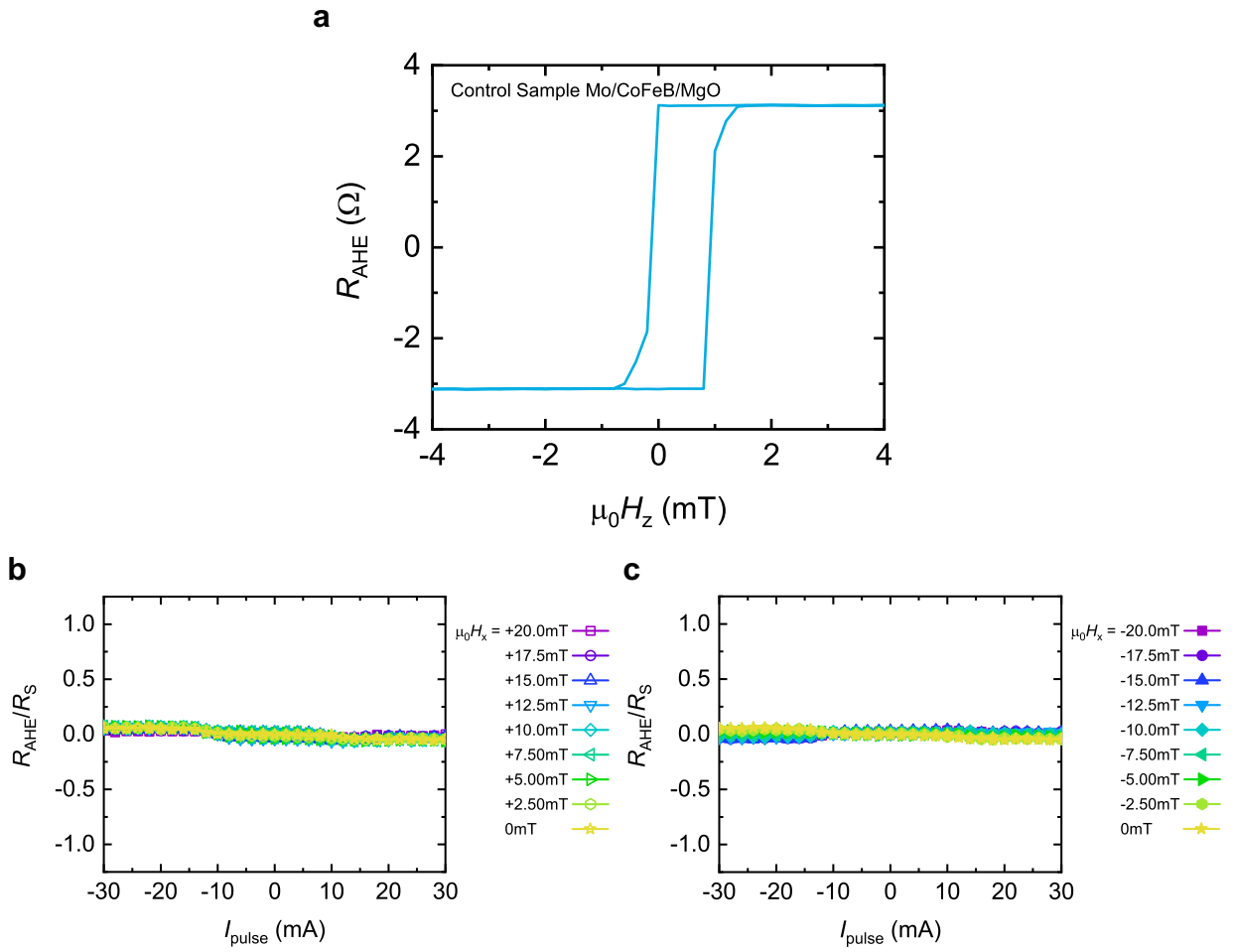

Figure 3-11. Control experiments on Mo(2)/CoFeB(1)/MgO(2)/Ta(2). a. Hysteresis loop (monitored using R_{AHE}) of a Mo/CoFeB/MgO/Ta control sample. A robust ferromagnetic order with perpendicular anisotropy can be clearly observed. (**b** and **c**) The normalized R_{AHE} of Mo/CoFeB/MgO sample in responses to the IP current pulse injection at different H_x. No detectable magnetization switching is observed. These results exclude the possibility of Mo being the major reason for the current-driven magnetization reversal. Figure 3-11 is reproduced from Ref. (*55*) (Q. Pan's publication).

The efficient magnetization manipulation achieved in these TI/Mo/CoFeB/MgO structures is ascribed to the current-induced SOFs from TI. In TI, the prominent spin-orbit coupling modifies

its band topology and results in the spin-momentum locking nature of its surface states.(*32*, *33*) One manifestation of this nature is that the conducting electrons on the surfaces of TI become completely spin-polarized and provide the dominant spin accumulation in the direction transverse to the electron motion, as shown in Figure 3-2.(*36*, *72*) Given that Mo has a spin diffusion length(*98*, *99*) that is considerably longer than its thickness (~2 nm) in the samples, the accumulated spin can diffuse over the Mo layer without loss and transfer angular momentum into the ferromagnetic CoFeB layer to reorient its magnetization. This current-induced effect can be viewed as applying SOFs onto the CoFeB free layer. More specifically, the damping-like SOF $\boldsymbol{H}_{\mathrm{DL}}$ is of primary interest for applicative magnetization switching in this thesis and is described by $\boldsymbol{H}_{\mathrm{DL}} \approx \chi_{\mathrm{DL}}(\boldsymbol{J}_{\mathrm{C}} \times \boldsymbol{z}) \times \boldsymbol{m}$.(*25*) When an external magnetic field and a current pulse are applied collinearly along x–axis, the combined action of H_{DL} and H_x selects a particular magnetization orientation in the CoFeB layer to be the final stable state (as illustrated in the insets of Figure 3-10a) for the switching process.(*54*, *65*, *100*, *101*) In the four cases shown in Figure 3-10a, the two where the current and the external field are applied in parallel result in a "down" magnetization state ($R_{\mathrm{AHE}} < 0$) after the switching process. Likewise, an "up" magnetization state ($R_{\mathrm{AHE}} > 0$) is preferred when the current and the external field are applied antiparallelly. These observations indicate the H_{DL} produced by the top surface of TI has the same sign as that of Pt.(*19*, *102*) In short, when assisted by a collinear external magnetic field, the IP current pulses through the TI layer can deterministically switch the magnetization state of the CoFeB layer via the SOF. To quantify the strength of such a SOF originating from the TSSs, well-established second-harmonic measurements were performed. In the presence of SOF induced by a moderate a.c charge current $J_0 \sin \omega t$ going through TI, the magnetic moment will oscillate around its rest position (i.e., when $J_0 = 0$), and manifest as a second-harmonic anomalous Hall resistance $R_{\mathrm{AHE}}^{2\omega}$ which can be

measured using lock-in techniques.(*25*, *54*, *86*, *103*, *104*) Note that the essence of this second-harmonic measurement is also the magnetization oscillation excited by an a.c. current and an external field along the x-axis, which is inherently the same as those discussed in Section 2.4 and Section 3.2. The principal difference is whether the magnetic moments are probed optically or electrically. Following the same formulation in Section 2.4 and Section 3.2, with a sufficiently large H_x (i.e., $H_x > H_{\mathrm{K}}$) to polarize the magnetic moments uniformly along the x-axis as a single domain state, $R_{\mathrm{AHE}}^{2\omega}$ acquires a simple form(*51*, *54*)

$$R_{\mathrm{AHE}}^{2\omega} = -\frac{1}{2}\frac{R_{\mathrm{S}}H_{\mathrm{DL}}}{|H_x| - H_{\mathrm{K}}} \tag{3-3}$$

where R_{S} is the saturation anomalous Hall resistance and H_{K} is the effective anisotropy field. Figure 3-12a and 3-12b depict the typical $R_{\mathrm{AHE}} - H_x$ curves and high-field $R_{\mathrm{AHE}}^{2\omega}$ signals produced by an a.c. current of $J_0 = 9\times10^4$ A cm^{-2} and the frequency of ~173 Hz through the TI layer. Curves are normalized to R_{S}, enlarged, and offset for clarity. In all studied samples, the spontaneous Hall resistance at zero field during the IP-field scans virtually reaches R_{S}, which strongly suggests a large exchange interaction is capable of spontaneously aligning all magnetic moments and retains samples in a single domain state during the measurements, validating the assumption for second-harmonic method. In the high-field region (i.e., $H_x > H_{\mathrm{K}}$), the nearly zero R_{AHE} (i.e., $|R_{\mathrm{AHE}}/R_{\mathrm{S}}|$ < 10% where R_{S} is obtained from Figure 3-7d) implies the magnetic moments of the CoFeB layer are fully aligned with the sufficiently strong H_x and the $R_{\mathrm{AHE}}^{2\omega}$ signal monotonically scales down with a $1/(|H_x| - H_{\mathrm{K}})$ field dependence indicating the SOF origin of $R_{\mathrm{AHE}}^{2\omega}$ as predicted. Additionally, the antisymmetric profile of $R_{\mathrm{AHE}}^{2\omega}$ as a function of H_x is also consistent with the picture of SOF-induced macroscopic magnetization oscillation. Fitting the experimental results of $R_{\mathrm{AHE}}^{2\omega}$ to Equation (3-3) at the high field region (shown by the black dashed lines in Figure 3-

12b) yields the H_{DL} strength and the H_{DL} extracted from the positive and negative fields have the same value but opposite signs. The perfect fitting of experimental data to the Equation (3-3) signifies that the $R_{AHE}^{2\omega}$ stems from the SOF-induced macroscopic magnetization oscillation. Moreover, the high linearity observed in the current dependency of H_{DL}, as summarized in Figure 3-12c, allows safely assuming that the contributions due to Joule heating and deviation of the dynamics from the linear regime are not prominent in the transport measurements.

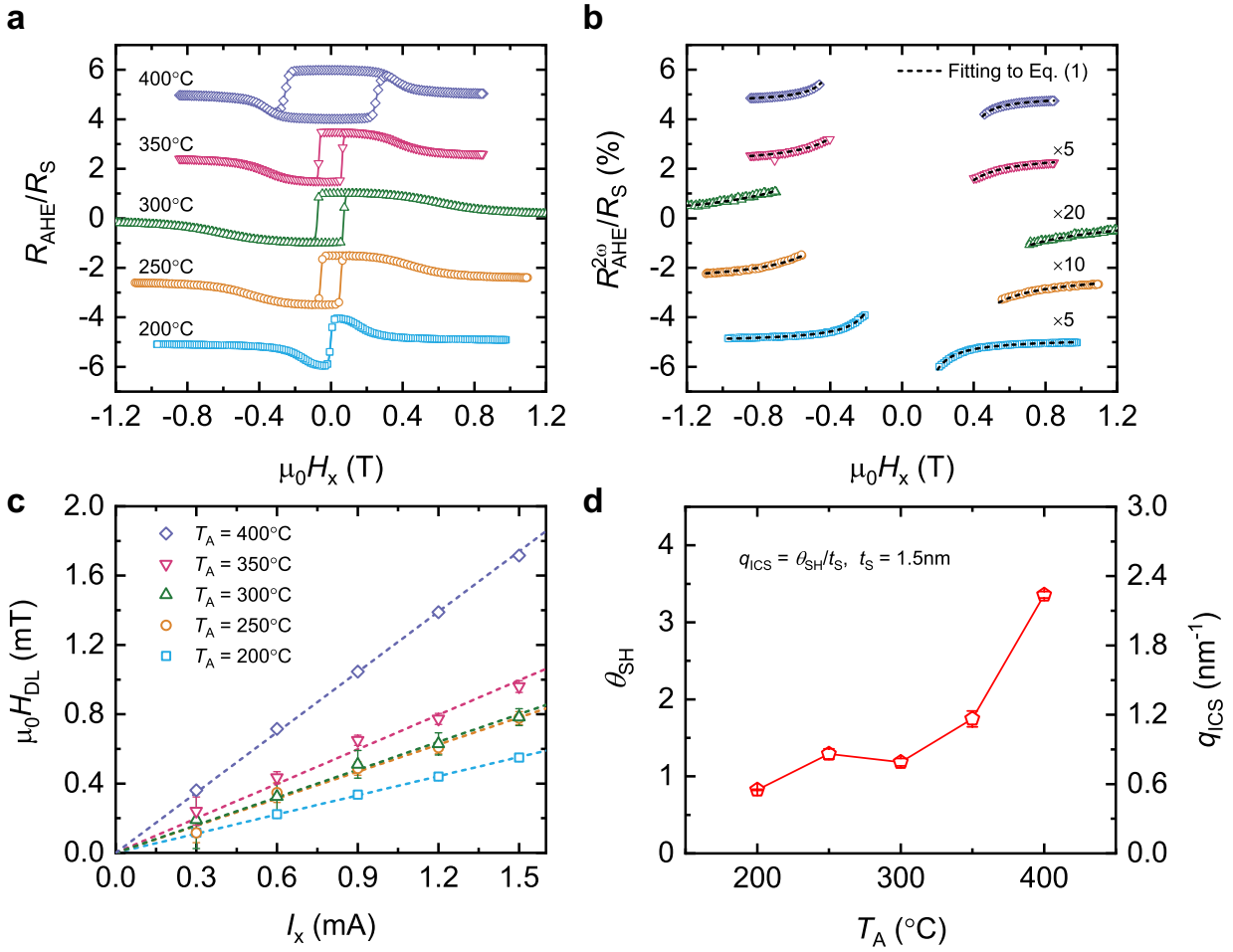

Figure 3-12. Calibration of charge-spin conversion efficiency in TI. a. and **b.** IP field dependence of anomalous Hall resistance (R_{AHE}) and second-harmonic anomalous Hall resistance ($R_{AHE}^{2\omega}$) induced by an a.c. current ($J_0 \sim 9\times10^4$ A cm^{-2} inside TI layer and $\omega \sim 173$ Hz). The switching observed in the IP hysteresis loops is due to the imperfect alignment of the applied fields,

which results in a small OP component. Fitting of experimental results to Equation (3-3) at high external field region (i.e., $H_x > H_K$ where H_K is given in Figure 3-7e) to extract the value of H_{DL} is presented with black dashed curves. Note that the experimental results are normalized to R_S, enlarged, and offset for clarity. **c.** current dependence of H_{DL} for samples with different annealing temperatures. The presented linearity indicates a negligible contribution from nonlinear effects and yields the charge-spin conversion efficiency parameterized by θ_{SH} (or q_{ICS}). **d.** Summary of dependence of θ_{SH} (and q_{ICS}) on the annealing temperature. A significantly enhanced θ_{SH} of ~3.36 (equals to q_{ICS} ~2.24 nm^{-1}) is achieved with annealing temperature T_A = 400 °C. This enhancement is ascribed to the annealing-promoted interfacial quality. Data and results presented in Figure 3-12 were also confirmed using the MOKE detection technique described in Section 2.4. Figure 3-12 is reproduced from Ref. (*55*) (Q. Pan's publication).

These results on H_{DL} are further compared with those obtained using the MOKE techniques developed in Section 2.4(*51*) and quantitively consistent results are obtained. In short, possible nonlinear effects (e.g., Joule heating, anomalous Nernst effect, and spin Seebeck effect $\propto {J_0}^2$), which are likely involved in the second-harmonic analysis of Hall voltage, do not add to the magneto-optical signal since it is a linear response to the current density (i.e., $\propto J_0$). Accordingly, the consistency between the transport and optical results firmly excludes the possible involvement of these nonlinear effects in the experimental results.

To quantify the intrinsic charge-spin conversion efficiency of TI, the effective spin Hall angle (tangent) θ_{SH} is calculated from the experimental results using Equation (3-1).(*18*) In this case, t_m is the thickness of the CoFeB layer. It should be noted that θ_{SH} is used here as an empirical term to quantify the overall efficiency of a spin current source without identifying the governing

mechanisms of the spin current generation. To reasonably emphasize the semi-2D TSSs as the primary spin generator, especially in this case of TIs with bulk insulating conditions, we estimated the interfacial charge-spin conversion efficiency(*72*) $q_{\mathrm{ICS}} = J_{\mathrm{S}}/J_{\mathrm{C}}^{\mathrm{2D}} = \theta_{\mathrm{SH}}/t_{\mathrm{S}}$, where $J_{\mathrm{C}}^{\mathrm{2D}}$ is the surface charge current density and t_{S} denotes the effective thickness of the SOC layer. With the assumption of a completely insulating bulk in the TIs, t_{S} is the TSS thickness and is estimated to be 1.5 nm from the half-thickness of TI, below which the top TSS hybridizes with the bottom TSS.(*105*) Although a completely insulating bulk would oversimplify the situation, a slightly conductive bulk should only produce negligible effects on the presented results.(*72*) Likewise, t_{S} can take the spin-diffusion length or SOC layer thickness (whichever is smaller) for calculating q_{ICS} in the 3D heavy metals. Extracting the H_{DL}/J_0 ratios from Figure 3-12c (shown by dashed lines) yields θ_{SH} and q_{ICS} for different annealing temperatures, as presented in Figure 3-12d. In stark contrast to the previously reported adverse effects of T_{A} on the performance of heavy metals,(*106*) the θ_{SH} of the presented TI-based structures constantly possesses a high value within the temperature range of this study. Quantitatively, θ_{SH} > 100% is achieved in samples with T_{A} from 250 °C to 400 °C and an appreciable enhancement in the θ_{SH} is observed when T_{A} rises above 350 °C. At 350 °C and 400 °C, which are the heat treatment temperatures usually required in the modern CMOS industries, θ_{SH} reaches a value of ~1.75 (q_{ICS} ~1.16 nm^{-1}) and ~3.36 (q_{ICS} ~2.24 nm^{-1}), respectively, which are 2~4 times of that at 200 °C providing an additional explanation for why no switching is achieved at 200 °C. The larger θ_{SH} at 350 °C and 400 °C are likely due to the annealing-enhanced interface quality and material properties. The experimentally determined θ_{SH} evaluates the overall charge-spin conversion in the TI/Mo/CoFeB/MgO film stack, and hence, depends not only on the intrinsic properties of each layer but also on the interfacial quality/spin transparency.(*25*, *89*, *107*) While in general, annealing treatments rearrange atoms and promote

crystallization to improve the quality of materials and interfaces, these benefits are counteracted as earlier studies have shown that annealing also lead to atom intermixing/diffusion at the interfaces, and thereby sever deterioration of the charge-spin conversion.(*106*) Therefore, with the Mo insert layer serving as a thermal barrier to prevent the atom intermixing/diffusion, the annealing treatment now considerably improves the interface quality/transparency and material properties in the TI/Mo/CoFeB/MgO stacks. This improvement in the quality of interfaces and materials upon annealing is evidenced as (1) the sharper interfaces at TI/Mo, Mo/CoFeB, and CoFeB/MgO observed in the TEM images (Figure 3-9b); (2) the annealing-enhanced magnetic anisotropy (Figure 3-7e) and interfacial anisotropy energy (Figure 3-8b). It is noteworthy that the contribution from shunting current in the Mo insertion should just lead to minor overestimation here, given its small θ_{SH} (*98*, *99*). In contrast, other factors such as the spin mixing conductance(*107*, *108*) and the spin memory loss(*109*, *110*) at the interfaces can potentially cause underestimation of θ_{SH}. Nevertheless, the θ_{SH} >100% in these TI/Mo/CoFeB/MgO structures is at least one order of magnitude larger than those previously found for similar thin stacks where TI is replaced with heavy metals as the SOC layer(*84*) (e.g., Ta/Mo/CoFeB/MgO and Pt/Mo/CoFeB/MgO) as summarized in Table 3-1.

Table 3-1. Room temperature ρ, $|\theta_{SH}|$, t_S, $|q_{ICS}|$, P in TIs and heavy metals.

	ρ [Ω·m]	$\lvert\theta_{SH}\rvert$ [dimensionless]	t_S [nm]	$\lvert q_{ICS}\rvert$ [nm^{-1}]	$P \propto \rho/{\theta_{SH}}^{2}$ [b)]
$(Bi_{0.2}Sb_{0.8})_2Te_3$ (this work)	4.0×10^{-5}	3.36	1.5[a)]	2.24	0.013
$Bi_xSe_{(1-x)}$(*71*)	1.3×10^{-4}	1.35	1.5[a)]	0.90	0.250
$Bi_xTe_{(1-x)}$(*111*)	5.2×10^{-6}	0.82	1.5[a)]	0.55	0.027
Bi_2Se_3(*112*)	1.1×10^{-2}	75.1	1.5[a)]	50.07	0.007
Bi_2Se_3(*113*)	8.9×10^{-6}	0.35	1.5[a)]	0.23	0.260
$Bi_{0.85}Sb_{0.15}$(*114*)	3.7×10^{-5}	3.2	1.5[a)]	2.13	0.235
$Bi_{0.9}Sb_{0.1}$(*115*)	4.0×10^{-6}	52	1.5[a)]	34.67	1.48×10^{-4}
Ta(*84*)	1.6×10^{-6}	0.40	1.9	0.21	0.036
Pt(*84*)	4.5×10^{-7}	0.04	7.3	0.01	1.000

[a)]These t_S are estimated from Ref. (*105*);

[b)]For normalization, the switching energy uses the Pt/Mo case as a reference, which is ~2.8×10^{-4} Ω m

Table 3-1 also includes the θ_{SH} for other recent reports of TI-based SOT switching devices that are particularly appealing to industrial applications. The room temperature of perpendicularly magnetized FM by TIs was first reported in Ref. (*62*) and was later achieved with TIs grown by a CMOS-industry compatible sputtering process.(*71*, *111–114*) Other researchers also focused on TIs with a higher bulk electrical conductivity to reduce the shunting effect on TIs due to the presence of common metallic materials in the applicable devices.(*115*) Indeed, despite the

remarkable charge-spin conversion efficiency in TI, doubts were cast on whether TIs could truly reduce the power dissipation in applicable devices since TIs are generally more resistive compared to other SOC materials, thus leading to a severe shunting effect that counteracts the increased θ_{SH} when integrated with widely used magnetic metals. Therefore, we evaluated the normalized switching energy per unit magnetic volume ($P \propto \rho/{\theta_{SH}}^2$) and summarized it in Table 3-1 for a comparison between different SOC materials.(*62*) As shown in Table 3-1, the presented TI-based heterostructure doubtlessly possesses an advantage over conventional heavy metals regarding energy efficiency. Furthermore, the θ_{SH} and the switching power dissipation of the TI/Mo/CoFeB/MgO structures after annealing at T_A >350 °C remain comparable to other TI-based devices, underlining their outstanding thermal tolerance and great potential in applications.

3.4 Summary

Motivated by the advantages predicted for TIs as a spin current source with unprecedented charge-spin conversion efficiency, Chapter 3 presented two research projects that focused on tackling some of the key challenges in leveraging TIs to enhance the energy efficiency of spintronic applications, particularly for the SOT-based memory and logic devices.

The first challenge addressed in this chapter was to definitively quantify the intrinsic charge-spin conversion efficiency of TIs, as there have been huge unsettle discrepancies among the earlier reported data, which seriously hampered the understanding of the SOC-related physics in TIs and the development of TI-based spintronic devices. To address this issue, the MOKE SOF magnetometer introduced in Section 2.4 was used to investigate the SOC-related phenomena and the charge-spin conversion efficiency in a TI/Cr-doped TI heterostructure. Unlike other traditional techniques, the MOKE results clearly manifested the characteristics of SOF-driven macroscopic

magnetization oscillations. These data's validity and accuracy were further verified by measuring the SOF-induced shifts in hysteresis loops and observing a solid consistency. In this respect, this work marked a major step toward resolving the previous discrepancies and offering a reliable probe to the charge-spin conversion efficiency and the SOF-driven physics in TI-based magnetic systems. Using this MOKE SOF magnetometer, a relatively large DL-SOF was confirmed in the TI/Cr-doped TI heterostructure at 12K, and the temperature dependence of the charge-spin conversion efficiency in TIs was also studied. The findings suggest that the giant SOFs produced by TI would likely survive at a higher temperature if the coupled magnetic orders could be maintained.

Along this line, a more applicable TI-based magnetic structure was developed for room temperature operation. By inserting a thin layer of Mo, the industrially mainstream ferromagnetic CoFeB/MgO system with strong perpendicular anisotropy was successfully grown on TI, and highly efficient current-induced magnetization switching was also realized at room temperature. Moreover, the studies on these TI/Mo/CoFeB/MgO structures annealed at different temperatures revealed that the perpendicular anisotropy and the current control of magnetization were stable against an elevated annealing temperature up to 400 °C. This offers superior thermal tolerance and a large annealing window for the back-end-of-line processes in the modern semiconductor industry. The deterministic switching achieved with the assistance of an in-plane field was attributed to the giant SOFs generated by TI under an in-plane charge current injection. Supported by careful calibration of the power dissipation and the intrinsic charge-spin conversion efficiency, the energy efficiency of these TI/Mo/CoFeB/MgO structures is at least one order of magnitude higher than conventional heavy metals at room temperature. Surprisingly, the TI/Mo/CoFeB/MgO structure's performance was enhanced as the annealing treatment temperature increased. The analysis of the TEM images and the interface quality revealed that the annealing-enhanced interface quality was

likely realized because of the protection provided by the Mo insertion layer and was the primary contributor to the performance improvement. This outstanding thermal tolerance combined with the room temperature efficient magnetization manipulation and the desirable magnetic properties in this TI/Mo/CoFeB/MgO structure represents a significant step toward the practical implementation of TI-based SOF devices in the semiconductor industry.

In short, the progress covered in Chapter 3 highlighted a new path towards highly efficient SOT-based spintronic memory and logic devices using TIs.

CHAPTER 4. Laser-Induced Ultrafast Spin Dynamics in a Ferrimagnet with a Vertical Composition Gradient

4.1 Overview

Modern silicon transistor-based electronics commonly operate in the gigahertz frequency range, corresponding to sub-nanosecond timescales. Accordingly, driving spin dynamics or controlling the associated magnetic states on a sub-nanosecond or even shorter timescale has become essential for spintronic devices to compete with the existing electronic devices and eventually revolutionize current technology. At the forefront of developing such ultrafast spintronic applications, ferrimagnets (FIM) have attracted considerable attention as they uniquely combine the advantages of both ferromagnets (FM) and antiferromagnets (AFM) as briefed in Section 1.3. In addition to this unique combination of the AFM-like ultrafast spin dynamics and the FM-like easy accessibility to the internal magnetic states, the inequivalent sublattices also provide extra degrees of freedom for material engineering and integrating novel functionalities. Indeed, it is well known that the properties of FIMs can be continuously tuned by varying their composition, i.e., the ratio between the constituent spin sublattices. This flexibility sheds light on several long-standing issues that have hindered the widespread use of SOT, which is envisioned as one of the most promising approaches to manipulating magnetism with superior efficiency and speed in spintronic devices. One of the most-recognized issues regarding SOT devices, as mentioned in the previous sections, is the need to break IP structural symmetry to some extent for the deterministic switching of perpendicular magnetic moments. This necessity is incompatible with mass production, where structural uniformity across the entire wafer is often required.(*26*) Exploiting the flexibility of FIMs, several researchers innovatively introduced a vertical composition gradient into various ferrimagnetic systems, and the induced variations in magnetic properties enable deterministic SOT

switching while preserving the in-plane structural symmetry.(*116–120*) These results present a major step toward practical SOT-based spintronic devices empowered with high efficiency and great thermal stability. However, the spin dynamics in these novel ferrimagnetic systems with vertical composition gradients and their suitability for high-speed devices have remained largely unexplored.

Reorientating magnetic moments by applying SOFs takes place on sub-nanosecond timescales and generally involves certain spin precession processes, which can be described analytically using the Landau–Lifshitz–Gilbert–Slonczewski Equation

$$\frac{\partial \boldsymbol{m}}{\partial t} = -\gamma \boldsymbol{m} \times \boldsymbol{H}_{\text{eff}} + \alpha \boldsymbol{m} \times \frac{\partial \boldsymbol{m}}{\partial t} + \boldsymbol{\tau} \tag{4-1}$$

where $\boldsymbol{m}$ is a unit vector along the magnetization direction; γ is the gyromagnetic ratio; α is the damping factor; $\boldsymbol{H}_{\text{eff}}$ is the effective magnetic field experienced by the magnetic moments and $\boldsymbol{\tau}$ denotes the SOTs associated with the SOFs. Clearly, the magnetic parameters in Equation (4-1), including spin precession/resonance frequency f, damping factor α, and gyromagnetic ratio γ, fundamentally dictate the dynamical processes. Intuitively, these dynamical parameters should have strong dependences on the structural uniformity and the exchange interaction between sublattices. This is because the inhomogeneous distribution of magnetic moments or magnetic anisotropy gives rise to an extra extrinsic damping component in addition to the intrinsic damping of materials.(*121*, *122*) Given that the vertical composition gradient naturally introduces additional inhomogeneities, it is of great importance to examine whether this incorporation of a vertical composition gradient will affect or even degrade the desirable high-frequency features of FIMs. Without a doubt, characterizing these ferrimagnetic structures will provide the information and potentially spark innovations for developing high-speed SOT-based spintronic memory and logic devices.

To this end, in Chapter 4, the dynamical properties of a ferrimagnetic GdFeCo thin film with a vertical composition gradient are comprehensively characterized using the optical pump-probe technique introduced in Section 2.3, i.e., the time-resolved magneto-optical Kerr effect (TR-MOKE) measurements. With particular emphasis on the dynamics related to SOF-induced switching, i.e., the spin precession/resonance motions, the experimental conditions, and material systems are carefully optimized and discussed in detail.

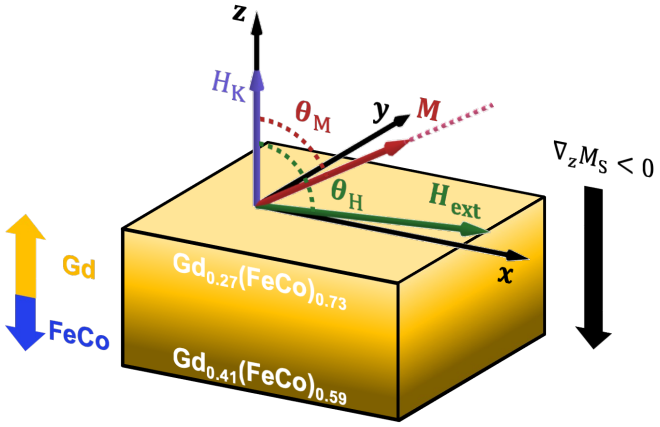

Figure 4-1. Ferrimagnetic GdFeCo with a vertical composition gradient. Schematic of the GdFeCo thin film with a vertical composition gradient chosen for this study. The thickness of this thin film is 5 nm. In GdFeCo, the two magnetic sublattices (Gd and FeCo) are antiparallel coupled. Note that the net magnetization is fully compensated with a composition of $Gd_{0.25}(FeCo)_{0.75}$, and hence, the structure is expected to exhibit a Gd-rich behavior at room temperature. The θ_H denotes the angle between the field direction and z-axis and the θ_M denotes the angle between the equilibrium magnetization direction and z-axis.

4.2 Magnetic Properties of a GdFeCo Film with a Vertical Composition Gradient

GdFeCo is a well-known prototypical metallic FIM in the study of femtosecond magnetism and has pronounced magneto-optical effects for the ultrafast magneto-optical recording.(*123*) In this

rare earth-transition metal amorphous alloy, the Gd and FeCo sublattices are aligned antiparallelly by the strong exchange interaction, and the composition ratio (x_{Gd}:x_{FeCo}) between these two sublattices plays a decisive role in both the static and dynamic properties of GdFeCo.(*44*) The counteraction between FeCo and Gd sublattices generally gives rise to two types of compensating behaviors in GdFeCo as presented previously in Figure 1-4b of Section 1.3.2: (1) At $x_{\mathrm{Gd}}M_{\mathrm{Gd}} = x_{\mathrm{FeCo}}M_{\mathrm{FeCo}}$, the net magnetization is nearly zero like an AFM, resulting in a large coercivity field and high magnetic anisotropy energy; (2) At $x_{\mathrm{Gd}}(M_{\mathrm{Gd}}/\gamma_{\mathrm{Gd}}) = x_{\mathrm{FeCo}}(M_{\mathrm{FeCo}}/\gamma_{\mathrm{FeCo}})$, the total angular momentum of GdFeCo vanishes while finite net magnetic moments remain. Therefore, on approaching this angular momentum compensation point, the spin dynamics accelerate dramatically, and the nonzero magnetic moments can still acutely couple to external fields or probes.(*44*, *45*)

The GdFeCo thin films investigated in Chapter 4 were deposited on a Si/SiO_2 thermal oxide silicon substrate using a radio-frequency magnetron sputtering system in a 3 mTorr sputtering gas of Ar at room temperature with a base pressure of 1×10^{-8} Torr. During the growth, off-axis Gd and FeCo targets, which are mounted at the opposite sides of the sputtering chamber, were co-sputtered to form $Gd_{1-x}(FeCo)_x$ while the substrate was continuously rotated to ensure uniform thickness/composition across the entire film.(*120*, *124*) The deposition rates of Gd and FeCo were mainly determined by the respective target powers, and hence, the composition of $Gd_{1-x}(FeCo)_x$ film and the associated magnetic properties can be continuously adjusted by varying the target powers. To introduce a vertical composition gradient into the $Gd_{1-x}(FeCo)_x$ thin film, the power of the Gd target was fixed at 20 W while the target power for FeCo was linearly ramped up from 45 W to 85 W during the growth, forming a composition profile with $Gd_{0.41}(FeCo)_{0.59}$ at the bottom and $Gd_{0.27}(FeCo)_{0.73}$ at the top as shown in Figure 4-1. For simplicity, this $Gd_{1-x}(FeCo)_x$ thin film

with a vertical composition gradient is named z-gradient GdFeCo throughout this chapter. The total thickness of this z-gradient GdFeCo layer is 5 nm, and by assuming a linear change in the composition ratio, the composition gradient is quantified using the gradient in the FeCo concentration of, i.e., $\partial_z x_{\mathrm{FeCo}} \approx 0.03$ nm^{-1}, corresponding to a gradient in the saturation magnetization $\partial_z M_{\mathrm{S}} \approx 82$ emu cm^{-3} nm^{-1}.(*79*) At room temperature, this z-gradient GdFeCo is expected to resemble a uniform Gd-rich GdFeCo in terms of magnetic signals, given that the lowest Gd concentration ~0.27 in this z-gradient GdFeCo is still higher than the compensation concentration of ~0.25 commonly reported in previous studies.(*79*, *125*, *126*) In addition to composition, the two compensation conditions can also be satisfied by varying the temperature, namely, reaching either the magnetization compensation temperature T_{MC} or the angular momentum compensation temperature T_{AMC}. In GdFeCo, the FeCo sublattice possesses a larger magnetization than the Gd sublattice at temperatures above the T_{MC}, which means the magnetic moments of the FeCo sublattice will align with the external field while those of the Gd sublattice will be aligned antiparallel. In contrast, at below the T_{MC}, the Gd sublattice will align with the external field while the FeCo is antiparallel to the external field. Based on earlier studies,(*46*) the T_{AMC} is slightly higher than the T_{MC} in this sample given the respective temperature dependencies of the FeCo sublattice and Gd sublattice. For the z-gradient GdFeCo studied here, the T_{MC} is evaluated to be 330 K from temperature-dependent SQUID measurements as presented in Figure 4-2a and 4-2b. In Figure 4-2b, a large positive (negative) field ~500 mT was first applied to saturate the sample at a temperature above the T_{MC} and the temperature dependence of the SQUID signal is acquired with a small positive (negative) magnetic field ~10 mT applied to maintain the direction of magnetic moments. The magnetization state of each sublattice is marked on the four corns of Figure 4-2b, and the curve corresponds to the case of initializing the sample with a positive

(negative) field at room temperature is colored in red (blue). From the crossing of the blue and red curves, the T_{MC} is estimated to be ~330 K, which is particularly beneficial for this study as it ensures a sufficient temperature margin such that the sample will not be easily heated above T_{MC} or T_{AMC} by the high-power laser during the experiments described in the next section. From an experimental point of view, avoiding the possible involvement of T_{AMC} and T_{MC} in this way considerably facilitates the data analysis for extracting the desirable dynamical parameters.(*127*) In the meantime, the z-gradient GdFeCo film does not significantly deviate from the compensation points where the existence of ultrafast spin dynamics is anticipated, as indicated by a small M_{S} < 20 emu cm^{-3} within the temperature range of 285 K to 360K. Based on such a temperature profile, the dominance of Gd in z-gradient GdFeCo is ensured throughout Chapter 4, and this dominance of Gd sublattice was also directly seen from the MOKE signals (θ_{K}) of the z-gradient GdFeCo sensed with a λ = 800 nm laser. In this situation, the MOKE signal of GdFeCo is almost entirely contributed from the FeCo sublattice and the opposite polarity of the $\theta_{\mathrm{K}} - H_z$ loop of a z-gradient GdFeCo sample (as shown in Figure 4-2c) with respect to that of the $M - H_z$ curve (Figure 4-2a) indicates the FeCo sublattice is antiparallelly aligned with the net magnetic moments, concluding that the Gd sublattice dominates in this z-gradient GdFeCo sample. The $\theta_{\mathrm{K}} - H_z$ loop in Figure 4-2c also yields a saturation magneto-optical Kerr angle $\theta_{\mathrm{S}} \approx 2.4$ mrad, which is used to normalize the optical signals throughout Chapter 4. The magnetic properties of this z-gradient GdFeCo film are also characterized using a magneto-transport approach which can provide high-field IP scans. For this purpose, the thin film was fabricated into a 20 μm × 130 μm Hall bar structure, and its anomalous Hall resistance as functions of external fields along different field directions was measured in a Quantum Design physical property measurement system.

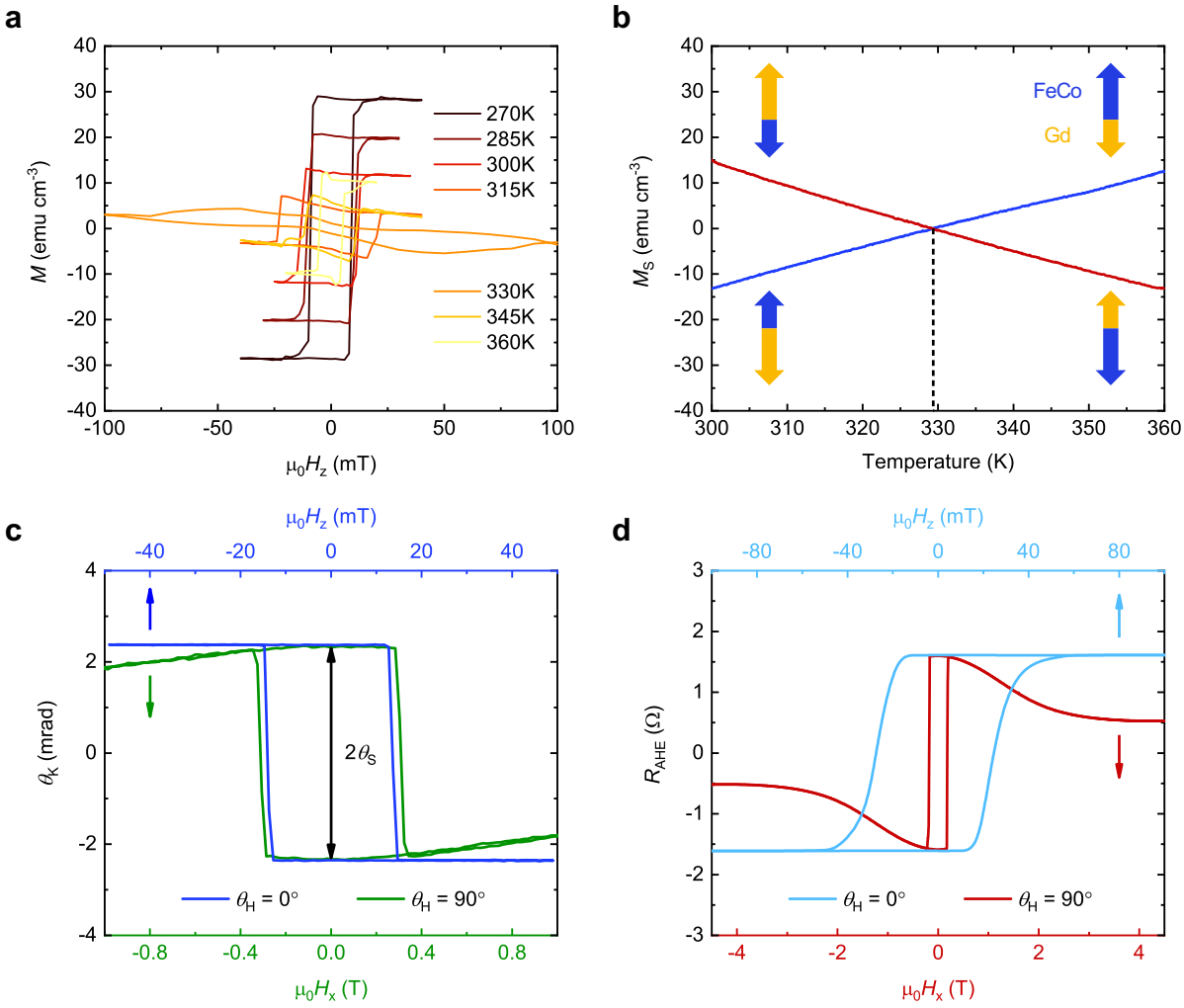

Figure 4-2 Magnetic properties of a GdFeCo thin film with a vertical composition gradient from $Gd_{0.41}(FeCo)_{0.59}$ at the bottom to $Gd_{0.27}(FeCo)_{0.73}$ at the top. a. Out-of-plane magnetic hysteresis loops measured by a SQUID system at different temperatures. The results imply a T_{MC} ~330 K at which the saturation magnetization is diminished and the magnitude of the coercivity field diverges. **b.** Saturation magnetization along the OP direction as a function of temperature. At the beginning of the measurement, a large field of ~500 mT was applied to align all the magnetic moments. During the measurement, a small field of ~10 mT along the easy axis was used to maintain the magnetic states while the temperature increased from room temperature to ~360 K. Specifically, the red and blue curves are obtained by initializing the sample with positive and

negative fields respectively at room temperature, and the associated magnetization states are indicated at the four corns. The magnetization compensation temperature can be precisely determined from the crossing of two curves as marked by the black dashed line. **c.** MOKE hysteresis loops with fields applied along OP (blue) and IP (green) directions, respectively. The polarity of the optical hysteresis loops reveals the dominance of the Gd sublattice in the z-gradient GdFeCo sample. **d.** Transport hysteresis loops measured on a Hall bar device with fields applied along OP (sky-blue) and IP (red) directions, respectively. The SQUID, optical, and transport results all confirm the establishment of strong perpendicular magnetic anisotropy in the sample.

The OP magnetic (Figure 4-2a), MOKE (Figure 4-2c), and magneto-transport (Figure 4-2d) hysteresis curves all confirm a strong uniaxial PMA with an easy axis along the z-direction, and a coercivity field H_{C} of ~5 mT is determined from the optical measurements. From the high-field magneto-transport measurement, an IP saturation field of ~4 T is obtained, which is commonly used as an estimate of the effective anisotropy field H_{K}. Accordingly, the anisotropy energy density $K = M_{\mathrm{S}}H_{\mathrm{K}}/2$ is on the order of 10^5 J m^{-3}, revealing a substantial PMA in this z-gradient GdFeCo sample, which is no surprise given its nearly compensated condition. This PMA energy can easily satisfy the requirement for achieving a thermal stability factor $\Delta > 45$ at room temperature for a miniaturized device size of <50 nm. It should be noted that the discrepancies between these hysteresis loops can be simply ascribed to the different sizes of the probing region and the largely distinct test sample preparation required for each probing technique.

4.3 Characteristics of Laser-Induced Ultrafast Spin Dynamics

The dynamical responses of the magnetic material play a central role in determining the operating speed of spintronics devices. Hence, to fully exploit and examine the potentials of z-gradient GdFeCo for high-speed spintronic applications, comprehensive characterization and insights into the dynamical properties of this system are essential. Aiming for this, an all-optical pump-probe technique was deployed to measure the time-resolved magneto-optical Kerr effect in the z-gradient GdFeCo. Considering the technological relevance of the precessional switching to most near-term methods for controlling magnetization, this pump-probe technique utilizes femtosecond laser pulses to thermally trigger the spin precession dynamics in the sample for the investigation. By probing the TR-MOKE signals, which capture these dynamics, key dynamical parameters such as spin resonance/precession frequency and damping factor could be obtained. This section will elaborate on the experimental setup and theoretical considerations for the TR-MOKE measurements on top of Section 2.3. Additionally, the magnetization dynamics and the extracted dynamical properties as functions of external fields are presented and discussed in detail.

As briefly covered in Chapter 2, the all-optical pump-probe setup employed for TR-MOKE measurements is sourced with an amplified Ti:Sapphire femtosecond laser. This femtosecond laser features a central wavelength λ = 800 nm and a repetition rate of 1 kHz. The laser beam is split into two with an intensity ratio of 9:1 for pumping and probing, respectively. To thermally excite the ultrafast spin dynamics, the pump beam is incident onto the sample with an angle of ~16º from the z-axis, and a lens with a focal length of 250 mm is used to focus the pump pulse into a spot of 100 μm in diameter, producing a fluence of 0.1 mJ cm^{-2} to 10 mJ cm^{-2} per pulse on the sample. To probe the excited transient magnetic states, a time-delayed probe pulse is set to normal incidence and focused into a smaller spot that overlaps with the pump spot using a 200 mm lens. In

this normal incidence geometry, the polar MOKE dominates, and hence, the optical signals are most sensitive and linearly proportional to the z-component of magnetization of the FeCo sublattice.(*49*) Compared to the pump arm, additional optics are added to linearly polarize the probe arm, causing additional attenuation in its intensity. Therefore, the fluence of a probe pulse measured at the sample is around 0.01 mJ cm^{-2}, which is at least one order lower than that of a pump pulse. The chirp of the femtosecond light source was optimized for the probe pulse duration on the sample side, which was measured to be ~160 fs with an autocorrelator. In the measurement, an extra modulation on the pump arm by an optical chopper at 37 Hz was adapted to improve the signal-to-noise ratio. Because of the strong PMA in the z-gradient GdFeCo, an external magnetic field H_{ext} was applied at an angle of ~6º from the x-axis such that a coherent spin precession motion can be triggered after the initial laser-heating excitation. Ideally, the external field needs to be strong enough to minimize the potential influence of multidomain effects(*128*) and to ensure that the sample relaxes back to the same well-defined initial state after each excitation by the laser pulse. From the shape of the IP and OP hysteresis loops shown in Figure 4-2c, it can be seen that a H_{ext} larger than ~0.4 T is sufficiently high to keep the z-gradient GdFeCo sample in a single-domain state that is tilted slightly away from its easy axis at rest. For separating common artifacts and isolating the optical signals originating from thermally excited magnetic states, the TR-MOKE measurements were repeatedly carried out at both positive and negative H_{ext} and the difference was extracted as the experimental results.(*128*) The schematic, configuration, and axes conventions of this TR-MOKE measurement are illustrated in Figure 4-1.

Given the ultrahigh transient power inherent to this femtosecond pump-probe technique, the laser damage threshold of the sample needs to be pre-determined. A series of test samples were exposed to pump pulses of different powers for 10 minutes, and the optical hysteresis loops were measured

before and after each exposure, as shown in Figure 4-3. By comparing the hysteresis loops before and after exposure, it appears that no laser-induced irreversible change was observed until the pump fluence reached 3 mJ cm^{-2}. Based on these results, the TR-MOKE measurements in Chapter 4 were carried out with a pump fluence less than 2.5 mJ cm^{-2}. While GdFeCo has received extensive studies for femtosecond laser-driven all-optical magnetization reversal,(*123*) however, the optical fluence used in Chapter 4 was relatively low for triggering all-optical magnetization reversal, allowing the presented studies to focus on the laser-induced spin precession process. It is noteworthy that although the laser pulses did not permanently damage the sample, a sizable amount of heat was still deposited into the sample, and thus, unavoidably altered the experimental conditions. Fortunately, based on the pump-induced temporary changes in the coercivity field, the local increase in sample temperature caused by a pump beam of 2.5 mJ cm^{-2} with a 1 kHz repetition rate was experimentally calibrated to be less than 15 K, producing acceptably minor thermal background on the experiments and has been accounted in all following measurements. Notably, such heating was obviously insufficient to bring the sample above its T_{MC}.

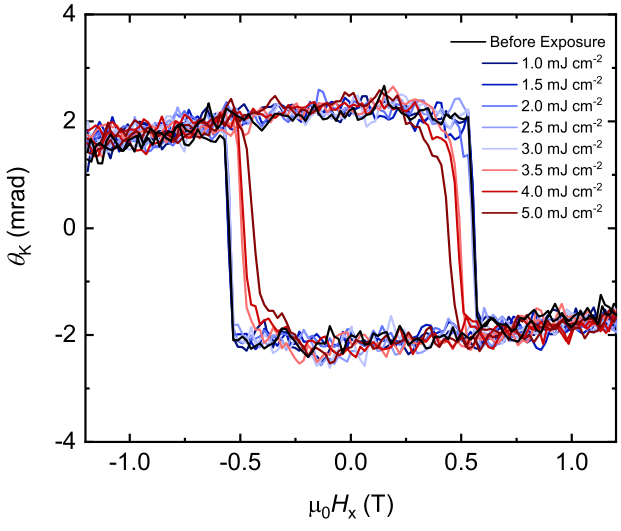

Figure 4-3. Determination of laser damage threshold in the *z*-gradient GdFeCo. The laser damage threshold was determined by observing whether the optical hysteresis loop was altered

after exposure to the pump laser for an extended amount of time. An irreversible change was observed after exposure to the pump pulses with fluence above 3 mJ cm^{-2}, indicating the sample was damaged under this fluence.

Figure 4-4a depicts representative TR-MOKE signals collected from a z-gradient GdFeCo film excited with a pump fluence of 0.3 mJ cm^{-2} at Δt = 0 ps for $\mu_0 H_{\mathrm{ext}}$ = ±1.2 T. Note that all optical signals are normalized to the saturation Kerr rotation θ_{S} (as defined in Section 2.4 and extracted from Figure 4-2c) and offset for clarity. The perfect antisymmetry between the temporal traces of the θ_{K} under positive and negative fields can be explained by their thermal origins.(*128*) Moreover, a strong field dependence (will be discussed in detail later) is also observed, affirming that these optical signals are rooted in magnetic states. As expected, the TR-MOKE traces feature two widely-observed laser-induced ultrafast magnetization dynamics, namely, the demagnetization process (Figure 4-4b) and the spin precession process (Figure 4-4c). Overall, with the aid of H_{ext}, a damping coherent spin precession (Δt > 20 ps) was initiated following the sudden demagnetization (Δt = 0 ps) and fast remagnetization (Δt = 0 ~ 20 ps) driven by the intense laser heating.(*129*)

More specifically, before the excitation, magnetic moments are tilted away from the magnetic easy-axis by H_{ext} and the equilibrium direction is determined by balancing between H_{ext} and the effective anisotropy field H_{K}. Upon the action of the intense femtosecond pump at zero delays, the sample is instantaneously heated, accompanied by a sharp reduction of ~5% in the magneto-optical signal. This is because the transient laser heating changes the magnitudes of both magnetization and anisotropy field (magneto-crystalline anisotropy field and shape anisotropy field), establishing a new short-lived quasi-equilibrium condition.(*130*) Within the next ~20 ps, the magnetization

starts to restore and moves toward this temporary equilibrium direction. It should be stressed that this quasi-equilibrium direction constantly varies as both the magnetization and anisotropy gradually recover during this temporal regime. Therefore, it is hard to observe a clear and complete precessional motion in this stage. After the first 20 ps, the excess heat diffuses through the thermal equilibration among electron, spin, and lattice systems, and the initial equilibrium position is re-established. Thereby, the magnetization returns to this rest position via a damped coherent precession motion during a temporal regime of hundreds of picoseconds.(*129*)

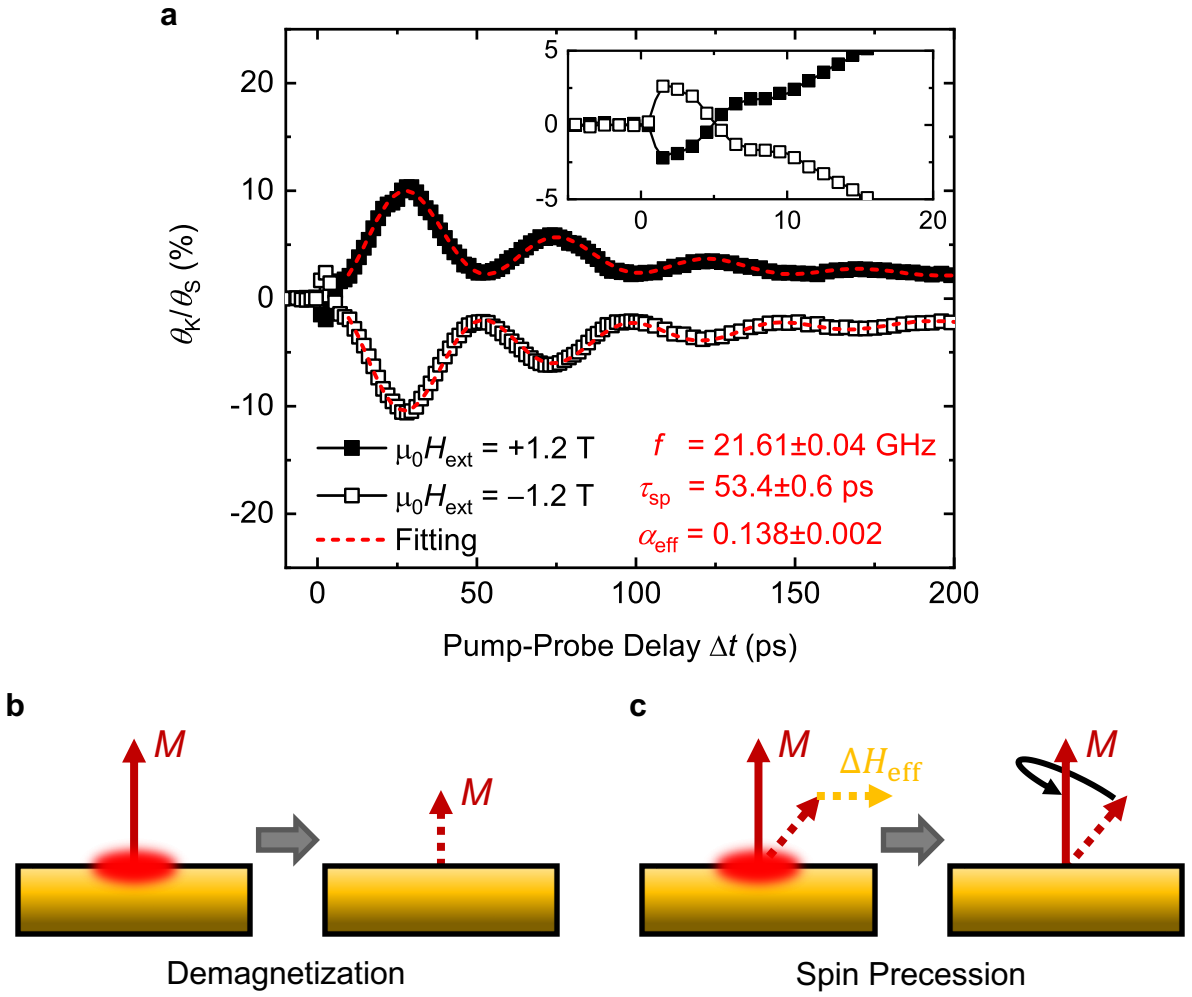

Figure 4-4. Laser-induced ultrafast magnetization dynamics and TR-MOKE signals. a. Typical TR-MOKE signals measured as a function of time delay under positive and negative

external fields H_{ext}. The measurements were conducted with a pump fluence of 0.3 mJ cm^{-2} and external fields $\mu_0 H_{\mathrm{ext}} = \pm 1.2$ T. The red dashed lines represent fits to Equation (4-2), and perfect fitting is achieved with the listed parameters. These TR-MOKE traces exhibit two different ultrafast processes triggered by the pump pulses, namely, the demagnetization and the coherent spin precession. The inset shows the enlarged TR-MOKE signals for the first 20ps after the laser excitation. **b.** Schematic of the laser-induced demagnetization. Upon being heated by an intense pump pulse, the magnetization is weakened. It is worth noting that for FIMs, an increase in sample temperature does not necessarily lead to a decrease in magnetization. As shown in Figure 4-2b, a rise in sample temperature can also result in larger magnetic moments. **c.** A pump pulse can also act as a transient change in the effective external field (ΔH_{eff}) onto the sample. For example, the laser heating results in a reduction of the magnetic anisotropy field. This transient change drags the magnetic system away from its equilibrium state, and thereafter, the sample will undergo a spin precession motion to return back to its original equilibrium state. Notably, the dashed lines in **b** and **c** denote the momentary non-equilibrium states created by the ultrafast laser excitation.

It is widely accepted that the damped magnetization precession is associated with the relaxation of energy from the heat-excited coherent magnons to lattice or incoherent magnons.(*131*) This long-lived oscillatory behavior, in the temporal regime $\Delta t > 20$ ps, is of particular interest for extracting the key dynamical magnetic properties, and thus, is primarily focused on for the presented studies. It appears that only one homogenous single-frequency spin resonance mode, namely, the ferromagnetic resonance mode, is observed from this oscillatory. Another mode that has also been commonly reported in FIMs, the exchange mode, was not observed here. This absence of the exchange mode was expected, because the pump fluence used in these experiments was not

sufficient to bring the sample temperature above or close to the vicinity of compensation points, which will be demonstrated experimentally in the following sections. Crossing or approaching the compensation temperatures is essential for the excitation of the exchange mode, since it is only under these conditions will the antiferromagnetic exchange interaction in FIMs be softened enough to allow the magnetization direction to deviate considerably from the exchange field, and thus, enabling the exchange mode to resonate with a greater amplitude that can be observed.(*46*, *127*) While the details of underlying microscopic mechanisms of these laser-induced ultrafast processes have been largely debated, useful dynamical parameters can be extracted from this damped single-frequency oscillation by fitting it to a phenomenological equation:

$$\theta_{\mathrm{K}} = A_1 \cdot \sin(2\pi f \Delta t + \varphi) \cdot e^{-\Delta t/\tau_{\mathrm{SP}}} + A_2 \cdot e^{-\Delta t/\tau_{\mathrm{BG}}} + A_3 \quad (4\text{-}2)$$

where A_1, A_2, and A_3 are the amplitudes of coherent magnon oscillation, exponentially decaying thermal background, and offset, respectively; The τ_{SP} and τ_{BG} denote the relaxation/decaying time constant of the coherent magnon and the background; f is spin resonance/precession frequency; φ is the excitation-related phase factor. As demonstrated in Figure 4-4a, this model fitting (dashed red line) by a least-squares method successfully reproduces the experimental results (symbols), yielding reliable estimates of the spin precession frequency and relaxation time with relatively small uncertainties, as listed in Figure 4-4a. This perfect fitting again indicates that the ferromagnetic mode dominates in this measurement. Directly from these fitting results, the effective damping constant α_{eff}, a widely accepted measure of how fast the energy and angular momentum can be dissipated or transferred from the magnetic system into other systems in materials, can also be headily evaluated based on $\alpha_{\mathrm{eff}} = 1/2\pi f \tau_{\mathrm{SP}}$, which is 0.138 in this measurement. This α_{eff} value also agrees well with those typical values obtained in GdFeCo.(*46*) This α_{eff}, however, not only contain intrinsic contributions that reflect the material properties but

also takes in extrinsic contributions that depend on the inhomogeneities/multidomain of the sample's magnetic properties, spin pumping into the adjacent areas, and the experimental conditions (such as the direction of H_{ext}, the strength of H_{ext}, and the pump fluence) Therefore, the dependences of f, τ_{SP}, and α_{eff}, on H_{ext} need to be systematically investigated to better understand how the vertical composition gradient can affect the dynamical behaviors.

Thereby, the TR-MOKE measurements depicted in Figure 4-4a were repeated at various H_{ext} from 0.2 to 1.2T, and the same model fitting to Equation (4-2) was performed to determine the values of f, τ_{SP}, and α_{eff} as summarized in Figure 4-5. Note that at H_{ext} < 0.2T, it appears that spin oscillation stopped before completing a full precession cycle. Therefore, the data acquired at H_{ext} < 0.2T are not suitable for reliable extraction of the dynamical parameters. When H_{ext} increases from 0.2 to 1.2T, the ferromagnetic resonance frequency f monotonically increases from 15 to 22 GHz with a quantitative agreement with that calculated using the fast Fourier transform (FFT). This field dependence can be described by an approximated Kittel model, which is derived in Ref.(*46*) for a similar experimental configuration and a GdFeCo sample with robust PMA, with an anisotropy field $\mu_0 H_{\mathrm{K}}$ = 1.70±0.09 T. This H_{K} value is significantly lower than that estimated from Figure 4-2d, such discrepancy is likely because the intense pump pulse elevates the background temperature of the sample and weakens its anisotropy.

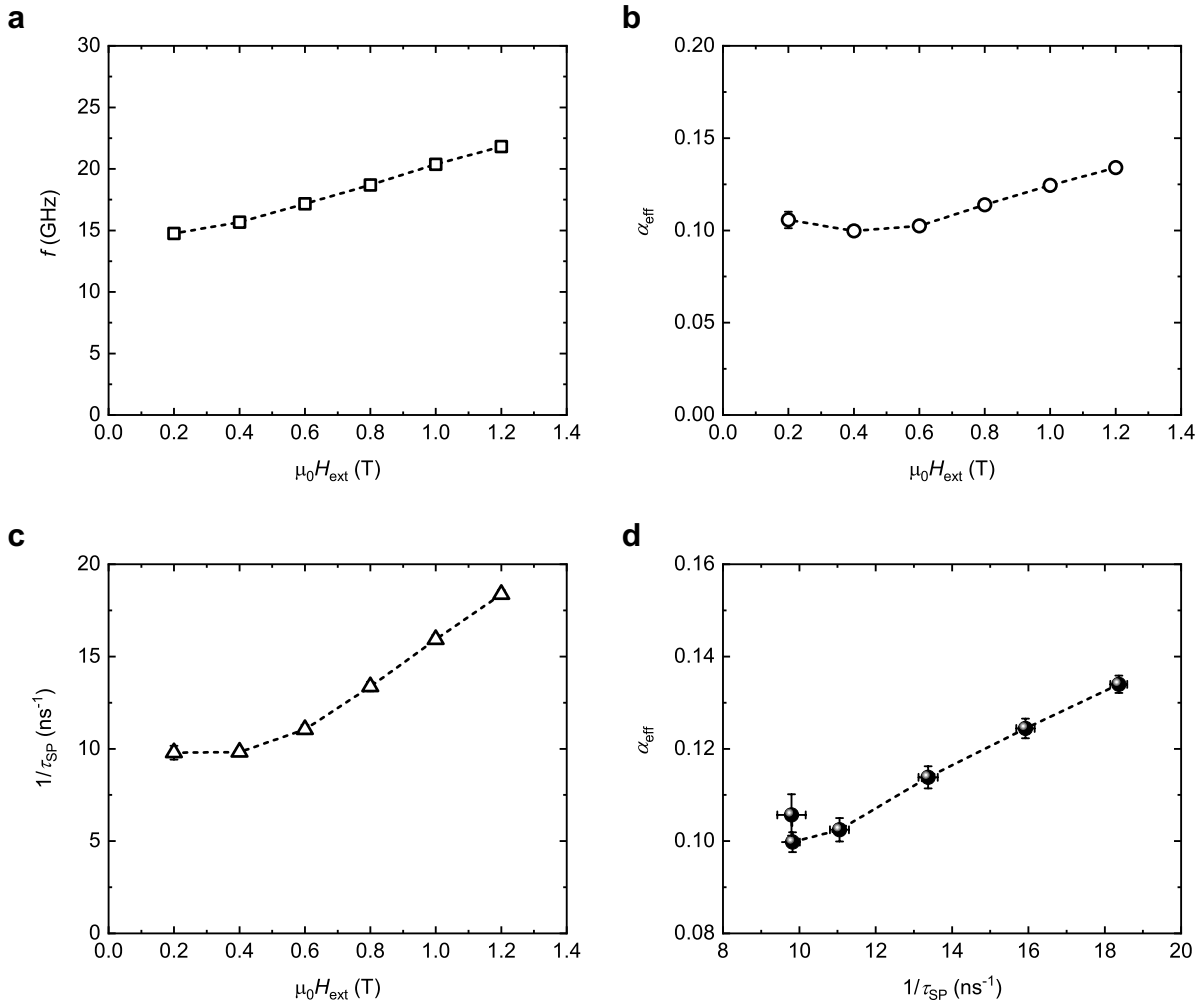

Figure 4-5. Key dynamical properties of a GdFeCo thin film with a vertical composition gradient from $Gd_{0.41}(FeCo)_{0.59}$ at the bottom to $Gd_{0.27}(FeCo)_{0.73}$ at the top. a, b, and **c** are the IP field dependence of spin precession frequency f, the damping factor α_{eff}, and the magnon relaxation time τ_{SP}. The inverse of magnon relaxation time, i.e., $1/\tau_{\mathrm{SP}}$ serves as a simple measure of the intrinsic damping factor. All three parameters increase with the H_{ext}. **d.** The $\alpha_{\mathrm{eff}} - 1/\tau_{\mathrm{SP}}$ curve provides insights into the extrinsic and intrinsic components of the damping factor as $1/\tau_{\mathrm{SP}}$ can serve as a simple measure of the intrinsic component of the damping factor. The apparent linear correlation between the α_{eff} and the $1/\tau_{\mathrm{SP}}$ suggests a dominant role of the intrinsic component in the experimentally-obtained damping factor.

Compared to the resonance frequencies, α_{eff} exhibits a less pronounced field dependence with the modest increase at larger H_{ext}. However, this is unexpected as the α_{eff} contains both intrinsic and extrinsic contributions. The extrinsic parts, which are mainly attributed to the inhomogeneities of the sample and magnon scattering processes, depend strongly on the external field.(*121*, *132*) To further examine this observation, the intrinsic damping contributions are evaluated from the inverse relaxation time (i.e., $1/\tau_{\mathrm{SP}}$) given that $1/\tau_{\mathrm{SP}}$ is linearly related to the intrinsic damping when the sample is in a single domain state that the inhomogeneous broadening of the spin precession is presumably minimized.(*132*, *133*) Similar to the field dependence of α_{eff}, the $1/\tau_{\mathrm{SP}}$ also increases with the H_{ext}. Noticeably, when the α_{eff} is plotted as a function of the $1/\tau_{\mathrm{SP}}$ in Figure 4-5d, an apparent linear relationship between the two can be found, except for outlying one datapoint associated with $\mu_0 H_{\mathrm{ext}}$ = 0.2 T. This discrepancy can be ascribed to the fact that at a low field regime, the sample does not stay in a single domain state and the resulted inhomogeneities lead to that: (1) the linear relationship between the inverse relaxation time and the intrinsic damping is no longer valid; (2) the external field becomes insufficient to suppress the extrinsic components of α_{eff} as the value of α_{eff} is larger than what is interpolated from a linear fitting on the $\alpha_{\mathrm{eff}} - 1/\tau_{\mathrm{SP}}$ curve; (3) the sample was not brought back to its initial state after each thermal perturbation by the intense pump pulses, causing the experimental results to be less reliable. Indeed, this explanation is also supported by the MOKE hysteresis loop shown in Figure 4-2c, where only at $\mu_0|H_{\mathrm{ext}}| \geq 0.4$ T, a single magnetization state is defined. With this analysis, it is concluded that the obtained α_{eff} is predominated by the intrinsic damping of the z-gradient GdFeCo sample, and therefore, does not manifest a strong field dependence. Based on these results, to minimize the experimental error that arises from the multidomain states and to simplify the analysis, the TR-

MOKE measurements in the following sections are all conducted at $\mu_0|H_{\mathrm{ext}}|$ ranging from 0.4 T to 1.2 T.

The successful reproduction of the experimental data with reliable model fitting and the remarkable self-consistence among the experimental observations both convince that the spin dynamics probed by the TR-MOKE measurements represent the coherent ferromagnetic precession motion, and the experimental results yield reliable estimates of the key dynamical properties of the z-gradient GdFeCo sample, where the extrinsic effects, such as the effects by experimental conditions, are negligible. The estimated ferromagnetic frequency f of tens of gigahertz and damping factor α of ~0.1 in the z-gradient GdFeCo sample are in good agreement with previous systematic studies on uniform GdFeCo films(*46*), suggesting that incorporating a moderate composition gradient into the GdFeCo not only provides extra design flexibility and substantial technological advances but also preserves the ultrafast dynamical properties of GdFeCo that are desirable for high-frequency spintronic devices.

4.4 Controlling Ultrafast Spin Dynamics by Laser Power

Beyond the precessional processes that can be described conventionally in terms of classical thermodynamics, the intense femtosecond laser can also ultimately disturb the thermodynamic equilibrium among the charge, spin, and lattice degrees of freedom in a magnetic system on an extremely short timescale. Exploring these strongly non-equilibrium and the related processes will create critical insights into elementary mechanisms and the energy flow channels that set the fundamental limits for magnetization manipulation, paving the way toward ultrafast switching strategies for high-speed spintronics devices. Indeed, on the engineering side, ultrafast optical excitation (<1 ps) has been representing, ever since its groundbreaking discovery,(*134*) an

intriguing approach to control magnetization at a much faster speed than the characteristic timescales of spin-orbit interaction (~1–10 ps), spin-lattice relaxation (~1–100 ps), or spin precession (~10–1000 ps) that typically govern the magnetization reversal.(*2*, *135*) While it is therefore expected that optical manipulation of magnetization will revolutionize the field of spintronics toward a range of unprecedentedly high frequencies (~10–100 GHz), the fundamental mechanisms that are responsible for energy and angular momentum transfers between photons, charges, spins/magnons, and lattices/phonons in these ultrashort temporal regimes remain poorly understood. Along this line, the laser-induced spin dynamics are further explored in this section by carrying out the TR-MOKE measurements with different pump fluence. To focus on the potential effects of the composition gradient, control experiments were also performed on a uniform $Gd_{0.35}(FeCo)_{0.65}$ thin film. A significantly different dependence on the pump fluence was observed in the z-gradient GdFeCo sample, indicating that much richer dynamics and physics occur in the z-gradient GdFeCo sample.

Figure 4-6 shows the variation of TR-MOKE signals with an applied field of 1.2 T at different pump fluences ranging from 0.3 mJ cm^{-2} to 2.0 mJ cm^{-2}, in which the results of 0.3 mJ cm^{-2} are adopted from Section 4.3. Offsets are added in Figure 4-6a to improve clarity. As the laser fluence increases, the detected TR-MOKE signals, as shown in Figure 4-6a, are altered dramatically while still featuring two types of processes: (1) a step-like instantaneous demagnetization followed by a partial recovery process in the temporal regime of $\Delta t < 20$ ps; and (2) an exponentially decaying thermal background accompanied by a damped spin oscillatory after a time delay of > 20 ps and subsequently relaxes back to the initial state.

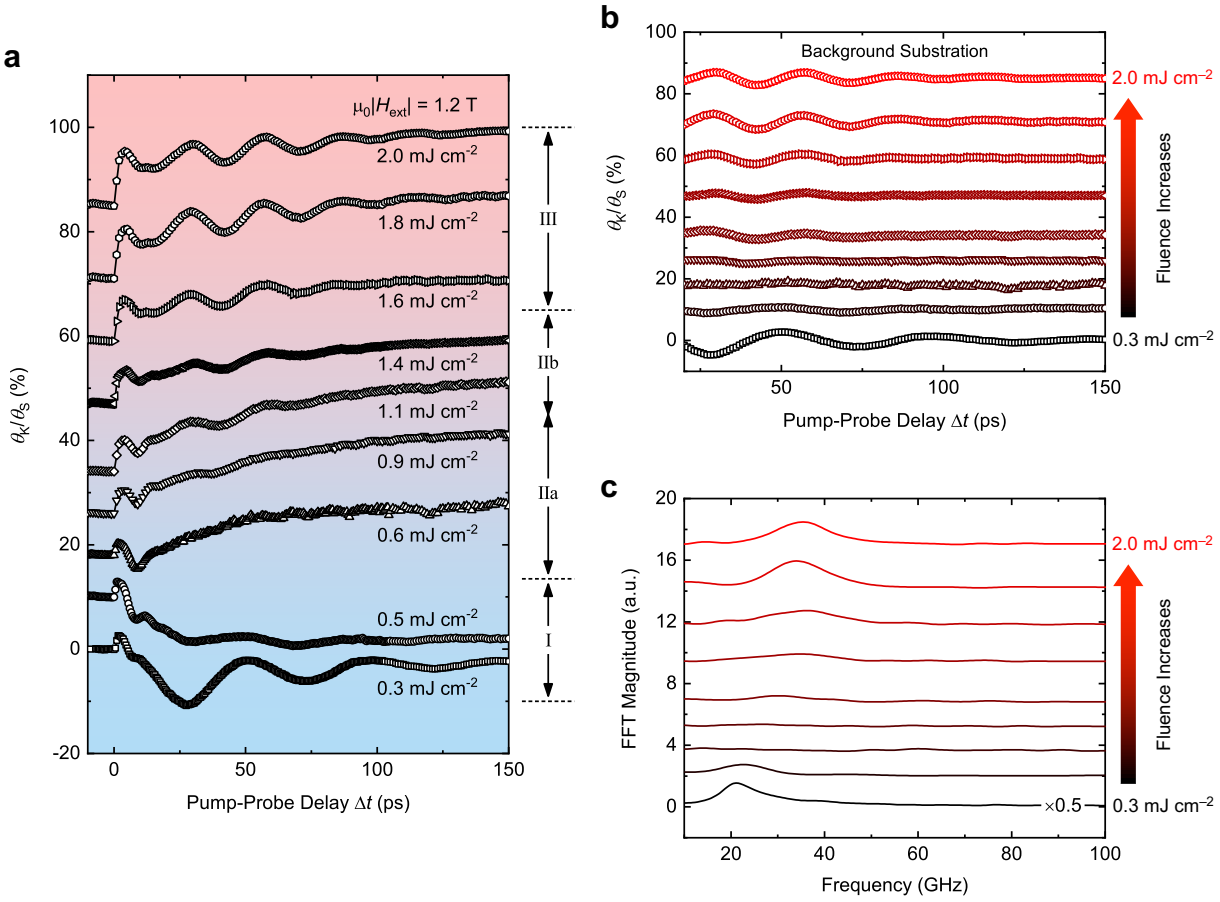

Figure 4-6. Pump fluence dependence of the TR-MOKE signals. a. Experimental TR-MOKE data acquired by the all-optical pump-probe technique at different pump fluences with an external field of 1.2 T. The TR-MOKE traces at different pump fluences differ dramatically. **b.** The spin precession signal separated from the raw data in **a** by subtracting an exponentially decaying thermal background. **c.** The fast Fourier transform of the data presented in **b**. Note that for the curve colors in **b** and **c**, red represents higher pump fluences, while black is for lower pump fluences, corresponding to those in **a**. In all **a**, **b**, and **c**, three distinct regimes (I) <0.6 mJ cm^{-2} (II) 0.6 mJ cm^{-2} ~ 1.4 mJ cm^{-2}, and (III) >1.4 mJ cm^{-2} can be observed.

As demonstrated previously, within the first 20 ps after the impulse of a femtosecond laser, demagnetization occurs at all pump fluences, producing similar changes in the TR-MOKE signals

varying from ~5% for 0.3 mJ cm^{-2} to ~10% for 2.0 mJ cm^{-2} in the same direction. Such a monotonic increase in the demagnetization signals with the pump fluence implies that the ultrafast spin dynamics are mainly heat-driven. Unlike the demagnetization parts of the TR-MOKE signals, the oscillatory parts that represent the spin precession dynamics and heat-excited coherent magnons were substantially modified by the pump fluence.(*131*) To simplify the analysis of precession behaviors, the TR-MOKE signals are first fitted to an exponentially decaying function with offset (i.e., the second and third terms of Equation (4-2)), which is linked to the demagnetization process and thermal background signals. By subtracting these fitting results from the experimental data, the separated oscillatory part of the TR-MOKE signal is plotted in Figure 4-6b for Δt > 20 ps, and three strikingly different regimes can be distinguished: (I) the pump fluence is smaller than 0.6 mJ cm^{-2}; (II) the pump fluence is between 0.6 mJ cm^{-2} and 1.4 mJ cm^{-2}; and (III) the pump fluence is large than 1.4 mJ cm^{-2}. Notably, in Regime I and III, the z-gradient GdFeCo sample behaves as a simple ferromagnet showing a single-frequency spin oscillation, which is ascribed to the ferromagnet resonance mode and can be well-fitted using Equation (4-2) as described in Section 4.3. Based on the fitting results, these two ferromagnetic precession motions, however, are quantitatively distinct and have a 180º phase difference which reveals the magnetization initially moves toward opposite directions. Surprisingly, the spin oscillation remains almost the same for all different pump fluences in Regime III, all of which can be characterized by nearly identical f, α_{eff} and τ_{SP}. Noticeably, the spin precession/resonance frequency in Regime III is ~35GHz, which is significantly higher than that of ~22 GHz in Regime I. In contrast, the relaxation times extracted in both Regime I and Regime III are approximately equal, which are around 60 ps. In Regime II, the oscillatory part appears to gradually transit from the ferromagnetic resonance mode in Regime I to the ferromagnetic resonance mode in Regime

III. Apparently, two evidently different behaviors can be further distinguished in Regime II. When the pump fluence is 0.6 and 0.9 mJ cm^{-2}, denoted by IIa, no oscillation has been observed. However, in the cases of 1.1 and 1.4 mJ cm^{-2} (denoted by IIb), a weak spin oscillation can be recognized. These oscillatory behaviors in Regime IIb are clearly more intricate than those in Regime I and Regime III. Using Equation (4-2) to fit the measured data in Regime IIb yields large uncertainties, which limit further quantitative analysis. This deficient fitting is due to the small magnitude of the oscillatory signals as well as the incomplete precession cycle. On the other hand, it may indicate the possible coexistence of multiple spin oscillation modes with different frequencies. Instead, these frequency characteristics can be directly seen from the FFT spectra presented in Figure 4-6c. A well-resolved single peak can be seen in Regime I and Regime III, with a peak location that agrees well with the fits to Equation (4-2). Figure 4-7 summarizes the fluence dependence of f, α_S, and τ_{SP} extracted from Figure 4-6b. Here, the α_S is a figure of merit that is linked to the value of α_{eff} at a high field of 1.2T, where the effects of inhomogeneities or domain fluctuations can be largely suppressed. For this reason, α_S serves as a simplified measure of the intrinsic damping factor. Based on this simplification, the α_S is either defined as the α_{eff} at $\mu_0 H_K$ = 1.2 T or extracted by fitting the field dependence of α_{eff} to $\alpha_{eff} = \alpha_S + \alpha_0 \exp(-H_{ext}/H_0)$. In the latter case, the α_S represents to the saturation α_{eff} at an infinite H_{ext}. Obviously, the three distinct regimes of the fluence dependences of the TR-MOKE results can also be seen in Figure 4-7.

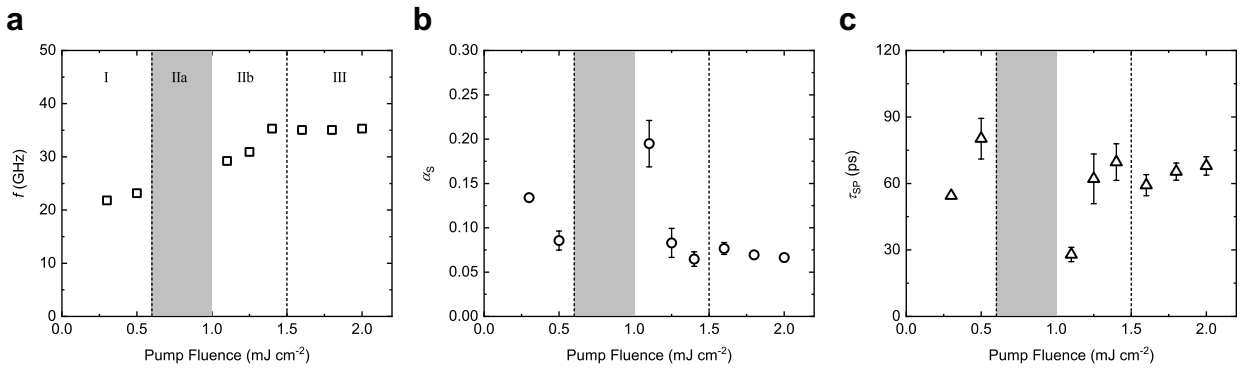

Figure 4-7. Fluence dependence of dynamical properties of a GdFeCo thin film with a vertical composition gradient. a, b, and **c** are the fluence dependences of spin precession frequency f, approximated intrinsic damping factor α_S, and magnon relaxation time τ_{SP}. These parameters are obtained by fitting the experimental results to Equation (4-2). The α_S is then evaluated from either the α_{eff} at $\mu_0 H_K$ = 1.2 T or by fitting the field dependence of α_{eff} to $\alpha_{eff} = \alpha_S + \alpha_0 \exp(-H_{ext}/H_0)$. In this way, the α_S is linked to the α_{eff} at a high field, where the extrinsic components are expected to be strongly suppressed, and therefore, serves as a simple measure of the intrinsic damping factor. In all **a**, **b**, and **c**, three distinct regimes can be clearly identified as those labeled in Figure 4-6a.

This intriguing pump fluence dependence is similar to those reported in a uniform GdFeCo film in earlier studies,(*46*, *127*, *136*) in which the compensation points were involved either by changing the temperature or tuning the composition. Nevertheless, this interpretation, which relies on the possible local elevation of sample temperature above the compensation point (i.e., T_{MC}), is not valid for the pump fluence dependence observed in Figure 4-6. This is because the pump intensity is not high enough to heat the sample to above the T_{MC} as mentioned before in Section 4.3. A closer look into the time traces of the thermally triggered magnetization dynamics is provided by measuring the optical hysteresis loops at different time delays after heating the sample with a pump

pulse of 2.0 mJ cm^{-2}. As reflected by the optical hysteresis loops in Figure 4-8, despite the magnetic moments being noticeably perturbed by the femtosecond laser excitation, the polarity of the signal remains unchanged, conclusively revealing that the sample was not heated above the T_{MC}, even with the most intense pump pulse applied in these measurements.

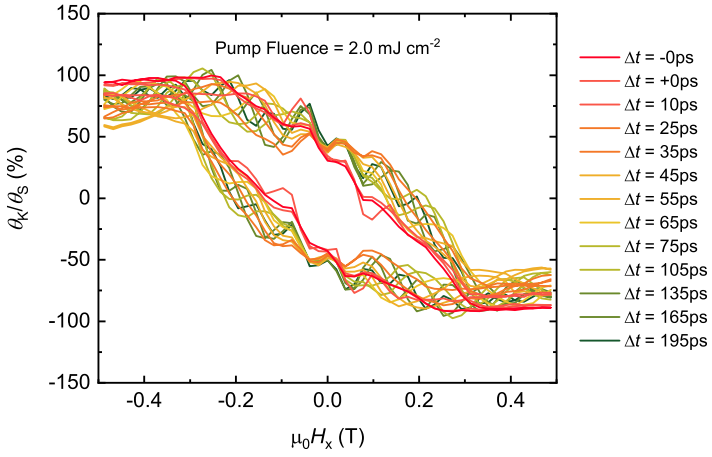

Figure 4-8. Optical hysteresis loops measured at different delays after the transient laser heating. Data are collected with a pump fluence of 2.0 mJ cm^{-2}, which is the highest fluence applied in Chapter 4. Although the optical hysteresis loops at different delays show noticeable differences, the polarity of these hysteresis loops remains unchanged, confirming that the sample temperature is not elevated above the T_{MC} even with the strongest laser heating in this study.

To unambiguously assess the influence of vertical composition gradient on the dynamical properties, especially the peculiar dependence on pump fluence. A series of control experiments were carried out on a uniform Gd-rich $Gd_{0.35}(FeCo)_{0.65}$ film, which represents a trivial case, and the results are summarized in Figure 4-9. This composition is precisely controlled to be the same as the average composition in the z-gradient case ($x_{\mathrm{Gd}}^{\mathrm{avg}} = 0.35$) and is uniform across a total thickness of 5 nm. Figure 4-9a presents both the IP and OP hysteresis loops collected from this

uniform sample. The polarity of the optical hysteresis loop firmly confirms the dominance of the Gd sublattice. Additionally, H_C and H_K are virtually identical to those of the z-gradient sample, demonstrating a magnetic resemblance between the uniform $Gd_{0.35}(FeCo)_{0.65}$ sample and the z-gradient GdFeCo sample. Distinctly different from the cases of z-gradient GdFeCo samples, no substantial dependence on the pump fluence is observed in the oscillatory parts. All temporal traces hold similar features: a sudden demagnetization process occurs within the first few picoseconds, followed by an exponentially decaying single-frequency spin oscillation. This FM-like behavior is frequently observed when the FIM is not in the vicinity of the compensation conditions. Note that these temporal traces of TR-MOKE signals also qualitatively resemble the spin dynamics of z-gradient GdFeCo samples in Regime I and Regime III. Clearly, the TR-MOKE signals from this uniform $Gd_{0.35}(FeCo)_{0.65}$ film can all be reproduced using Equation (4-2). The field dependence acquired at different pump fluences for the uniform sample is depicted in Figure 4-9c, where virtually no difference is observed among different pump fluences. The overlapping among the $f - H_{ext}$ curves suggests that the H_K remains approximately constant at different fluences, indicating the spin precession motion indeed takes place after the magnetic anisotropy is fully restored. Likewise, it is also concluded from the damping factor that the spin precession/resonance mode in this uniform $Gd_{0.35}(FeCo)_{0.65}$ film only has inconsequential dependence on the pump fluence. Note that although the $\alpha_{eff} - H_{ext}$ curves show obviously different trends, the values of α_S, which is more relevant to the intrinsic damping properties of a material, are approximately the same. These distinctive $\alpha_{eff} - H_{ext}$ curves can be explained by considering that a stronger femtosecond pulse substantially softens the magnetic anisotropy. As a result, the sample excited by high fluence is more likely to be uniformly perturbed, and the external field can also suppress

the domain fluctuations more easily, thereby leading to a reduction in the extrinsic damping contributions and less significant field dependence.

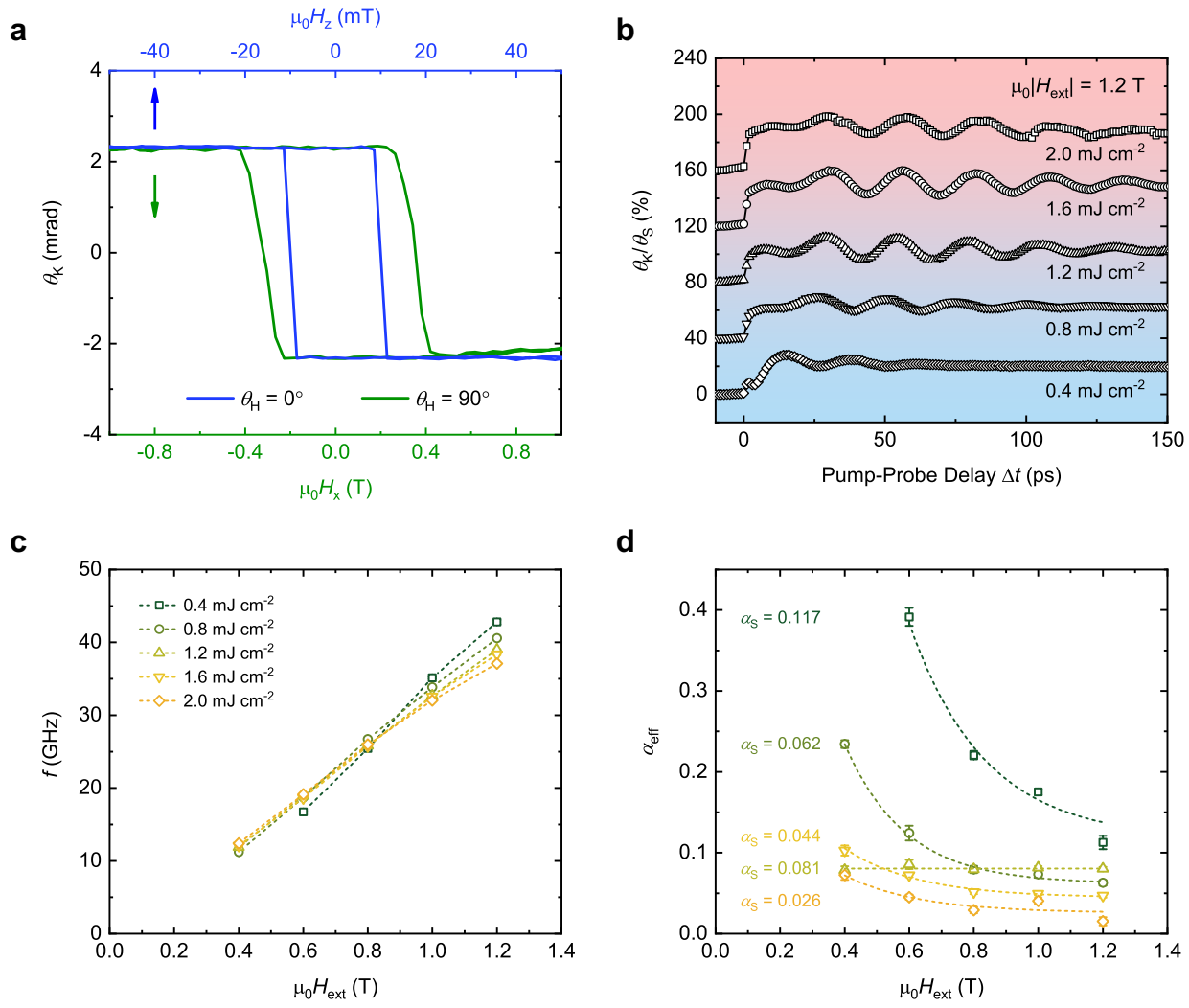

Figure 4-9. Control measurements on a uniform $Gd_{0.35}(FeCo)_{0.65}$ thin film. a. The static optical hysteresis loops of the control sample. The composition of the control sample is uniform and is selected as the average composition of the z-gradient sample ($x_{\mathrm{Gd}}^{\mathrm{avg}} = 0.35$). Both the IP and OP loops magnetically resemble those of a GdFeCo with a vertical composition gradient. **b.** Fluence dependence of the TR-MOKE measurements performed on the uniform sample under identical experimental conditions as those for the z-gradient sample. Unlike the z-gradient sample, no significant dependence on the pump fluence is detected. **c** and **d.** The fundamental dynamical

magnetic properties, f and α_{eff}, extracted from the series of field-dependent TR-MOKE measurements at different pump fluences for the uniform sample. The α_{S} in **d** implies the α_{eff} at an infinite H_{ext} and is supposedly linked to the intrinsic damping factor of a material structure. It is concluded from **c** and **d** that no significant fluence dependence is observed here.

Compared with the results collected on the z-gradient sample, this independence on the pump fluence observed in a uniform sample firmly suggests that the exotic fluence dependence and the associated spin dynamics in the z-gradient sample are surprisingly unique results of the vertical composition gradient.

More intriguingly, a further comparison reveals that the spin oscillation triggered by high-fluence pumps in the z-gradient sample (Region III of Figure 4-6a) exhibits a high degree of similarity to that observed in the uniform samples. To be more specific, the foregoing results of the fluence dependence (in Figure 4-6) reveal that the z-gradient sample manifests two distinctly dissimilar single-frequency FMR modes, namely, a low-frequency, field-independent mode excited at a low pump fluence (Regime I in Figure 4-6a) and a high-frequency, field-dependent mode excited at a higher pump fluence (Regime III in Figure 4-6a). The field dependences of these two spin resonance modes are depicted comparatively in Figure 4-10, where the data at 0.3 mJ cm^{-2} represent the features under a low-fluence stimulation (i.e., Regime I in Figure 4-6a), while the results at 2.0 mJ cm^{-2} represent the features for a high-fluence pump pulse (i.e., Regime III in Figure 4-6a). Figure 4-10 also contains the corresponding results from the uniform $Gd_{0.35}(FeCo)_{0.65}$ sample for a direct comparison, and it clearly illustrates that the high-fluence results of the z-gradient sample are magnetically similar to the only mode inherent to the uniform $Gd_{0.35}(FeCo)_{0.65}$ sample. By contrast, the results collected at low fluences feature an entirely different field

dependence. Both the α_{eff} and the f manifest a relatively low sensitivity to the external magnetic field, unmistakably implying the presence of a different spin precession/resonance mode. On the basis of these experimental observations, it is evident that the introduction of a vertical composition gradient not only does not deteriorate the highly promising dynamical properties of GdFeCo as the original ferromagnetic spin precession mode inherent to GdFeCo is well-sustained but also creates an additional distinct and peculiar spin precession/resonance mode which directly suggests that there are likely more pathways to transfer energy and angular momentum to manipulate magnetization.

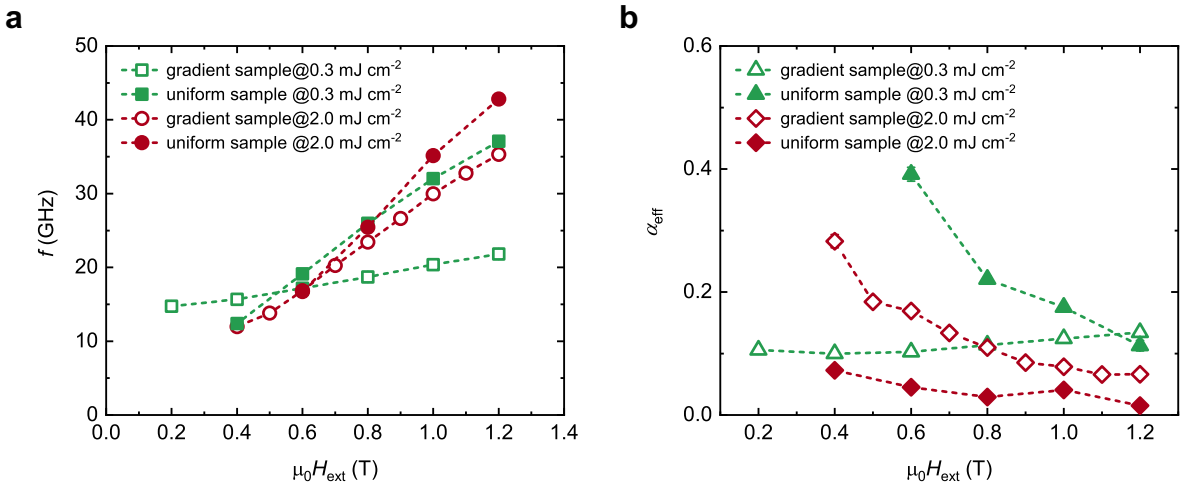

Figure 4-10. The distinction between the spin precession/resonance modes in the *z*-gradient sample and the uniform $Gd_{0.35}(FeCo)_{0.65}$ sample. a and **b.** The field dependences of spin precession frequency/damping factor in a *z*-gradient sample (open marker) and a uniform sample (solid marker). The data at 0.3 mJ cm^{-2} represent the features under low-fluence stimulation (i.e., Regime I in Figure 4-6a) and the results at 2.0 mJ cm^{-2} represent the features for high-fluence pump pulse (i.e., Regime III in Figure 4-6a). It is concluded from **a** and **b** that the *z*-gradient GdFeCo not only preserves the intrinsic spin precession mode of the normal GdFeCo material but

also features an additional spin precession/resonance mode with a distinctly dissimilar field dependence.

4.5 Summary

In Chapter 4, a newly developed ferrimagnetic structure, i.e., the GdFeCo thin film with a vertical composition gradient, was comprehensively investigated and characterized for its laser-induced ultrafast spin dynamics and dynamical properties using the TR-MOKE measurements. The material parameters of the z-gradient GdFeCo and the experimental conditions were delicately chosen to place particular emphasis on the dynamical properties that fundamentally govern the SOF-induced magnetization manipulation, which commonly proceeds via the precessional motion of spin. The main dynamical parameters, namely, spin resonance frequency and damping factor, were precisely and accurately evaluated by model-fitting the experimental TR-MOKE results produced by transient thermal excitation. The field dependences of these properties were also investigated to provide a more comprehensive understanding of the z-gradient GdFeCo. Based on the analysis of the field dependences, it was concluded that the TR-MOKE measurements yielded information that faithfully reflected the intrinsic properties of z-gradient GdFeCo. The ferromagnetic resonance frequency and damping factor were of particular interest, estimated to be a few tens of gigahertz and ~0.10, respectively. Surprisingly, while the vertical composition gradient naturally introduced additional inhomogeneities into the sample, which generally degrades the dynamical properties, these results indicated that the z-gradient sample likely preserved the technologically desired dynamical properties.

To gain further insights into the laser-induced ultrafast spin dynamics and dynamical properties of z-gradient GdFeCo, the pump fluence dependence of TR-MOKE signals was also investigated

thoroughly. Surprisingly, these signals exhibited an unusual dependence on the pump energy, which was subsequently confirmed to be a direct and unique consequence of the vertical composition gradient through comparing with a series of elaborate control experiments on a uniform $Gd_{0.35}(FeCo)_{0.65}$ sample. The TR-MOKE data and the dynamical magnetic properties extracted from the fluence-dependent results can be categorized into three distinguishable regimes. In particular, a low-frequency (~22 GHz at 1.2 T) spin oscillation with a weak field dependence was triggered with low-fluence (<0.6 mJ cm^{-2}) pump pulses. Comparatively, a field-sensitive, high-frequency (~35 GHz at 1.2 T) mode was excited by high-fluence (>1.4 mJ cm^{-2}) pump pulses. In the intermediate fluence regime (0.6 mJ cm^{-2} ~ 1.4 mJ cm^{-2}), the TR-MOKE results gradually transitioned from one mode to another and appeared to be in a mixed spin oscillatory/precessional mode. Noteworthily, the high-frequency mode of the *z*-gradient GdFeCo was virtually identical to the only intrinsic ferromagnetic resonance mode of a uniform $Gd_{0.35}(FeCo)_{0.65}$. It was therefore concluded that the *z*-gradient sample not only sustained the spin precession/resonance mode and the high-frequency properties inherent to a normal GdFeCo but also possessed various intriguing spin precession/resonance modes that were exclusively created by the vertical component gradient. These findings revealed the possible existence of much richer ultrafast spin dynamics and physics in the *z*-gradient GdFeCo. They also marked the potential of creating extra channels for injecting energy and angular momentum to better control magnetic materials by selectively introducing composition gradients.

In this respect, these observations will promote the idea of utilizing composition gradients and highlight the great flexibility of FIMs for material engineering toward faster and more efficient magnetization manipulation for advanced and applicable spintronic memory and logic devices.

CHAPTER 5. Summary and Perspective

Aiming at innovating modern magnetic memory, and more broadly, spintronic devices, this dissertation has experimentally explored two emerging classes of materials, topological insulators and ferrimagnets, for achieving more efficient and faster control of magnetism. By investigating the generation of spin-orbit torques and the correlated spin dynamics in several representative material systems and heterostructures based on topological insulators and ferrimagnets, with highlights of applying advanced magneto-optical detection techniques, this line of research has offered valuable knowledge about these novel materials and has tackled some of the core challenges in comprehending the underlying mechanisms and in developing practicable spintronic devices. In view of this, the results covered in this dissertation will doubtlessly open up new prospects for developing next-generation spintronic memory and logic applications.

Towards these aforementioned goals, this dissertation first outlined two detection techniques based on the magneto-optical Kerr effect, which have been employed to obtain the main results of this dissertation. One was a sensitive spin-orbit field magnetometer that can statically probe various magnetic phenomena and accurately characterize the underlying material properties, especially the charge-spin conversion efficiency. This optical magnetometer can serve as a powerful supplement, or even an ideal alternative, to standard magneto-transport techniques (e.g., anomalous Hall measurements). More attractively, the optical detection generally requires minimal sample preparation and allows for more flexible modulation/lock-in techniques to avoid the artifacts and nonlinear effects frequently found in traditional transport methods, making it highly preferable for investigating unconventional materials. Another technique introduced was the time-resolved magneto-optical Kerr effect measurement, an all-optical pump-probe technique designed to study ultrafast magnetism and offer in-depth analysis of dynamical magnetic properties. With an

advanced femtosecond laser, it can straightforwardly produce temporal traces of ultrafast magnetization dynamics with a sub-picosecond resolution, which is unparalleled by traditional techniques like ferromagnetic resonance experiments. In principle, these two optical detection techniques hold great promises for addressing the new challenges that come with the appealing features of topological insulators and ferrimagnets. More remarkably, the delicate integration of these two optical techniques onto a single femtosecond optical measurement platform has vastly improved the feasibility and convenience of finding novel spintronic material systems with fast dynamics and high efficiency from an experimental and technical point of view. The preceding is the main body of Chapter 2.

On the basis of these optical techniques and the laser experiment platform, topological insulators were studied for their long-predicted superiority in energy efficiency, as presented in Chapter 3. One of the most troublesome issues faced by topological insulators is the significant discrepancy among the charge-spin conversion efficiency measured by various techniques (e.g., harmonic magneto-transport measurements) in earlier reports. Indeed, the origin of these signals is still debatable. Chapter 3 began with the first application of the optical spin-orbit field magnetometer in quantifying the charge-spin conversion efficiency of topological insulators. The optical measurements were carried out on a Cr-doped topological insulator structure at cryogenic temperatures (~12 K). Notably, the optical signals unambiguously exhibited signatures that originated from the macroscopic magnetization oscillations driven by the spin-orbit fields. More convincing supports were that the charge-spin conversion efficiencies extracted from these optical results quantitatively agreed with those acquired independently from a hysteresis loop shift method. Thereby, the optical spin-orbit field magnetometer can serve as a reliable yet straightforward probe for the charge-spin conversion efficiency in topological insulator-based material systems.

Benefiting from these detection methods, subsequent investigations of the charge-spin conversion efficiencies in topological insulators, including experiments on temperature dependence and carrier concentration dependence demonstrated here and done by other collaborators,(*57*) provided a possible explanation for the disagreement in earlier studies; revealed the vital role of topological surface states in generation spin-orbit fields; and most importantly, firmly suggested that topological insulators were outstanding candidates for efficient spin current generators.

In view of these, another important issue concerned in Chapter 3 was whether it would be technologically feasible for topological insulators to be incorporated into practical spintronic memory and logic devices, in which case the ambient temperature operation and the compatibility with modern semiconductor manufacturing are indispensable. In pursuit of these goals, a topological insulator-based magnetic structure with a multifunctional molybdenum layer, i.e., topological insulator/Mo/CoFeB/MgO, was developed. As a result of this Mo insertion, the industry-preferred ferromagnetic CoFeB/MgO system with robust perpendicular anisotropy was successfully integrated onto the topological insulator with high quality, and the current-induced magnetization switching via the spin-orbit fields generated by the topological insulator was also achieved at room temperature. As envisioned, the energy efficiency of this magnetization manipulation, as parameterized by the effective spin Hall angle θ_{SH}, exceeded 100%, keeping overall power consumption at least one order of magnitude lower than those of conventional heavy metals. More excitingly, these advantages mentioned above of the topological insulator/Mo/CoFeB/MgO structures are sustained at an elevated annealing temperature up to 400 °C owing to the thermally stable Mo layer. This demonstrated, for the first time, exceptional thermal tolerance and a board heat treatment window that are imperative for the modern semiconductor industry. The findings presented in Chapter 3 delivered a definitive yes to whether

topological insulators would bring a breakthrough in the energy efficiency of spintronic applications.

Another primary focus of this dissertation was to investigate the characteristics of emerging ferrimagnetic systems with the aim of boosting the operation speed of future spintronic devices. In this regard, the dynamical properties of a ferrimagnetic GdFeCo film with a vertical compositional gradient were studied in Chapter 4 through the laser-excited ultrafast spin dynamics, which are experimentally investigated using the time-resolved magneto-optical Kerr effect measurements. It is worth noting that due to the technological interest in the fast control of magnetic moments based on spin-orbit fields, both the material structure and the experimental condition were deliberately tailored for the precession motion of spin, which underlies the majority of phenomena driven by spin-orbit fields. In other words, this experimental study gave a reliable estimate of the high-frequency properties intrinsic to this novel ferrimagnetic structure, and the findings were tightly relevant to the development of practical high-frequency spintronic devices.

The characterization of GdFeCo with a composition gradient was first carried out using magnetic field-dependent time-resolved magneto-optical Kerr effect measurements. Although the vertical composition gradient naturally introduces magnetic inhomogeneities, which usually deteriorates the dynamical properties, the experimentally determined ferromagnetic precession/resonance frequency of a few tens of gigahertz and damping factor of ~0.10 indicated the advantageous high-frequency performance of GdFeCo was largely preserved even in the presence of a vertical composition gradient. More surprisingly, the pump fluence substantially influenced the laser-induced spin dynamics. By comparing with a series of systematic and elaborate control experiments on a GdFeCo sample with a uniform composition profile, it was subsequently confirmed that this unusual dependence on the pump fluence was a direct and unique consequence

of the vertical composition gradient. By varying the fluence of laser excitation, two distinctly different spin precession/resonance modes — one high-frequency, field-sensitive mode intrinsic to GdFeCo, and one low-frequency, field-insensitive mode — were identified in the sample with a vertical composition gradient. It was therefore concluded that the gradient GdFeCo sample not only retained the spin precession/resonance mode and the high-frequency characteristics inherent to the uniform GdFeCo but also possessed various intriguing spin precession/resonance modes that were induced by the vertical component gradient. Going further, these findings implied the possible existence of much richer ultrafast spin dynamics and physics linked to the vertical composition gradient, and consequently, possible channels for injecting energy and angular momentum to control the dynamics of magnetization better. In this respect, these observations promoted the idea of adding functionality by introducing composition gradients and highlighted the great flexibility of ferrimagnets for material engineering toward fast and efficient magnetization manipulation, which might ultimately lead to breakthroughs in spintronic memory and logic devices.

Thanks to the community's pioneering works and ongoing efforts, including the results in this dissertation, the material and device platform for spintronics has been broadened in order to unleash the full capabilities of spintronic memory and logic devices. Along with the richer material choices come a myriad of challenges and opportunities. Indeed, much ahead remains to be addressed, explored, and accomplished. Future works could pursue the following areas concerning the further implementation of topological insulators and ferrimagnets for spintronics.

1. Presently, harnessing the exceptional charge-spin conversion efficiency in topological insulators to create advanced spin current sources and to write data efficiently to magnetic materials has been conceptually demonstrated by many researchers. The next leap in this

direction will be the incorporation of topological insulators into functional spintronic building blocks like magnetic tunnel junctions since the majority of studies to date were performed on prototypic components, i.e., multilayer thin film structures, and the development of operational devices that meet the industry standards is only in their infancy.(*137*) In particular, realizing a magnetic tunnel junction with perpendicular magnetic anisotropy and high read-out signals in terms of the tunnel magnetoresistance ratio can be targeted as a near-term goal that will appeal to the industry.(*138*) Encouragingly, several foreseeable key obstacles (*30*) along the path have already been tackled to some extent in recent proof-of-concept studies — This dissertation and Ref. (*55*) realized in a topological insulator-based magnetic structure the high thermal tolerance that was indispensable in modern semiconductor manufacture; Ref. (*71*) by J. Wang presented a magnetron-sputtered topological insulator that can potentially eliminate the needs for the sophisticated, low-throughput epitaxial growth techniques; Ref. (*115*) by P. Hai developed a conductive topological insulator that could keep the overall dissipation low when integrated with the frequently used metallic magnets in the industry; And lastly, Ref. (*137*) showcased a functional magnetic tunnel junction based on topological insulators and magnetic materials with easy-plane anisotropy, representing a big step toward achieving applicable memory components with topological insulators; Thus, the prospects for reaching the objective targeted above through further material engineering are bright.

2. Although the intrinsic material parameters of ferrimagnets strongly indicate a superior spintronic platform over the convectional ferromagnets, the direct demonstration of the corresponding fast electrical control on ferrimagnetism using spin-orbit torques is still much desired but underreported. In this respect, it is of enormous technological value to definitely establish the lower limit on the duration of current pulses necessary to successfully switch

magnetic systems using spin-orbit torques and to track the temporal evolution of the associated ultrafast magnetization reversal process. As the predicted timescales are at the sub-nanosecond level, the lack of relevant research in this direction is due in large part to the instruments' limitations in terms of bandwidth and amplitude. This obstacle has, fortunately, been largely resolved by the recent studies presented in Ref. (*139*) and Ref. (*140*) (co-authored by Q. Pan, in submission) by incorporating an Auston switch (i.e., a type of photoconductive switch) and employing the optical pump-probe technique with a femtosecond light source. In these studies, despite some trivial differences, an Auston switch, which served as an ultrafast current source, was fabricated with electrical connections to a typical spin-orbit torque device. Principally, this Auston switch was excited by the pump pulse and converted the femtosecond laser pulses into electrical pulses that could be as short as a few picoseconds. These photon-generated ultrashort current pulses were then swept into the adjacent spin-orbit torque device by a d.c. voltage applied across the Auston switch (*141*) and drove the magnetic reversal processes, which were directly monitored by the probe pulses focused onto the spin-orbit torque device with a sub-picosecond resolution. Using this approach, deterministic spin-orbit torque switching of a ferromagnet is observed for 6-ps-wide electrical pulses,(*139*) and the switching trajectories recorded in the time domain were expected to be completed on timescales of tens to hundreds of picoseconds.(*142–144*) More significantly, the straightforward temporal trajectories unambiguously revealed that ferrimagnets could be switched much faster (by a factor of ~10) than ferromagnets in a practical device.(*144*) While these studies are still at an early stage, modifications in experimental configuration and further device optimization will enable more rigorous investigations to gain a more systematic and comprehensive picture of these ultrafast electrical control of magnetization. One critical aspect is how to isolate the

experimental signals that solely originated from the ultrashort spin-orbit torques, given that the intense optical pumps by themselves can strongly perturb the magnetic system (e.g., thermal demagnetization, heat-assisted magnetization reversal, and laser-excited hot electrons), and hence, inevitably impact the measurements. A viable solution may be to make the devices larger and increase the spacing between the spin-orbit torque device and the Auston switch where the pump laser is focused. In this case, it is necessary to redesign the electrical contact by combining coplanar waveguides to support the more extended propagation of ultrashort current pulses and to re-engineer the Auston switch to sustain a stronger pump fluence and output higher currents.(*139*, *145*) Another concern is that the performance of the Auston switch, especially when combined with the spin-orbit torque device, is typically asymmetrical under positive and negative voltages for producing current pulses in different directions.(*141*) Because the switching behaviors associated with current pulses of opposite polarities with respect to an in-plane magnetic field can signify the origin in spin-orbit torques and yield essential knowledge for developing practical devices, the Auston switch has to be precisely calibrated for its unipolar behaviors. It is worth noting that this issue can be circumvented to some extent by reversing the applied field direction in the measurements instead of applying opposite currents. Along these lines, the more comprehensive and systematic investigation will certainly deliver invaluable information on the rapid magnetization switching by spin-orbit torques and potentially unveil uncharted domains of the underlying ultrafast physics. Undoubtedly, the insights gained will aid the development of ultrafast control of magnetization that is compatible with the existing electronic technologies and will spark high-speed spintronic applications in the future.

Throughout the years of research leading up to this dissertation, it has been thrilling to witness the flourishing of spintronics, and many more intriguing questions and exciting opportunities await ahead. Moving forward, the emerging topological insulators and ferrimagnets will surely keep revolutionizing the field by empowering faster and more efficient magnetization manipulation.

Reference:

1. C.-G. Stefanita, *Magnetism* (Springer Berlin Heidelberg, Berlin, Heidelberg, 2012; http://link.springer.com/10.1007/978-3-642-22977-0).
2. A. Kirilyuk, A. V. Kimel, T. Rasing, Ultrafast optical manipulation of magnetic order. *Rev. Mod. Phys.* **82**, 2731–2784 (2010).
3. M. N. Baibich, J. M. Broto, A. Fert, F. N. Van Dau, F. Petroff, P. Eitenne, G. Creuzet, A. Friederich, J. Chazelas, Giant magnetoresistance of (001)Fe/(001)Cr magnetic superlattices. *Phys. Rev. Lett.* **61**, 2472–2475 (1988).
4. G. Binasch, P. Grünberg, F. Saurenbach, W. Zinn, Enhanced magnetoresistance in layered magnetic structures with antiferromagnetic interlayer exchange. *Phys. Rev. B*. **39**, 4828–4830 (1989).
5. T. Miyazaki, N. Tezuka, Giant magnetic tunneling effect in Fe/Al2O3/Fe junction. *J. Magn. Magn. Mater.* **139**, L231–L234 (1995).
6. J. Mathon, A. Umerski, Theory of tunneling magnetoresistance of an epitaxial Fe/MgO/Fe(001) junction. *Phys. Rev. B - Condens. Matter Mater. Phys.* **63**, 1–4 (2001).
7. J. Åkerman, Toward a universal memory. *Science (80-.).* **308**, 508–510 (2005).
8. J. S. Moodera, L. R. Kinder, T. M. Wong, R. Meservey, Large magnetoresistance at room temperature in ferromagnetic thin film tunnel junctions. *Phys. Rev. Lett.* **74**, 3273–3276 (1995).
9. M. Bowen, V. Cros, F. Petroff, A. Fert, C. Martínez Boubeta, J. L. Costa-Krämer, J. V. Anguita, A. Cebollada, F. Briones, J. M. De Teresa, L. Morellón, M. R. Ibarra, F. Güell, F. Peiró, A. Cornet, Large magnetoresistance in Fe/MgO/FeCo(001) epitaxial tunnel junctions on GaAs(001). *Appl. Phys. Lett.* **79**, 1655–1657 (2001).

10. S. Ikeda, J. Hayakawa, Y. Ashizawa, Y. M. Lee, K. Miura, H. Hasegawa, M. Tsunoda, F. Matsukura, H. Ohno, Tunnel magnetoresistance of 604% at 300 K by suppression of Ta diffusion in CoFeBMgOCoFeB pseudo-spin-valves annealed at high temperature. *Appl. Phys. Lett.* **93**, 1–4 (2008).

11. K. L. Wang, J. G. Alzate, P. Khalili Amiri, Low-power non-volatile spintronic memory: STT-RAM and beyond. *J. Phys. D. Appl. Phys.* **46** (2013), doi:10.1088/0022-3727/46/7/074003.

12. S. D. Bader, S. S. P. Parkin, Spintronics. *Annu. Rev. Condens. Matter Phys.* **1**, 71–88 (2010).

13. W. Zhao, E. Belhaire, C. Chappert, F. Jacquet, P. Mazoyer, New non-volatile logic based on spin-MTJ. *Phys. Status Solidi Appl. Mater. Sci.* **205**, 1373–1377 (2008).

14. N. Maciel, E. Marques, L. Naviner, Y. Zhou, H. Cai, Magnetic tunnel junction applications. *Sensors (Switzerland)*. **20**, 1–20 (2020).

15. J. Grollier, D. Querlioz, K. Y. Camsari, K. Everschor-Sitte, S. Fukami, M. D. Stiles, Neuromorphic spintronics. *Nat. Electron.* **3**, 360–370 (2020).

16. J. C. Slonczewski, Current-driven excitation of magnetic multilayers. *J. Magn. Magn. Mater.* **159**, L1–L7 (1996).

17. S. Ikeda, K. Miura, H. Yamamoto, K. Mizunuma, H. D. Gan, M. Endo, S. Kanai, J. Hayakawa, F. Matsukura, H. Ohno, A perpendicular-anisotropy CoFeB-MgO magnetic tunnel junction. *Nat. Mater.* **9**, 721–724 (2010).

18. L. Liu, C. F. Pai, Y. Li, H. W. Tseng, D. C. Ralph, R. A. Buhrman, Spin-torque switching with the giant spin hall effect of tantalum. *Science (80-.).* **336**, 555–558 (2012).

19. I. M. Miron, K. Garello, G. Gaudin, P. J. Zermatten, M. V. Costache, S. Auffret, S.

Bandiera, B. Rodmacq, A. Schuhl, P. Gambardella, Perpendicular switching of a single ferromagnetic layer induced by in-plane current injection. *Nature*. **476**, 189–193 (2011).

20. A. Manchon, J. Železný, I. M. Miron, T. Jungwirth, J. Sinova, A. Thiaville, K. Garello, P. Gambardella, Current-induced spin-orbit torques in ferromagnetic and antiferromagnetic systems. *Rev. Mod. Phys.* **91** (2019), doi:10.1103/RevModPhys.91.035004.

21. I. M. Miron, G. Gaudin, S. Auffret, B. Rodmacq, A. Schuhl, S. Pizzini, J. Vogel, P. Gambardella, Current-driven spin torque induced by the Rashba effect in a ferromagnetic metal layer. *Nat. Mater.* **9**, 230–234 (2010).

22. A. Manchon, H. C. Koo, J. Nitta, S. M. Frolov, R. A. Duine, New perspectives for Rashba spin-orbit coupling. *Nat. Mater.* **14**, 871–882 (2015).

23. M. I. Dyakonov, V. I. Perel, Current-induced spin orientation of electrons in semiconductors. *Phys. Lett. A*. **35**, 459–460 (1971).

24. J. E. Hirsch, Spin Hall Effect. *Phys. Rev. Lett.* **83**, 1834–1837 (1999).

25. K. Garello, I. M. Miron, C. O. Avci, F. Freimuth, Y. Mokrousov, S. Blügel, S. Auffret, O. Boulle, G. Gaudin, P. Gambardella, Symmetry and magnitude of spin-orbit torques in ferromagnetic heterostructures. *Nat. Nanotechnol.* **8**, 587–593 (2013).

26. H. Wu, J. Zhang, B. Cui, S. A. Razavi, X. Che, Field-free approaches for deterministic spin – orbit torque switching of the.

27. Q. Shao, P. Li, L. Liu, H. Yang, S. Fukami, A. Razavi, H. Wu, K. Wang, L. Fellow, F. Freimuth, Y. Mokrousov, M. D. Stiles, S. Emori, A. Hoffmann, J. Åkerman, K. Roy, Roadmap of Spin – Orbit Torques. **57** (2021).

28. L. Liu, T. Moriyama, D. C. Ralph, R. A. Buhrman, Spin-torque ferromagnetic resonance induced by the spin Hall effect. *Phys. Rev. Lett.* **106**, 1–4 (2011).

29. C. F. Pai, L. Liu, Y. Li, H. W. Tseng, D. C. Ralph, R. A. Buhrman, Spin transfer torque devices utilizing the giant spin Hall effect of tungsten. *Appl. Phys. Lett.* **101**, 1–5 (2012).

30. C.-F. Pai, Switching by topological insulators. *Nat. Mater.* **17**, 755–757 (2018).

31. A. R. Mellnik, J. S. Lee, A. Richardella, J. L. Grab, P. J. Mintun, M. H. Fischer, A. Vaezi, A. Manchon, E. A. Kim, N. Samarth, D. C. Ralph, Spin-transfer torque generated by a topological insulator. *Nature*. **511**, 449–451 (2014).

32. X. L. Qi, S. C. Zhang, Topological insulators and superconductors. *Rev. Mod. Phys.* **83** (2011), doi:10.1103/RevModPhys.83.1057.

33. M. Z. Hasan, C. L. Kane, Colloquium: Topological insulators. *Rev. Mod. Phys.* **82**, 3045–3067 (2010).

34. Y. L. Chen, J. G. Analytis, J.-H. Chu, Z. K. Liu, S.-K. Mo, X. L. Qi, H. J. Zhang, D. H. Lu, X. Dai, Z. Fang, S. C. Zhang, I. R. Fisher, Z. Hussain, Z.-X. Shen, Experimental Realization of a Three-Dimensional Topological Insulator, Bi 2 Te 3. *Science (80-.).* **325**, 178–181 (2009).

35. H. Zhang, C. X. Liu, X. L. Qi, X. Dai, Z. Fang, S. C. Zhang, Topological insulators in Bi 2 Se 3, Bi 2 Te 3 and Sb 2 Te 3 with a single Dirac cone on the surface. *Nat. Phys.* **5**, 438–442 (2009).

36. C. H. Li, O. M. J. Van't Erve, J. T. Robinson, Y. Liu, L. Li, B. T. Jonker, Electrical detection of charge-current-induced spin polarization due to spin-momentum locking in Bi2Se3. *Nat. Nanotechnol.* **9**, 218–224 (2014).

37. J. Tang, L.-T. Chang, X. Kou, K. Murata, E. S. Choi, M. Lang, Y. Fan, Y. Jiang, M. Montazeri, W. Jiang, Y. Wang, L. He, K. L. Wang, Electrical Detection of Spin-Polarized Surface States Conduction in (Bi 0.53 Sb 0.47) 2 Te 3 Topological Insulator. *Nano Lett.*

14, 5423–5429 (2014).

38. T. Zhang, P. Cheng, X. Chen, J. F. Jia, X. Ma, K. He, L. Wang, H. Zhang, X. Dai, Z. Fang, X. Xie, Q. K. Xue, Experimental demonstration of topological surface states protected by Time-Reversal symmetry. *Phys. Rev. Lett.* **103**, 1–4 (2009).

39. X. L. Qi, S. C. Zhang, The quantum spin Hall effect and topological insulators. *Phys. Today*. **63**, 33–38 (2010).

40. V. Baltz, A. Manchon, M. Tsoi, T. Moriyama, T. Ono, Y. Tserkovnyak, Antiferromagnetic spintronics. *Rev. Mod. Phys.* **90**, 15005 (2018).

41. P. Němec, M. Fiebig, T. Kampfrath, A. V. Kimel, Antiferromagnetic opto-spintronics. *Nat. Phys.* **14**, 229–241 (2018).

42. S. K. Kim, G. S. D. Beach, K. J. Lee, T. Ono, T. Rasing, H. Yang, Ferrimagnetic spintronics. *Nat. Mater.* **21**, 24–34 (2022).

43. S. K. Kim, Fast and efficient switching with ferrimagnets. *Nat. Electron.* **3**, 18–19 (2020).

44. R. Medapalli, I. Razdolski, M. Savoini, A. R. Khorsand, A. Kirilyuk, A. V. Kimel, T. Rasing, A. M. Kalashnikova, A. Tsukamoto, A. Itoh, Efficiency of ultrafast laser-induced demagnetization in Gd xFe 100-x-yCo y alloys. *Phys. Rev. B - Condens. Matter Mater. Phys.* **86**, 1–7 (2012).

45. K. J. Kim, S. K. Kim, Y. Hirata, S. H. Oh, T. Tono, D. H. Kim, T. Okuno, W. S. Ham, S. Kim, G. Go, Y. Tserkovnyak, A. Tsukamoto, T. Moriyama, K. J. Lee, T. Ono, Fast domain wall motion in the vicinity of the angular momentum compensation temperature of ferrimagnets. *Nat. Mater.* **16**, 1187–1192 (2017).

46. C. D. Stanciu, A. V. Kimel, F. Hansteen, A. Tsukamoto, A. Itoh, A. Kirilyuk, T. Rasing, Ultrafast spin dynamics across compensation points in ferrimagnetic GdFeCo: The role of

angular momentum compensation. *Phys. Rev. B - Condens. Matter Mater. Phys.* **73**, 1–4 (2006).

47. A. K. Zvezdin, V. A. Kotov, *Modern Magnetooptics and Magnetooptical Materials* (1997; http://stacks.iop.org/075030362X).

48. J. Kerr, XLIII. On rotation of the plane of polarization by reflection from the pole of a magnet . *London, Edinburgh, Dublin Philos. Mag. J. Sci.* **3**, 321–343 (1877).

49. Z. Q. Qiu, S. D. Bader, Surface magneto-optic Kerr effect. *Rev. Sci. Instrum.* **71**, 1243–1255 (2000).

50. D. Huang, D. Lattery, X. Wang, Materials Engineering Enabled by Time-Resolved Magneto-Optical Kerr Effect for Spintronic Applications. *ACS Appl. Electron. Mater.* **3**, 119–127 (2021).

51. M. Montazeri, P. Upadhyaya, M. C. Onbasli, G. Yu, K. L. Wong, M. Lang, Y. Fan, X. Li, P. K. Amiri, R. N. Schwartz, C. A. Ross, K. L. Wang, Magneto-optical investigation of spin-orbit torques in metallic and insulating magnetic heterostructures. *Nat. Commun.* **6**, 1–9 (2015).

52. X. Fan, A. R. Mellnik, W. Wang, N. Reynolds, T. Wang, H. Celik, V. O. Lorenz, D. C. Ralph, J. Q. Xiao, All-optical vector measurement of spin-orbit-induced torques using both polar and quadratic magneto-optic Kerr effects. *Appl. Phys. Lett.* **109** (2016), doi:10.1063/1.4962402.

53. X. Fan, H. Celik, J. Wu, C. Ni, K. J. Lee, V. O. Lorenz, J. Q. Xiao, Quantifying interface and bulk contributions to spin-orbit torque in magnetic bilayers. *Nat. Commun.* **5**, 1–8 (2014).

54. Y. Fan, P. Upadhyaya, X. Kou, M. Lang, S. Takei, Z. Wang, J. Tang, L. He, L. Te Chang,

M. Montazeri, G. Yu, W. Jiang, T. Nie, R. N. Schwartz, Y. Tserkovnyak, K. L. Wang, Magnetization switching through giant spin-orbit torque in a magnetically doped topological insulator heterostructure. *Nat. Mater.* **13**, 699–704 (2014).

55. Q. Pan, Y. Liu, H. Wu, P. Zhang, H. Huang, C. Eckberg, X. Che, Y. Wu, B. Dai, Q. Shao, K. L. Wang, Efficient Spin-Orbit Torque Switching of Perpendicular Magnetization using Topological Insulators with High Thermal Tolerance. *Adv. Electron. Mater.* **2200003**, 1–10 (2022).

56. Y. Fan, K. L. Wang, Spintronics Based on Topological Insulators. *Spin*. **06**, 1640001 (2016).

57. X. Che, Q. Pan, B. Vareskic, J. Zou, L. Pan, P. Zhang, G. Yin, H. Wu, Q. Shao, P. Deng, K. L. Wang, Strongly Surface State Carrier-Dependent Spin–Orbit Torque in Magnetic Topological Insulators. *Adv. Mater.* **32**, 1–9 (2020).

58. X. Kou, M. Lang, Y. Fan, Y. Jiang, T. Nie, J. Zhang, W. Jiang, Y. Wang, Y. Yao, L. He, K. L. Wang, Interplay between Different Magnetisms in Cr-Doped Topological Insulators. *ACS Nano*. **7**, 9205–9212 (2013).

59. K. Yasuda, A. Tsukazaki, R. Yoshimi, K. S. Takahashi, M. Kawasaki, Y. Tokura, Large Unidirectional Magnetoresistance in a Magnetic Topological Insulator. *Phys. Rev. Lett.* **117**, 1–5 (2016).

60. C. F. Pai, M. Mann, A. J. Tan, G. S. D. Beach, Determination of spin torque efficiencies in heterostructures with perpendicular magnetic anisotropy. *Phys. Rev. B*. **93**, 1–7 (2016).

61. G. Yu, P. Upadhyaya, Y. Fan, J. G. Alzate, W. Jiang, K. L. Wong, S. Takei, S. A. Bender, L. Te Chang, Y. Jiang, M. Lang, J. Tang, Y. Wang, Y. Tserkovnyak, P. K. Amiri, K. L. Wang, Switching of perpendicular magnetization by spin-orbit torques in the absence of

external magnetic fields. *Nat. Nanotechnol.* **9**, 548–554 (2014).

62. J. Han, A. Richardella, S. A. Siddiqui, J. Finley, N. Samarth, L. Liu, Roomerature Spin-Orbit Torque Switching Induced by a Topological Insulator. *Phys. Rev. Lett.* **119**, 1–5 (2017).

63. C. Liu, Y. Zang, W. Ruan, Y. Gong, K. He, X. Ma, Q. K. Xue, Y. Wang, Dimensional Crossover-Induced Topological Hall Effect in a Magnetic Topological Insulator. *Phys. Rev. Lett.* **119**, 1–5 (2017).

64. Q. L. He, G. Yin, A. J. Grutter, L. Pan, X. Che, G. Yu, D. A. Gilbert, S. M. Disseler, Y. Liu, P. Shafer, B. Zhang, Y. Wu, B. J. Kirby, E. Arenholz, R. K. Lake, X. Han, K. L. Wang, Exchange-biasing topological charges by antiferromagnetism. *Nat. Commun.* **9**, 1–8 (2018).

65. S. Emori, U. Bauer, S. M. Ahn, E. Martinez, G. S. D. Beach, Current-driven dynamics of chiral ferromagnetic domain walls. *Nat. Mater.* **12**, 611–616 (2013).

66. K. Yasuda, R. Wakatsuki, T. Morimoto, R. Yoshimi, A. Tsukazaki, K. S. Takahashi, M. Ezawa, M. Kawasaki, N. Nagaosa, Y. Tokura, Geometric Hall effects in topological insulator heterostructures. *Nat. Phys.* **12**, 555–559 (2016).

67. M. Jamali, J. S. Lee, J. S. Jeong, F. Mahfouzi, Y. Lv, Z. Zhao, B. K. Nikolić, K. A. Mkhoyan, N. Samarth, J. P. Wang, Giant Spin Pumping and Inverse Spin Hall Effect in the Presence of Surface and Bulk Spin-Orbit Coupling of Topological Insulator Bi2Se3. *Nano Lett.* **15**, 7126–7132 (2015).

68. J. Tang, L. Te Chang, X. Kou, K. Murata, E. S. Choi, M. Lang, Y. Fan, Y. Jiang, M. Montazeri, W. Jiang, Y. Wang, L. He, K. L. Wang, Electrical detection of spin-polarized surface states conduction in (Bi0.53Sb0.47)2Te3topological insulator. *Nano Lett.* **14**,

5423–5429 (2014).

69. A. Dankert, J. Geurs, M. V. Kamalakar, S. Charpentier, S. P. Dash, Room temperature electrical detection of spin polarized currents in topological insulators. *Nano Lett.* **15**, 7976–7981 (2015).

70. L. Liu, A. Richardella, I. Garate, Y. Zhu, N. Samarth, C. T. Chen, Spin-polarized tunneling study of spin-momentum locking in topological insulators. *Phys. Rev. B - Condens. Matter Mater. Phys.* **91**, 1–10 (2015).

71. M. Dc, R. Grassi, J. Y. Chen, M. Jamali, D. Reifsnyder Hickey, D. Zhang, Z. Zhao, H. Li, P. Quarterman, Y. Lv, M. Li, A. Manchon, K. A. Mkhoyan, T. Low, J. P. Wang, Room-temperature high spin–orbit torque due to quantum confinement in sputtered BixSe(1–x) films. *Nat. Mater.* **17**, 800–807 (2018).

72. K. Kondou, R. Yoshimi, A. Tsukazaki, Y. Fukuma, J. Matsuno, K. S. Takahashi, M. Kawasaki, Y. Tokura, Y. Otani, Fermi-level-dependent charge-to-spin current conversion by Dirac surface states of topological insulators. *Nat. Phys.* **12**, 1027–1031 (2016).

73. Y. Fan, X. Kou, P. Upadhyaya, Q. Shao, L. Pan, M. Lang, X. Che, J. Tang, M. Montazeri, K. Murata, L. Te Chang, M. Akyol, G. Yu, T. Nie, K. L. Wong, J. Liu, Y. Wang, Y. Tserkovnyak, K. L. Wang, Electric-field control of spin-orbit torque in a magnetically doped topological insulator. *Nat. Nanotechnol.* **11**, 352–359 (2016).

74. K. Yasuda, A. Tsukazaki, R. Yoshimi, K. Kondou, K. S. Takahashi, Y. Otani, M. Kawasaki, Y. Tokura, Current-Nonlinear Hall Effect and Spin-Orbit Torque Magnetization Switching in a Magnetic Topological Insulator. *Phys. Rev. Lett.* **119**, 1–5 (2017).

75. Y. Shiomi, K. Nomura, Y. Kajiwara, K. Eto, M. Novak, K. Segawa, Y. Ando, E. Saitoh,

Spin-electricity conversion induced by spin injection into topological insulators. *Phys. Rev. Lett.* **113**, 7–11 (2014).

76. Y. Wang, P. Deorani, K. Banerjee, N. Koirala, M. Brahlek, S. Oh, H. Yang, Topological surface states originated spin-orbit torques in Bi2Se3. *Phys. Rev. Lett.* **114**, 1–5 (2015).

77. L. He, F. Xiu, X. Yu, M. Teague, W. Jiang, Y. Fan, X. Kou, M. Lang, Y. Wang, G. Huang, N. C. Yeh, K. L. Wang, Surface-dominated conduction in a 6 nm thick Bi2Se3thin film. *Nano Lett.* **12**, 1486–1490 (2012).

78. S. Fukami, T. Anekawa, C. Zhang, H. Ohno, A spin-orbit torque switching scheme with collinear magnetic easy axis and current configuration. *Nat. Nanotechnol.* **11**, 621–625 (2016).

79. H. Wu, Y. Xu, P. Deng, Q. Pan, S. A. Razavi, K. Wong, L. Huang, B. Dai, Q. Shao, G. Yu, X. Han, J. C. Rojas-Sánchez, S. Mangin, K. L. Wang, Spin-Orbit Torque Switching of a Nearly Compensated Ferrimagnet by Topological Surface States. *Adv. Mater.* **31**, 1–6 (2019).

80. K. Yamane, Y. Higo, H. Uchida, Y. Nanba, S. Sasaki, H. Ohmori, K. Bessho, M. Hosomi, Spin torque switching of perpendicularly magnetized CoFeB-based tunnel junctions with high thermal tolerance. *IEEE Trans. Magn.* **49**, 4335–4338 (2013).

81. X. Li, G. Yu, H. Wu, P. V. Ong, K. Wong, Q. Hu, F. Ebrahimi, P. Upadhyaya, M. Akyol, N. Kioussis, X. Han, P. Khalili Amiri, K. L. Wang, Thermally stable voltage-controlled perpendicular magnetic anisotropy in Mo|CoFeB|MgO structures. *Appl. Phys. Lett.* **107** (2015), doi:10.1063/1.4932553.

82. M. Li, J. Lu, G. Yu, X. Li, G. Han, X. Chen, H. Shi, G. Yu, P. K. Amiri, K. L. Wang, Influence of inserted Mo layer on the thermal stability of perpendicularly magnetized

Ta/Mo/Co20Fe60B20/MgO/Ta films. *AIP Adv.* **6** (2016), doi:10.1063/1.4947075.

83. M. Li, H. Shi, G. Yu, J. Lu, X. Chen, G. Han, G. Yu, P. K. Amiri, K. L. Wang, Effects of annealing on the magnetic properties and microstructures of Ta/Mo/CoFeB/MgO/Ta films. *J. Alloys Compd.* **692**, 243–248 (2017).

84. D. Wu, G. Yu, Q. Shao, X. Li, H. Wu, K. L. Wong, Z. Zhang, X. Han, P. Khalili Amiri, K. L. Wang, In-plane current-driven spin-orbit torque switching in perpendicularly magnetized films with enhanced thermal tolerance. *Appl. Phys. Lett.* **108**, 0–5 (2016).

85. C. Weyrich, M. Drögeler, J. Kampmeier, M. Eschbach, G. Mussler, T. Merzenich, T. Stoica, I. E. Batov, J. Schubert, L. Plucinski, B. Beschoten, C. M. Schneider, C. Stampfer, D. Grützmacher, T. Schäpers, Growth, characterization, and transport properties of ternary (Bi1-xSbx)2Te3 topological insulator layers. *J. Phys. Condens. Matter*. **28** (2016), doi:10.1088/0953-8984/28/49/495501.

86. H. Wu, P. Zhang, P. Deng, Q. Lan, Q. Pan, S. A. Razavi, X. Che, L. Huang, B. Dai, K. Wong, X. Han, K. L. Wang, Room-Temperature Spin-Orbit Torque from Topological Surface States. *Phys. Rev. Lett.* **123**, 207205 (2019).

87. T. Zhu, Y. Yang, R. C. Yu, H. Ambaye, V. Lauter, J. Q. Xiao, The study of perpendicular magnetic anisotropy in CoFeB sandwiched by MgO and tantalum layers using polarized neutron reflectometry. *Appl. Phys. Lett.* **100**, 2–6 (2012).

88. S. Peng, M. Wang, H. Yang, L. Zeng, J. Nan, J. Zhou, Y. Zhang, A. Hallal, M. Chshiev, K. L. Wang, Q. Zhang, W. Zhao, Origin of interfacial perpendicular magnetic anisotropy in MgO/CoFe/metallic capping layer structures. *Sci. Rep.* **5**, 3–8 (2015).

89. S. Peng, D. Zhu, J. Zhou, B. Zhang, A. Cao, M. Wang, W. Cai, K. Cao, W. Zhao, Modulation of Heavy Metal/Ferromagnetic Metal Interface for High-Performance

Spintronic Devices. *Adv. Electron. Mater.* **5**, 1–30 (2019).

90. Q. Shao, H. Wu, Q. Pan, P. Zhang, L. Pan, K. Wong, X. Che, K. L. Wang, *Tech. Dig. - Int. Electron Devices Meet. IEDM*, in press, doi:10.1109/IEDM.2018.8614499.

91. T. Liu, Y. Zhang, J. W. Cai, H. Y. Pan, Thermally robust Mo/CoFeB/MgO trilayers with strong perpendicular magnetic anisotropy. *Sci. Rep.* **4**, 1–6 (2014).

92. T. Y. Chen, H. I. Chan, W. B. Liao, C. F. Pai, Current-Induced Spin-Orbit Torque and Field-Free Switching in Mo-Based Magnetic Heterostructures. *Phys. Rev. Appl.* **10**, 1 (2018).

93. B. Dieny, M. Chshiev, Perpendicular magnetic anisotropy at transition metal/oxide interfaces and applications. *Rev. Mod. Phys.* **89** (2017), doi:10.1103/RevModPhys.89.025008.

94. T. Liu, J. W. Cai, L. Sun, Large enhanced perpendicular magnetic anisotropy in CoFeB/MgO system with the typical Ta buffer replaced by an Hf layer. *AIP Adv.* **2**, 1–7 (2012).

95. P. Bruno, Magnetic surface anisotropy of cobalt and surface roughness effects within Neel's model. *J. Phys. F Met. Phys.* **18**, 1291–1298 (1988).

96. Y. H. Wang, W. C. Chen, S. Y. Yang, K. H. Shen, C. Park, M. J. Kao, M. J. Tsai, Interfacial and annealing effects on magnetic properties of CoFeB thin films. *J. Appl. Phys.* **99**, 8–11 (2006).

97. N. Miyakawa, D. C. Worledge, K. Kita, Impact of TA diffusion on the perpendicular magnetic anisotropy of Ta/CoFeB/MgO. *IEEE Magn. Lett.* **4**, 4–7 (2013).

98. O. Mosendz, V. Vlaminck, J. E. Pearson, F. Y. Fradin, G. E. W. Bauer, S. D. Bader, A. Hoffmann, Detection and quantification of inverse spin Hall effect from spin pumping in

permalloy/normal metal bilayers. *Phys. Rev. B - Condens. Matter Mater. Phys.* **82**, 1–10 (2010).

99. M. Morota, K. Ohnishi, T. Kimura, Y. Otani, Spin Hall effect in Molybdenum wires. *J. Appl. Phys.* **105**, 1–4 (2009).

100. O. J. Lee, L. Q. Liu, C. F. Pai, Y. Li, H. W. Tseng, P. G. Gowtham, J. P. Park, D. C. Ralph, R. A. Buhrman, Central role of domain wall depinning for perpendicular magnetization switching driven by spin torque from the spin Hall effect. *Phys. Rev. B - Condens. Matter Mater. Phys.* **89**, 1–8 (2014).

101. P. P. J. Haazen, E. Murè, J. H. Franken, R. Lavrijsen, H. J. M. Swagten, B. Koopmans, Domain wall depinning governed by the spin Hall effect. *Nat. Mater.* **12**, 299–303 (2013).

102. M. H. Nguyen, D. C. Ralph, R. A. Buhrman, Spin Torque Study of the Spin Hall Conductivity and Spin Diffusion Length in Platinum Thin Films with Varying Resistivity. *Phys. Rev. Lett.* **116**, 1–6 (2016).

103. U. H. Pi, K. W. Kim, J. Y. Bae, S. C. Lee, Y. J. Cho, K. S. Kim, S. Seo, Tilting of the spin orientation induced by Rashba effect in ferromagnetic metal layer. *Appl. Phys. Lett.* **97**, 3–6 (2010).

104. J. Kim, J. Sinha, M. Hayashi, M. Yamanouchi, S. Fukami, T. Suzuki, S. Mitani, H. Ohno, Layer thickness dependence of the current-induced effective field vector in Ta|CoFeB|MgO. *Nat. Mater.* **12**, 240–245 (2013).

105. K. Park, J. J. Heremans, V. W. Scarola, D. Minic, Robustness of topologically protected surface states in layering of Bi 2Te3 thin films. *Phys. Rev. Lett.* **105**, 1–4 (2010).

106. C. O. Avci, K. Garello, C. Nistor, S. Godey, B. Ballesteros, A. Mugarza, A. Barla, M. Valvidares, E. Pellegrin, A. Ghosh, I. M. Miron, O. Boulle, S. Auffret, G. Gaudin, P.

Gambardella, Fieldlike and antidamping spin-orbit torques in as-grown and annealed Ta/CoFeB/MgO layers. *Phys. Rev. B - Condens. Matter Mater. Phys.* **89**, 1–13 (2014).

107. W. Zhang, W. Han, X. Jiang, S. H. Yang, S. S. P. Parkin, Role of transparency of platinum-ferromagnet interfaces in determining the intrinsic magnitude of the spin Hall effect. *Nat. Phys.* **11**, 496–502 (2015).

108. M. H. Nguyen, C. F. Pai, K. X. Nguyen, D. A. Muller, D. C. Ralph, R. A. Buhrman, Enhancement of the anti-damping spin torque efficacy of platinum by interface modification. *Appl. Phys. Lett.* **106**, 2–7 (2015).

109. J. Bass, W. P. Pratt, Spin-diffusion lengths in metals and alloys, and spin-flipping at metal/metal interfaces: An experimentalist's critical review. *J. Phys. Condens. Matter*. **19** (2007), doi:10.1088/0953-8984/19/18/183201.

110. J. C. Rojas-Sánchez, N. Reyren, P. Laczkowski, W. Savero, J. P. Attané, C. Deranlot, M. Jamet, J. M. George, L. Vila, H. Jaffrès, Spin pumping and inverse spin hall effect in platinum: The essential role of spin-memory loss at metallic interfaces. *Phys. Rev. Lett.* **112**, 1–5 (2014).

111. T. Y. Chen, C. W. Peng, T. Y. Tsai, W. B. Liao, C. Te Wu, H. W. Yen, C. F. Pai, Efficient Spin-Orbit Torque Switching with Nonepitaxial Chalcogenide Heterostructures. *ACS Appl. Mater. Interfaces*. **12**, 7788–7794 (2020).

112. R. Ramaswamy, T. Dutta, S. Liang, G. Yang, M. S. M. Saifullah, H. Yang, Spin orbit torque driven magnetization switching with sputtered Bi2Se3 spin current source. *J. Phys. D. Appl. Phys.* **52** (2019), doi:10.1088/1361-6463/ab0b96.

113. X. Zhang, B. Cui, J. Mao, J. Yun, Z. Yan, M. Chang, Y. Zuo, L. Xi, Topological Surface States-Induced Perpendicular Magnetization Switching in Pt/Co/Bi2Se3 Heterostructures.

Phys. Status Solidi - Rapid Res. Lett. **14**, 1–7 (2020).

114. N. H. D. Khang, S. Nakano, T. Shirokura, Y. Miyamoto, P. N. Hai, Ultralow power spin–orbit torque magnetization switching induced by a non-epitaxial topological insulator on Si substrates. *Sci. Rep.* **10**, 1–12 (2020).

115. N. H. D. Khang, Y. Ueda, P. N. Hai, A conductive topological insulator with large spin Hall effect for ultralow power spin–orbit torque switching. *Nat. Mater.* **17**, 808–813 (2018).

116. D. Céspedes-Berrocal, H. Damas, S. Petit-Watelot, D. Maccariello, P. Tang, A. Arriola-Córdova, P. Vallobra, Y. Xu, J. L. Bello, E. Martin, S. Migot, J. Ghanbaja, S. Zhang, M. Hehn, S. Mangin, C. Panagopoulos, V. Cros, A. Fert, J. C. Rojas-Sánchez, Current-Induced Spin Torques on Single GdFeCo Magnetic Layers. *Adv. Mater.* **33** (2021), doi:10.1002/adma.202007047.

117. W. H. Li, Z. Jin, D. L. Wen, X. M. Zhang, M. H. Qin, J. M. Liu, Ultrafast domain wall motion in ferrimagnets induced by magnetic anisotropy gradient. *Phys. Rev. B*. **101**, 1–7 (2020).

118. K. Zhang, L. Chen, Y. Zhang, B. Hong, Y. He, K. Lin, Z. Zhang, Z. Zheng, X. Feng, Y. Zhang, Y. Otani, W. Zhao, Efficient and controllable magnetization switching induced by intermixing-enhanced bulk spin-orbit torque in ferromagnetic multilayers. *Appl. Phys. Rev.* **9** (2022), doi:10.1063/5.0067348.

119. Z. Zheng, Y. Zhang, V. Lopez-Dominguez, L. Sánchez-Tejerina, J. Shi, X. Feng, L. Chen, Z. Wang, Z. Zhang, K. Zhang, B. Hong, Y. Xu, Y. Zhang, M. Carpentieri, A. Fert, G. Finocchio, W. Zhao, P. Khalili Amiri, Field-free spin-orbit torque-induced switching of perpendicular magnetization in a ferrimagnetic layer with a vertical composition

gradient. *Nat. Commun.* **12**, 1–9 (2021).

120. H. Wu, J. Nance, S. A. Razavi, D. Lujan, B. Dai, Y. Liu, H. He, B. Cui, D. Wu, K. Wong, K. Sobotkiewich, X. Li, G. P. Carman, K. L. Wang, Chiral Symmetry Breaking for Deterministic Switching of Perpendicular Magnetization by Spin-Orbit Torque. *Nano Lett.* **21**, 515–521 (2021).

121. S. Iihama, S. Mizukami, H. Naganuma, M. Oogane, Y. Ando, T. Miyazaki, Gilbert damping constants of Ta/CoFeB/MgO(Ta) thin films measured by optical detection of precessional magnetization dynamics. *Phys. Rev. B - Condens. Matter Mater. Phys.* **89**, 1–6 (2014).

122. D. M. Lattery, D. Zhang, J. Zhu, X. Hang, J. P. Wang, X. Wang, Low Gilbert Damping Constant in Perpendicularly Magnetized W/CoFeB/MgO Films with High Thermal Stability. *Sci. Rep.* **8**, 1–9 (2018).

123. A. Kirilyuk, A. V. Kimel, T. Rasing, Laser-induced magnetization dynamics and reversal in ferrimagnetic alloys. *Reports Prog. Phys.* **76** (2013), doi:10.1088/0034-4885/76/2/026501.

124. H. Wu, J. Nance, S. A. Razavi, D. Lujan, B. Dai, H. He, B. Cui, D. Wu, K. Wong, K. Sobotkiewich, Supporting Information of the manuscript entitled " Chiral symmetry breaking for deterministic switching of perpendicular magnetization by spin-orbit torque ," 1–18.

125. T. Kato, K. Nakazawa, R. Komiya, N. Nishizawa, S. Tsunashima, S. Iwata, Compositional dependence of g-factor and damping constant of GdFeCo amorphous alloy films. *IEEE Trans. Magn.* **44**, 3380–3383 (2008).

126. S. Joo, R. S. Alemayehu, J. G. Choi, B. G. Park, G. M. Choi, Magnetic anisotropy and

damping constant of ferrimagnetic gdco alloy near compensation point. *Materials (Basel).* **14**, 1–9 (2021).

127. A. Mekonnen, M. Cormier, A. V. Kimel, A. Kirilyuk, A. Hrabec, L. Ranno, T. Rasing, Femtosecond laser excitation of spin resonances in amorphous ferrimagnetic Gd1-xCox alloys. *Phys. Rev. Lett.* **107**, 3–6 (2011).

128. C. D. Stanciu, F. Hansteen, A. V. Kimel, A. Tsukamoto, A. Itoh, A. Kirilyuk, T. Rasing, Ultrafast interaction of the angular momentum of photons with spins in the metallic amorphous alloy GdFeCo. *Phys. Rev. Lett.* **98**, 1–4 (2007).

129. M. van Kampen, C. Jozsa, J. T. Kohlhepp, P. LeClair, L. Lagae, W. J. M. de Jonge, B. Koopmans, *Phys. Rev. Lett.*, in press, doi:10.1103/PhysRevLett.88.227201.

130. M. Vomir, L. H. F. Andrade, L. Guidoni, E. Beaurepaire, J. Y. Bigot, Real space trajectory of the ultrafast magnetization dynamics in ferromagnetic metals. *Phys. Rev. Lett.* **94**, 1–4 (2005).

131. D. Bossini, A. M. Kalashnikova, R. V. Pisarev, T. Rasing, A. V. Kimel, Controlling coherent and incoherent spin dynamics by steering the photoinduced energy flow. *Phys. Rev. B - Condens. Matter Mater. Phys.* **89**, 1–5 (2014).

132. P. Krivosik, N. Mo, S. Kalarickal, C. E. Patton, Hamiltonian formalism for two magnon scattering microwave relaxation: Theory and applications. *J. Appl. Phys.* **101**, 083901 (2007).

133. A. Capua, S. H. Yang, T. Phung, S. S. P. Parkin, Determination of intrinsic damping of perpendicularly magnetized ultrathin films from time-resolved precessional magnetization measurements. *Phys. Rev. B - Condens. Matter Mater. Phys.* **92**, 1–9 (2015).

134. E. Beaurepaire, J. C. Merle, A. Daunois, J. Y. Bigot, Ultrafast spin dynamics in

ferromagnetic nickel. *Phys. Rev. Lett.* **76**, 4250–4253 (1996).

135. C. D. Stanciu, A. Tsukamoto, A. V. Kimel, F. Hansteen, A. Kirilyuk, A. Itoh, T. Rasing, Subpicosecond magnetization reversal across ferrimagnetic compensation points. *Phys. Rev. Lett.* **99**, 14–17 (2007).

136. A. Tsukamoto, T. Sato, S. Toriumi, A. Itoh, Precessional switching by ultrashort pulse laser: Beyond room temperature ferromagnetic resonance limit. *J. Appl. Phys.* **109**, 10–13 (2011).

137. H. Wu, A. Chen, P. Zhang, H. He, J. Nance, C. Guo, J. Sasaki, T. Shirokura, P. N. Hai, B. Fang, S. A. Razavi, K. Wong, Y. Wen, Y. Ma, G. Yu, G. P. Carman, X. Han, X. Zhang, K. L. Wang, Magnetic memory driven by topological insulators. *Nat. Commun.* **12**, 1–7 (2021).

138. K. L. Wang, H. Wu, S. A. Razavi, Q. Shao, *Tech. Dig. - Int. Electron Devices Meet. IEDM*, in press, doi:10.1109/IEDM.2018.8614671.

139. K. Jhuria, J. Hohlfeld, A. Pattabi, E. Martin, A. Y. Arriola Córdova, X. Shi, R. Lo Conte, S. Petit-Watelot, J. C. Rojas-Sanchez, G. Malinowski, S. Mangin, A. Lemaître, M. Hehn, J. Bokor, R. B. Wilson, J. Gorchon, Spin–orbit torque switching of a ferromagnet with picosecond electrical pulses. *Nat. Electron.* **3**, 680–686 (2020).

140. H. Wu, D. Turan, Q. Pan, G. Wu, S. A. Razavi, N. T. Yardimci, Z. Zhang, M. Jarrahi, K. L. Wang, Picosecond spin-orbit torque switching of ferrimagnets, 1–13 (2019).

141. C. W. Berry, N. Wang, M. R. Hashemi, M. Unlu, M. Jarrahi, Significant performance enhancement in photoconductive terahertz optoelectronics by incorporating plasmonic contact electrodes. *Nat. Commun.* **4** (2013), doi:10.1038/ncomms2638.

142. K. Garello, C. O. Avci, I. M. Miron, M. Baumgartner, A. Ghosh, S. Auffret, O. Boulle, G.

Gaudin, P. Gambardella, Ultrafast magnetization switching by spin-orbit torques. *Appl. Phys. Lett.* **105** (2014), doi:10.1063/1.4902443.

143. M. M. Decker, M. S. Wörnle, A. Meisinger, M. Vogel, H. S. Körner, G. Y. Shi, C. Song, M. Kronseder, C. H. Back, Time Resolved Measurements of the Switching Trajectory of Pt/Co Elements Induced by Spin-Orbit Torques. *Phys. Rev. Lett.* **118**, 1–5 (2017).

144. K. Cai, Z. Zhu, J. M. Lee, R. Mishra, L. Ren, S. D. Pollard, P. He, G. Liang, K. L. Teo, H. Yang, Ultrafast and energy-efficient spin–orbit torque switching in compensated ferrimagnets. *Nat. Electron.* **3**, 37–42 (2020).

145. Y. Yang, R. B. Wilson, J. Gorchon, C. H. Lambert, S. Salahuddin, J. Bokor, Ultrafast magnetization reversal by picosecond electrical pulses. *Sci. Adv.* **3**, 1–7 (2017).